INFLUENCE RANGES OF THE STRESS INVARIANTS AND HARDENING TYPES ON THE MECHANICAL BEHAVIOR OF MATERIALS: MONOTONIC AND CYCLIC APPLICATIONS

Lucas Mangas Araújo

Master's dissertation
Mechanical Sciences

UNIVERSITY OF BRASILIA

Faculty of Technology
Department of Mechanical Engineering

UNIVERSITY OF BRASILIA
FACULTY OF TECHNOLOGY
DEPARTMENT OF MECHANICAL ENGINEERING

INFLUENCE RANGES OF THE STRESS INVARIANTS AND HARDENING TYPES ON THE MECHANICAL BEHAVIOR OF MATERIALS: MONOTONIC AND CYCLIC APPLICATIONS

Lucas Mangas Araújo

Advisor: Lucival Malcher, Prof. Univ (ENM/ UnB)

MASTER'S DISSERTATION

PUBLICATION NUMBER: ENM.DM -

BRASÍLIA/DF: July 28, 2021

UNIVERSITY OF BRASILIA
FACULTY OF TECHNOLOGY
DEPARTMENT OF MECHANICAL ENGINEERING

Influence Ranges of the Stress Invariants and Hardening Types On The Mechanical Behavior of Materials: Monotonic and Cyclic Applications

Lucas Mangas Araújo

REPORT SUBMITTED TO THE DEPARTMENT OF MECHANICAL ENGINEERING OF THE FACULTY OF TECHNOLOGY OF THE UNIVERSITY OF BRASILIA AS A PARTIAL REQUIREMENT FOR OBTAINING THE DEGREE OF MASTER IN MECHANICAL SCIENCES.

APPROVED BY:

Lucival Malcher, Prof. Univ (ENM/ UnB)
(Advisor)

Larissa Driemeier, Prof. Univ (USP)
(External Examiner)

Déborah de Oliveira, Prof. Univ (ENM/ UnB)
(External Examiner)

Thiago de Carvalho Rodrigues Doca, Prof. Univ (ENM/ UnB)
(Internal Examiner)

Fábio Comes de Castro, Prof. Univ (ENM/ UnB)
(Surrogate Examiner)

BRASÍLIA/DF, JULY 28, 2021.

FICHA CATALOGRÁFICA

Araújo, L.M
Influence Ranges of the Stress Invariants and Hardening Types
On The Mechanical Behavior of Materials: Monotonic and Cyclic Applications
[Distrito Federal] 2021.
xvii, 99p. (ENM/FT/UnB, Mestrado, Ciências Mecânicas, 2021.
Dissertação de Mestrado - Universidade de Brasília.
Faculdade de Tecnologia.
Departamento de Engenharia Mecânica.
Palavras-chave:
1. Invariantes de Tensão 2. Fratura Dúctil
3. Fadiga
I. ENM/FT/UnB II. Título (série)

REFERÊNCIA BIBLIOGRÁFICA

Araújo, L.M(2021). Influence Ranges of the Stress Invariants and Hardening Types On The Mechanical Behavior of Materials: Monotonic and Cyclic Applications. Dissertação de mestrado, Publicação ENM.DM - , Departamento de Engenharia Mecânica, Universidade de Brasília, Brasília, Distrito Federal, xvii, 99p.

CESSÃO DE DIREITOS

NOME DO AUTOR: Lucas Mangas Araújo.

TÍTULO DA DISSERTAÇÃO DE MESTRADO: Influence Ranges of the Stress Invariants and Hardening Types On The Mechanical Behavior of Materials: Monotonic and Cyclic Applications.

GRAU / ANO: MESTRADO / 2021

_____

Lucas Mangas Araújo

"Tudo o que muda a vida vem quieto no escuro, sem preparos de avisar."

Guimarães Rosa

Acknowledgments

I would like to firstly thank my mother Bia and my father Alex, to whom I owe pretty much everything that I have and that I am today. Without your unconditional love and support, I would not have accomplished my goals and dreams. You are and will always be my cornerstone. Words are not enough to thank you.

I would like to thank my brother Rafael, whose company was essential for me during my whole life, especially during this harsh and strange time we live.

I would like to thank my grandparents, my uncles and my cousins for all the love, advice and breakfasts. Your love and supported were vital on my path.

I would like to thank Prof.Dr. Lucival Malcher, who I proudly worked with for the last 6 years. His guidance and support were fundamental to the researcher I have became. Thank you very much for trusting in my potential and for inviting me to join several research projects. I am lucky to be able to call my supervisor as a friend.

I would like to to thank Professors Edgar and Fabio for all the extremely enlightening academic chats, friendly conversation and support. Your teachings and help were fundamental form my ambitions pursue.

I would like to thank my childhood friend Alexandre, who has been with me since 5 years old. Your friendship was always something that I could on, and it is one of the things I am most grateful for.

I would like to thank my PCMEC friends Cainã, Guilherme, Canut, Raniere, Leonel, Pedro, Caixeta, Gabriel and Remy for the funny moments, the coffee breaks and the help you gave. You have made my academic journey less heavy that I thought it would be.

I would like to thank my neighborhood friends Luis, Luan, Leo, Rafael, Pedro, Andre for all the unforgettable and hilarious moments we lives. Without you I would have the energy and good humor to keep going.

I would like to thank my Florianópolis friends Livia, Marcos, Estevan, Luisa, Raissa, Karen, who were one of the greatest surprises recently. Thank you for the unforgettable vacations, and I am really thankful to have met you.

Finally, I would like to thank CNPq (Contract 57614/2019-0) for the financial support essential for the elaboration of this dissertation.

Abstract

The objective the present work is to evaluate the effects of the stress invariants I_1 and J_3 on the mechanical behavior of metallic materials. In this regard, the Ductile Fracture (monotonic), Ultra-Low (ULCF) and Low Cycle (LCF) fatigue behavior of SAE 1045 steel was analyzed supported by the experimental information furnished by Bai (2008) and Leese and Socie (1989). Furthermore, a Gao-based model (Gao et al., 2011) with mixed (isotropic and kinematic) hardening was proposed to capture I_1 and J_3 influences. The numerical simulations conducted assuming von Mises behavior did not described properly the mechanical response from Ductile Fracture, ULCF, and LCF data, which demonstrated the SAE 1045 steel dependence on I_1 and J_3. After the calibration of Gao's a and b parameters, the numeric responses provided better agreement with respect to experiments. Interestingly, a and b were affected by the hardening type considered. In particular, significant differences between Mises and Gao based constitutive modeling arose in monotonic and ULCF conditions, while the discrepancies in LCF were less pronounced in terms of stress amplitudes. Nevertheless, the evolution of the accumulated plastic strain expected by Mises and Gao approaches deviated considerably, which suggests that stress invariants formulations may be an attractive option for incremental techniques for fatigue life assessments.

Key-words: Stress invariants, Ductile Fracture, Fatigue.

Summary

List of Figures

List of Tables

List of Abbreviations and Acronyms

BOP	Blowout preventer
ULCF	Ultra-Low Cycle Fatigue
LCF	Low Cycle Fatigue
FEM	Finite Element Method

List of Symbols

Latin symbols:

I_i	Invariants of the Cauchy stress tensor or the relative stress tensor
J_i	Invariants of the deviatoric part of the Cauchy stress tensor or the relative stress tensor
p	Hydrostatic stress
q	von Mises equivalent stress
t	Pseudo-time
r	Auxiliary variable used for the computation of the normalized third invariant
R	Thermodynamic force associated with isotropic hardening
W	Total work
W^e	Elastic work
W^p	Plastic work
H^I	Isotropic hardening modulus
n	Isotropic hardening exponent
H^K	Kinematic hardening modulus
b^K	Saturation coefficient
m	Number of Armstrong-Fredrick terms
a, b, c	Gao's constants
E	Young or elasticity modulus
G	Shear modulus
K	Bulk modulus
t_n	Time instant at the beginning of the increment
t_{n+1}	Time instant at the end of the increment
$R_{(\cdot)}$	Residual equation of the variable $(\cdot)$
x_i	Unknowns of the Newton-Raphson linear system

Error	Error of the Newton-Raphson method
C_{ij}	Elements of the inverse of the derivatives matrix
f	Objective functions
d	Displacement
$\bar{d}$	Prescribed displacement
F	Force
F^{NUM}	Numerical force predicted by the Finite Element Method
F^{EXP}	Experimentally measured force
N	Number of experimental points
K'	Ramberg-Osgood axial cyclic hardening modulus
n'	Ramberg-Osgood axial cyclic hardening exponent
K'_0	Ramberg-Osgood shear cyclic hardening modulus
n'_0	Ramberg-Osgood shear cyclic hardening exponent
F_{SWT}	Smith-Watson-Topper fatigue parameter
N_f	Crack initiation fatigue life
g	Function for the estimation of the fatigue life
k	Newton-Raphson iteration counter
R_a	Fatigue loading ratio
$\mathbf{I}$	Second order identity tensor
$\mathbf{S}$	Deviatoric component of the Cauchy stress tensor
$\mathbf{N}$	Flow vector
$\mathbf{N}^D$	Deviatoric component of the flow vector
$N^V\mathbf{I}$	Spherical component of the flow vector
$\mathbb{D}^e$	Fourth order elasticity tensor
$\mathbb{I}$	Fourth order identity tensor
$\mathbb{I}$	Fourth order deviatoric projector
$\mathbb{D}$	Consistent tangent operator
$\mathbb{D}^{ep}$	Elastoplastic tangent
$\mathbf{J}^k$	Coefficient matrix of the Newton-Raphson method at iteration k
R^k	Residual array at iteration k
K^{el}	Element stuffiness matrix
K	Global stiffness matrix
$\mathbf{p}$	Parameters array

$\mathbf{p}_0$	Parameters initial guess
$\mathbf{p}^*$	Optimized parameters
$\{\mathbf{A}_i\}$	Set of hardening thermodynamic forces

Greek symbols:

σ_y	Normal yield strength
τ_y	Shear yield strength
η	Triaxiality ratio
ξ	Normalized third invariant
θ	Lode angle
$\bar{\theta}$	Normalized Lode angle
σ_i	Principal stresses
φ	Elevator angle
$\bar{\varepsilon}^p$	Accumulated plastic strain
$\dot{\bar{\varepsilon}}^p$	Accumulated plastic strain evolution
$\dot{\gamma}$	Plastic multiplier
σ_{y0}	Initial yield strength
ω, σ_∞, δ	Isotropic hardening law parameters
ϕ	Yield criterion
δ	Dissipation per unit volume
Φ	Dissipation potential
Λ	Parameter used to compute Gao's associated variables
$\Delta\gamma$	Plastic multiplier increment
ε	Newton-Raphson method tolerance
ε_a	Axial strain amplitude
σ_a	Experimentally computed normal stress amplitude
$\bar{\sigma_a}$	Average experimentally computed normal stress amplitude
γ_a	Shear strain amplitude
τ_a	Experimentally computed shear stress amplitude
$\bar{\tau}_a$	Average experimentally computed shear stress amplitude
ν	Poisson's ratio
σ	Engineering normal stress
ε	Engineering normal strain
σ_v	True normal stress

ε_v	True normal strain
$\bar{\varepsilon}_f^p$	Accumulated plastic strain at fracture
$\bar{\varepsilon}_a^p$	Accumulated plastic strain amplitude
γ_a^p	Plastic shear strain amplitude
σ_n^{max}	Maximum normal stress at a given material plane
$\boldsymbol{\sigma}$	Cauchy stress tensor
$\boldsymbol{\varepsilon}$	Total strain tensor
$\boldsymbol{\varepsilon}^e$	Elastic strain tensor
$\boldsymbol{\varepsilon}^p$	Plastic strain tensor
$\dot{\boldsymbol{\varepsilon}}^p$	Plastic strain tensor evolution
$\boldsymbol{\beta}$	Backstress tensor
$\boldsymbol{\beta}^D$	Deviatoric component of the backstress tensor
$\beta^V\mathbf{I}$	Spherical component of the backstress tensor
$\dot{\boldsymbol{\beta}}$	Backstress tensor evolution
$\boldsymbol{\eta}$	Relative stress tensor
$\boldsymbol{\eta}^D$	Deviatoric component of the relative stress tensor
$\eta^V\mathbf{I}$	Spherical component of the relative stress tensor
$\Delta\boldsymbol{\varepsilon}$	Total strain tensor increment
$\Delta\boldsymbol{\varepsilon}^e$	Elastic strain tensor increment
$\Delta\boldsymbol{\varepsilon}^p$	Plastic strain tensor increment
$\{\boldsymbol{\alpha}_i\}$	Set of hardening thermodynamic internal variables
δ^{k+1}	Unknowns array of the Newton-Raphson method at iteration $k+1$

Operations:

$\mathrm{tr}\,(\cdot)$	Trace
$\det(\cdot)$	Determinant
$\otimes$	Tensor Product
:	Double contraction operation
$\cos^-1\,(\cdot)$	Arc-cosine
$\ln(\cdot)$	Natural logarithm
$\tanh(\cdot)$	Hyperbolic tangent
max	Maximum operator
min	Minimum operator

Others:

$(*)_n$	Internal variables at the beginning of the time step
$(*)_{n+1}^T$	Trial state
$(*)_{n+1}$	Updated internal variables

1 Introduction

1.1 Motivation

Ductile fracture and Fatigue are major topics in engineering as they are fundamental for the design of several components and structures. Both consist of the analysis of the fracture behavior of a given material, differing only on the type of loading that the structure experiences. The former focuses on monotonic loads while the latter on time-varying ones.

These phenomena have gained increasing importance in recent years due to industry demands for lighter structures, often with complex geometries, which are capable of withstanding a number of loading conditions (monotonic and cyclic). The incorrect description of the Ductile Fracture and Fatigue behavior can lead to catastrophic or failure. For instance, in 2010 an explosion on the platform Deepwater Horizon provoked an oil leak, which led to an environmental disaster on the Mexican Golf. One of the devices that could have prevented this accident is a security valve called Blowout Preventer (BOP). A report released in 2011 proved that this device did act to solve the problem, but it did not work correctly (Veritas, 2011). More recently, the turbine of an Airbus A380 presented a failure during a flight from Paris to Los Angeles, provoked by the fatigue fracture of one of its blades. The aircraft needed to make an emergency landing and fortunately, there were only material losses (BEA, 2020).

To properly predict the mechanical behavior of materials, one needs to use an adequate constitutive model. For Ductile Fracture and Fatigue (especially the ultra low and low cycle regimes), one is particularly interested in modeling the elastoplastic behavior of metallic materials. Plasticity, being a classical engineering field, has been extensively studied throughout the past century. The most well-known formulations are the ones based on von Mises yield criterion (Mises, 1913), also called J_2-based approaches. The cornerstone of these models lays in the assumption that plastic flow occurs when the elastic distortional strain energy reaches a critical level, which can be related to the second invariant J_2 of the deviatoric component $\mathbf{S}$ of the stress tensor $\boldsymbol{\sigma}$. Furthermore, plastic flow is assumed to be volume-preserving, which means that it is insensitive to pressure effects.

Mises-based approaches are widely employed by engineers and researchers to

describe the elastoplastic behavior of metallic materials near to fracture and to obtain stress amplitudes, which are vital for fatigue life assessments. Such observation can be explained by two reasons. First, J_2-formulations are relatively simple, they do not require a complex mathematical framework. Second, most of the commercial simulation softwares have von Mises models as a built-in option.

Despite the reasonable results obtained by the classical von Mises yield criterion in given practical engineering applications, it does present limitations for a range of materials and loading conditions. This is because J_2-formulation neglects the first I_1 and third J_3 invariants effects, which are relevant in many applications (Bai, 2008; Driemeier et al., 2015; Malcher et al., 2020). For instance, the BOP malfunction was related to the usage of von Mises-based design calibrated in tension, while the load conditions experienced by the BOP were shear predominant (Koutsolelos, 2012; Tekin et al., 2015; Zhu et al., 2020). In this particular case, the third invariant J_3 has a strong effect on the behavior of a range of alloys, and hence J_2-approaches may lead to inaccurate descriptions for this class of materials.

The influence of the first I_1 and third J_3 invariants on the Ductile Fracture behavior of metallic materials is acknowledged by researchers, and several studies demonstrate that they do need to be incorporated into the constitutive modeling for a more accurate mechanical behavior description (Bai and Wierzbicki, 2008; Driemeier et al., 2010; Gao et al., 2011; Malcher et al., 2012; Brünig et al., 2013). Nevertheless, the incorporation of these parameters into Fatigue analysis has not been extensively analyzed as in Ductile Fracture (Pereira et al., 2016; Algarni et al., 2017; Xu et al., 2020; Li et al., 2021a), especially within the ultra low (ULCF) and low cycle (LCF) regimes, which are the conditions with the highest plastic strain levels in time-varying load situations. Besides, the effects of these invariants on the different hardening types (Isotropic and Kinematic) were broadly discussed in cyclic conditions.

1.2 Objectives

Within this context, the present work aims to show the influence of stress invariants I_1 and J_3 on the mechanical behavior of metallic materials. More precisely, the effects provoked by these parameters on Ductile Fracture and Fatigue (ULCF and LCF conditions) responses will be discussed, along with the consequences of incorporating I_1 and J_3 into the constitutive modeling for engineering applications. Moreover, the coupling of these invariants with kinematic and isotropic hardening will be analyzed. For this purpose, one uses a Gao-based formulation (Gao et al., 2011) with kinematic and isotropic hardenings to describe SAE 1045 steel behavior, and compares the results with the experimental data of Bai (2008) and Leese and Socie (1989).

As far as the author is aware, there is a lack of works that demonstrate the role of

the stress invariants in different situations and to what extent one needs to consider them in practical situations. Within the context of this dissertation, the only study found and worth mentioning is the one from Pereira et al. (2016).

1.3 Outline of the dissertation

This dissertation is composed of eight chapters: in Chapter 2, a literature outline is presented, discussing the most relevant models that incorporate the stress invariants into the constitutive modeling and the results achieved in past years in Ductile Fracture and Fatigue fields; Chapter 3 is dedicated to introducing the basic concepts used throughout the work and to presenting Gao-based elastoplastic model (Gao et al., 2011) which incorporates stress invariant effects; in Chapter 4, the numerical implementation of the model in Chapter 3 for Finite Element calculations is developed; in Chapter 5, the material used in this work is presented, along with the experimental data from Bai (2008) and Leese and Socie (1989), as well as the calibration of the material parameters; in Chapter 6 the results obtained in Monotonic and Ultra-Low Cycle Fatigue conditions are presented and discussed; in Chapter 7 the results achieved in the Low Cycle regime are displayed and analyzed, then compared with the observations made in Chapter 6; and in Chapter 8, the conclusions and suggestions are presented.

2 Literature Overview

2.1 Stress Invariants and Their Effects

The most well-known and used models for describing the elastoplastic behavior of isotropic metallic materials are based on von Mises yield criterion (Mises, 1913). It can be shown that for isotropic alloys, the yield criterion is a function of the principal invariants I_1, I_2, and I_3 of the Cauchy stress tensor $\boldsymbol{\sigma}$. In this setting, von Mises's approaches assert that plastic flow is pressure insensitive and it occurs when the distortional elastic energy reaches a critical value. The volume-preserving feature is a characteristic shared with other plasticity models and it is supported by the experiments performed by Bridgman (Bridgman, 1923, 1931, 1949), which led to the conclusion that volume changes are reversible and hence associated with elastic deformation. The previously mentioned energy can be related to the second invariant J_2 of the deviatoric part $\mathbf{S}$ of $\boldsymbol{\sigma}$, which is the reason why these models are often called J_2-formulations. Mises-based methodologies are the go-to techniques chosen by engineers who wish to design a mechanical part or structure to withstand Ductile Fracture and Fatigue. Two main reasons explain that: first, these approaches are mathematically simple, the underlying fields are all smooth and hence, one can implement these models with relative ease; second, most of the commercial Finite Elements Codes already possess J_2-based models as built-in options, which is extremely convenient. Furthermore, these formulations provide satisfactory results in many applications.

Regardless of the success of models based on von Mises yield criterion, they display inconsistencies when used to describe a range of metallic materials, especially modern alloys, under different loading scenarios (and consequently a range of stress states) (Bai, 2008; Driemeier et al., 2015; Malcher et al., 2020). Shear predominant loads are classical examples in which J_2-formulations do not capture properly the mechanical response. These techniques require one calibration point to obtain the required material parameters, and this is usually carried out via standard tensile tests. However, several metallic materials deviate from the well-known $\sqrt{3}$ ratio between the normal σ_y and shear τ_y yield strengths predicted by the Mises approach. The inaccuracies displayed can be explained by the fact these formulations neglect the first and third invariants, which suggests that more accurate constitutive models need to embody them. (Bai and Wierzbicki, 2008; Driemeier et al., 2010; Gao et al., 2011; Malcher et al., 2012; Brünig et al., 2013)

The stress state in a given material point can be characterized by a set of parameters. In plasticity theory, researchers and authors often do this by informing the second invariant J_2 of $\mathbf{S}$, the hydrostatic stress p, and the third invariant J_3 of $\mathbf{S}$. Therefore, models that account for effects provoked by the stress invariants incorporate these mentioned stress-based variables in different ways.

The hydrostatic stress p is related to I_1, and hence some methodologies account for this parameter by directly embodying this invariant into its mathematical framework. Alternatively, some approaches prefer to use a normalized measure of p to describe the stress state and formulate the constitutive theory. The parameter commonly used in this context is the triaxiality ratio η, which is defined as the ratio between the hydrostatic stress and some equivalent stress (usually von Mises's q). The effect caused by p has been investigated in depth in the past decades. Another set of tests carried out by Bridgman (1953) showed that higher values of hydrostatic stress led to higher displacements at fracture for some steel alloys. According to Rice and Tracey (1969), p controls the rate of void nucleation and growth for tensile loads, while in compressive cases it dictates the closure of such voids. Furthermore, high triaxiality regions are hot-spots for crack initiation and consequent growth (Hancock and Mackenzie, 1976; Lemaitre, 2012). From the mathematical and constitutive point of view, p controls the size of the yield surface, and consequently, of the elastic domain. Nevertheless, η (or p) alone does not describe completely the material's ductility, especially in shear conditions (Barsoum and Faleskog, 2007a,b). Several experiments were conducted to investigate in more detail the effects of η. For instance, Bao and Wierzbicki (2004) performed a series of tests on aluminum alloy AL2024-T351 with different specimen geometries to analyze a wide range of η values. The experiments showed that triaxiality affects the crack initiation spot and the failure mechanism. Besides, following the works of Gao and Kim (2006) and Kim et al. (2007), it was observed that despite presenting similar triaxiality, different stress-states displayed different mechanical behavior. This further suggests that indeed η is not enough for modeling properly Ductile Fracture and Fatigue responses.

Thus, to cover a larger range of stress states, one needs to also consider J_3, especially in shear-predominant cases. In such situations, J_3 has a strong influence and hence provides better behavior predictions once incorporated into the formulation. One way to account for this parameter is by directly considering J_3 in the model, or through related variables: the normalized third invariant ξ or the Lode angle θ, both functions of J_3. The addition of J_3 (or ξ and θ) in the constitutive model allows capturing different failure mechanisms not captured by η, such as the formation of shear bands, changes in ductility in shear/torsion loads, and the transition of failure modes (Bao and Wierzbicki, 2004; Brünig et al., 2013). Besides, J_3 controls the shape of the yield surface (Bardet, 1990; Bai, 2008). Interestingly, according to Bai (2008), in shear-predominant scenarios, J_3 is more relevant when describing a given material mechanical response than η. Similar conclusions were achieved in recent works. (Malcher et al., 2020; Morales, 2020)

The previous paragraphs indicate that indeed p and J_3 play important roles in the mechanical behavior of metallic materials. In some situations, p is more influential, while in others J_3 is the key factor, but, in general, both need to be considered. Within this context, works have been carried out to investigate the effects of both variables and new constitutive models were proposed to account for their influence. The first yield criteria to account for stress invariants were Tresca (Tresca, 1869), Drucker-Prager (Drucker and Prager, 1952), and Möhr-Coulomb (Mohr, 1900; Coulomb, 1776). The former depends on the Lode angle (Nayak and Zienkiewicz, 1972), while the two-latter are pressure sensitive. Nevertheless, only Möhr-Coulomb considers both η and J_3 (Bardet, 1990).

Moving to some years ahead, Hosford (1972) generalized von Mises equivalent stress through a p-norm approach of $\boldsymbol{\sigma}$, which allows the incorporation of J_3 effects, besides being capable of recovering both Mises and Tresca yield criteria. In the '90s, Bardet (1990) proposed a formulation to account for both η and θ for pressure-sensitive isotropic alloys. Wilson (2002) performed tests on notched specimens of AA2024-T351 and verified the importance of the Lode-angle for such materials. Brünig (1999) also proposed a constitutive model embodying all stress invariants for Ductile Fracture applications. Bai (2008) conducted many experiments with different loading paths and specimen geometries that further showed the impact of these invariants on the fracture behavior of some alloys. Besides, the J_2-based simulations presented corroborated the limitations of this approach. Thus, Bai proposed a model for the correction of the inaccuracies displayed by Mises yield criterion. Mirone and Corallo (2010) performed numerical simulations and compared them to data from smooth and notched specimens of some metallic materials and pure copper. They confirmed that η and J_3 affect the mechanical behavior, which indicated that accurate failure predictions indeed have to consider both variables. Driemeier et al. (2010) carried out tests to study fracture in shear conditions that backed up all the observations made in previous studies. At the beginning of the past decade, Gao et al. (2011) presented a formulation incorporating all the three invariants in a new equivalent stress measure. Cavalheiro and Malcher (2017) used Gao's model to describe the mechanical response of two metallic materials and showed that in some conditions there are non-convexity issues. Malcher et al. (2012) analyzed the performance of three constitutive formulations that considered η and θ to predict fracture of ductile materials. Recently, Brünig et al. (2018) furnished important experimental data for negative triaxiality situations. Other recent works and models shed more light in the field, further corroborating the importance of p and J_3 (Pereira et al., 2016; Algarni et al., 2017; Wang and Qu, 2018; Yu et al., 2018; Zhang et al., 2019; Rad and Zajkani, 2020; Tuo et al., 2021; Li et al., 2021b; Ganjiani and Homayounfard, 2021; Li et al., 2021a).

2.2 Ductile Fracture

Roughly speaking, Ductile Fracture can be understood as the study of the fracture behavior of ductile materials under monotonic or quasi-static loading conditions, usually with the presence of permanent deformation. In many engineering applications, mastering this phenomenon is vital for the proper design of components and structures. For instance, forming process on metal sheets relies on the knowledge of material ductility (Bao and Wierzbicki, 2004; Bai et al., 2006; Bai, 2008). Furthermore, the force that the BOP needs to apply on the riser to cease oil extraction is the key information sought by BOP designers (Koutsolelos, 2012; Tekin et al., 2015; Zhu et al., 2020). To predict material ductility, force levels required to generate specified displacements without failure, or crack sites, engineers often perform their calculations and simulations on Mises-based analysis for the reasons presented previously. However, it may not be a appropriate strategy as many materials are not well described by J_2-formulations, especially if the stress state considered is not similar to the model calibration point. It is observed that the elastoplastic behavior of several alloys lays within the Tresca's and Mises's yield surfaces. Supported by this remark, modern formulations aim to describe this intermediate mechanical response by incorporating the hydrostatic stress and third invariant (Bai and Wierzbicki, 2008).

From the phenomenological point of view, ductile failure in metallic materials can be explained empirically by the nucleation, coalescence, and growth of micro defects and shear bands (McClintock, 1968; Rice and Tracey, 1969; Hancock and Mackenzie, 1976). Examples of such defects are voids generated by air bubbles formed during casting and more brittle secondary phases present in the alloy (Brown and Embury, 1973). Since constitutive theories are mathematical frameworks to describe the internal structure of materials, researchers propose models that incorporate these empirical observations. Based on the works presented previously, one way to accomplish this is by incorporating p and J_3 into the constitutive formulation. Authors have been doing this extensively in the past years (Hosford, 1972; Bardet, 1990; Brünig, 1999; Bai and Wierzbicki, 2008; Gao et al., 2011; Khan and Liu, 2012), and interesting results were obtained when stress-invariant models were used with Damage Mechanics theories (Xue, 2008; Brünig et al., 2013; Malcher and Mamiya, 2014; Cavalheiro and Malcher, 2017; Tuo et al., 2021). These approaches satisfactorily described not only the failure moment but also the crack initiation spot. Damage Mechanics formulations measure material degradation by directly defining an internal damage variable in the constitutive formulation or by employing damage indicators. Interested readers should refer to Bai (2008); Nahshon and Hutchinson (2008); Xue (2008); Lemaitre (2012); Malcher et al. (2012); Malcher and Mamiya (2014); Cavalheiro and Malcher (2017) for more detailed insights on Damage Mechanics.

2.3 Fatigue: Ultra Low Cycle and Low Cycle Regimes

The fatigue phenomenon can be understood as the failure experienced by structures and components when subjected to time-varying loads, which are common for engineering applications. For instance, Fatigue design is essential in the aircraft, vehicle and power generation industries (Fatemi and Shamsaei, 2011). Fatigue life assessment represents the major concern when designing components to withstand such failure. Structures fatigue life N_f is composed of two parts: crack initiation and crack propagation. In some situations, the former comprises the majority of N_f, while in others the latter is the longer period. Regardless, proper durability predictions depend on the usage of good techniques supported by experimental data (Dowling and Thangjitham, 2000). This work focuses on scenarios in which crack initiation plays a key role, and thus attention will be dedicated to articles and works that discuss this topic.

In the past, researchers defined two types of fatigue regimes depending on the number of cycles until rupture: High Cycle Fatigue (HCF) for N_f above 100000 cycles, and Low Cycle Fatigue (LCF) otherwise. Nevertheless, this life-based definition showed to be inappropriate, as some materials possess LCF characteristics (such as hysteresis loops) even after a large number of cycles (see Bemfica et al. (2019)). In this regard, one can outline more properly these two regimes by evaluating the presence (LCF) or not (HCF) of perceptible levels of plastic strain (Dowling and Thangjitham, 2000). Furthermore, LCF conditions with very high strain amplitude and that are within the large deformation domain are called Ultra-Low Cycle Fatigue (UCLF), which is characterized by extremely low lives and large amounts of plastic strain.

The first experiments to study fatigue behavior were conducted by Wöhler (1860), who performed rotatory bending tests on train shafts, and the techniques proposed by Goodman (1918), Basquin (1910), and Soderberg (1939) were pioneers in life estimation under uniaxial loading conditions. Nevertheless, practical applications are multiaxial, often with complex loading histories, and hence require more refined crack initiation methodologies for proper assessments. Modern approaches widely employed are based on Critical Plane and Stress Invariant formulations. In the former group, one highlights Smith et al. (1970), Brown and Miller (1973), Matake (1977), Fatemi and Socie (1988), while in the latter Crossland (1956), Dang (1971), Mamiya and Araújo (2002), Mamiya et al. (2009). These previous techniques were constructed following empirical observations from fatigue tests.

Fatigue cracks share common features with Ductile Fracture ones. Phenomenologically, the failure mechanisms are similar, they can be explained for instance by the formation of shear bands and void nucleation (Bannantine and Socie, 1988; Bemfica et al., 2019; Castro and Jiang, 2016). Besides, crack formation depends on the material and stress state. Nevertheless, Fatigue seems to possess a more intricate cracking process. Some works

demonstrate that the same material, with the same values of η and ξ, shows different crack types depending on the loading amplitudes (Bannantine and Socie, 1988; Kalnaus, 2009; Bemfica et al., 2019). Furthermore, fatigue cracks possess preferential propagation directions (interested readers can refer to Wilson et al. (2019) for a microstructure explanation on this matter).

In LCF conditions, Critical Plane approaches are particularly interesting, as some of them are stain-based methodologies. However, one needs to run a constitutive model to extract the stress history, as in these types of problems the inputs are the strain amplitudes. Therefore, the choice of a suitable constitutive formulation is vital for accurate fatigue life assessments, as well as the correct calibration of material parameters. Since solving the constitutive problem is inevitable, authors suggested the usage of incremental formulations, such as Damage Mechanics models, as they have an internal damage variable and can be useful for non-periodic cases (Lemaitre et al., 1999; Jiang et al., 2009; Lopes and Malcher, 2017; Araújo et al., 2020; Neves et al., 2020)

A good constitutive model for LCF applications is capable of furnishing stress amplitudes close enough to the experimentally observed ones to be later used in Critical Plane approaches, for instance. Besides, the predicted hysteresis loops should be similar to the experimental loops. In this setting, the performance of the constitutive formulation relies on suitable choices of i) yield criterion and ii) kinematic hardening law (isotropic hardening is not usually considered in such modeling). Regarding the latter, some common opted proposals are Prager (1955), Armstrong and Frederick (1966), Chaboche (1989), and Desmorat (2010). The yield criterion usually chosen is von Mises's, but as discussed in Ductile Fracture, several materials are not well described by Mises's predictions. Therefore, one may expect that the incorporation of p and J_3, as in Gao et al. (2011), may lead to improved results.

The UCLF regime may be viewed as an intermediate case between Ductile Fracture and LCF. In this regard, one can presume that UCLF will have features from both phenomena. Ductile Fracture modeling usually accounts only for isotropic hardening, while LCF models consider kinematic hardening. On the other hand, UCLF modeling requires the incorporation of both hardening types (Bai, 2008; Pereira et al., 2016; Algarni et al., 2017), because there is no reason to believe that there is enough time for cyclic stabilization and due to the Bauschinger effect. Furthermore, traditional Critical Plane approaches are not practical in UCLF applications, and Damage Mechanics become an attractive option (Pereira et al., 2016; Algarni et al., 2017; Xu et al., 2020; Li et al., 2021a).

3 Theoretical Framework

3.1 Stress State Characterization

The stress state in a given material point is determined by its stress tensor, more precisely the Cauchy stress tensor in our context. Every second-order tensor admits a unique decomposition into traceless (deviatoric) and spherical (volumetric) parts (Gurtin et al., 2010). Thus:

$$\boldsymbol{\sigma} = \boldsymbol{S} + p\boldsymbol{I}, \tag{3.1}$$

in which $\boldsymbol{S}$ and $p\boldsymbol{I}$ denote the deviatoric and volumetric parts of $\boldsymbol{\sigma}$ respectively. Furthermore, second order tensors also possess principal invariants $I_i, i = 1, 2, 3$, which are quantities whose values do not depend on the particular frame chosen. It can be shown that these invariants are the coefficients of the characteristic equation of the analyzed tensor. In particular for $\boldsymbol{\sigma}$

$$\sigma^3 - I_1(\boldsymbol{\sigma})\,\sigma^2 + I_2(\boldsymbol{\sigma})\,\sigma - I_3(\boldsymbol{\sigma}) = 0, \tag{3.2}$$

with σ representing the principal stresses. I_1, I_2, and I_3 are defined as:

$$\begin{cases} I_1(\boldsymbol{\sigma}) = \operatorname{tr}(\boldsymbol{\sigma}), \\ I_2(\boldsymbol{\sigma}) = \dfrac{1}{2}\left[\operatorname{tr}^2(\boldsymbol{\sigma}) - \operatorname{tr}(\boldsymbol{\sigma}^2)\right], \\ I_3(\boldsymbol{\sigma}) = \det(\boldsymbol{\sigma}), \end{cases} \tag{3.3}$$

where $\operatorname{tr}(\cdot)$ and $\det(\cdot)$ express the trace and determinant operations respectively. It is worth noting that Eq.(3.3) leads to:

$$p = \frac{1}{3} I_1(\boldsymbol{\sigma}). \tag{3.4}$$

In plasticity theory, the invariants of both $\boldsymbol{\sigma}$ and $\boldsymbol{S}$ are important, and, for notation purposes, one denotes the principal invariants of $\boldsymbol{\sigma}$ by I, and by J the ones of $\boldsymbol{S}$. The

deviatoric nature of $\mathbf{S}$ immediately leads to the conclusion $J_1(\boldsymbol{S}) = 0$, and hence:

$$\begin{cases} J_2(\boldsymbol{S}) = \dfrac{1}{2}\boldsymbol{S} : \boldsymbol{S} \\ J_3(\boldsymbol{S}) = \det(\boldsymbol{S}), \end{cases} \tag{3.5}$$

in which : represents the double contraction product, commonly referred to as the inner product between second order tensors.

Once these basic definitions are set, one can introduce formally the triaxiality ratio η, normalized third invariant ξ, and Lode Angle θ. η is defined and quotient between p and some equivalent stress measure σ_{eq}. Based on this, η can be expressed as:

$$\eta = \frac{p}{\sigma_{eq}}. \tag{3.6}$$

Next, ξ is a parameter that express J_3 in a dimensionless way through the relation:

$$\xi = \left(\frac{r}{\sigma_{eq}}\right)^3, \; r = \left(\frac{27}{2}J_3\right)^{\frac{1}{3}}. \tag{3.7}$$

Moreover, ξ is used on the definition of θ:

$$\theta = \frac{1}{3}\cos^{-1}(\xi). \tag{3.8}$$

It is worth noting that $0 \leq \theta \leq \pi/3$, and thus $-1 \leq \xi \leq 1$. The Lode Angle can be also expressed in a normalized way as:

$$\bar{\theta} = 1 - \frac{6\theta}{\pi}, \tag{3.9}$$

which implies $1 \leq \bar{\theta} \leq 1$. The triaxiality ratio and Lode Angle have interesting geometrical interpratations. In this setting, consider Fig.3.1, which shows schematically the definitions of η and θ

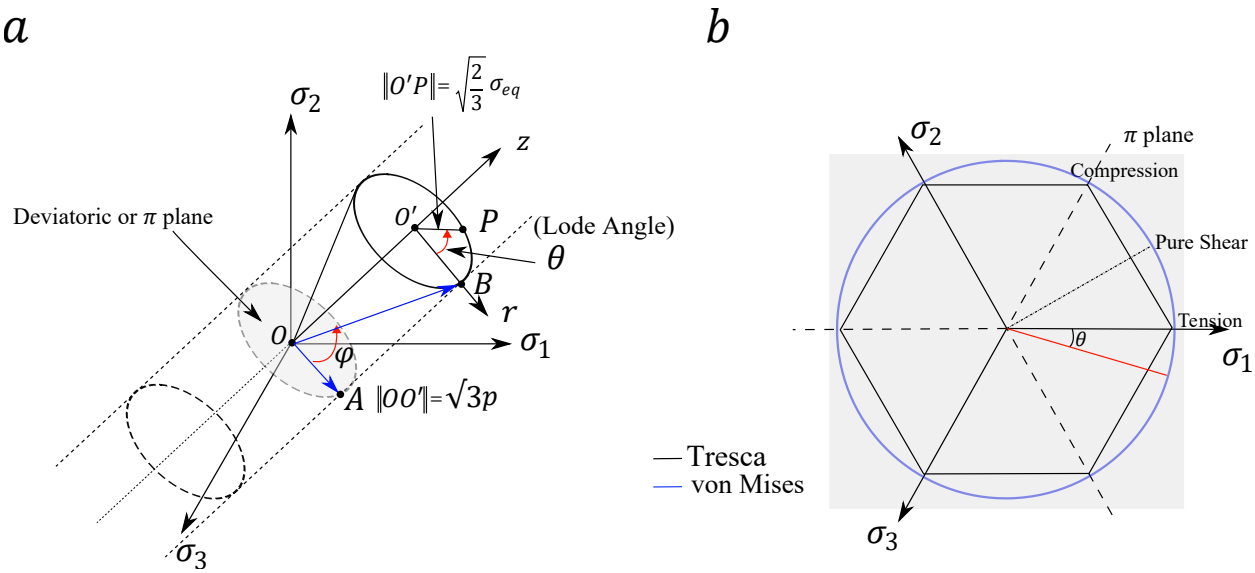

Figure 3.1 – (a) Illustration displaying the stress vector $\overrightarrow{OB}$ on the principal stress space and (b) definition of the Lode angle on π plane. Adapted from Bai (2008) and Cavalheiro and Malcher (2017).

The illustration on the left in Fig.3.1 presents the stress vector $\overrightarrow{OB}$ on the principal stress space. $\overrightarrow{OB}$ can be decomposed into two parts: a hydrostatic $\overrightarrow{OO'}$ and a deviatoric $\overrightarrow{OA}$. The triaxiality ratio η is the quotient between the lengths of these two components, and it is associated with the so called elevator angle φ (Bai, 2008). φ controls the size of the elastic domains. Figure 3.1b displays the geometrical interpretation of θ. The Lode angle is the angle formed by $\overrightarrow{OA}$ and one of the principal directions.

Table 3.1 displays the values of η, ξ, θ, $\bar{\theta}$ in some important loading scenarios:

Table 3.1 – Values assumed by the stress-based parameters in some common stress states.

Stress State	Stress-Based Parameter			
	η	ξ	θ	$\bar{\theta}$
Uniaxial Tension Loading	$\geq \frac{1}{3}$	1	0	1
Uniaxial Compression Loading	$\leq \frac{-1}{3}$	-1	$\frac{\pi}{3}$	-1
Pure Shear	0	0	$\frac{\pi}{6}$	0

3.2 Hardening Types

Fundamentally, hardening may be defined ad the dependence of the yield stress upon the history of plastic staining the material has experienced. From the yield surface point of view, hardening is responsible for changes in the surface size, shape, and orientation.

In a thermodynamically consistent framework, hardening is associated with changes in the hardening thermodynamic force (or power-conjugate) $\boldsymbol{A}$ in the presence of plastic flow (Lemaitre and Chaboche, 1994; de Souza Neto et al., 2011).

3.2.1 Microscopic Nature

Despite the macroscopic models mentioned so far and the continuum level formulation used in this work, plastic flow is a microscopic phenomenon (Lemaitre and Chaboche, 1994; Khan and Huang, 1995), closely linked with the crystalline structure of metallic materials. Ewing and Rosenhain (1900) were the first to observe that plastic deformation occurs by simple shearing provoked by the sliding of certain crystallographic planes in given directions. Besides, permanent deformation may occur by twinning. Another important source of plastic deformations are dislocations, more precisely their mobility within the crystalline structure. The augmentation in the dislocation density produced by external loads increases the number of blocking within the crystal, which manifests macroscopically into material hardening.

These are brief explanations of how plastic flow strongly influences the alloy's microstructure. For more details and references on microscopic phenomenon during plastic deformation, the reader is invited to refer to Lemaitre and Chaboche (1994); Khan and Huang (1995); de Souza Neto et al. (2011)

3.2.2 Isotropic Hardening

Isotropic Hardening models are formulations that consider a uniform (isotropic) expansion of the yield surface, without translation. Considering a Mises-based model with isotropic hardening, the Mises cylinder in the principal stress space will increase its radius in the presence of plastic flow, as depicted in Fig.3.2.

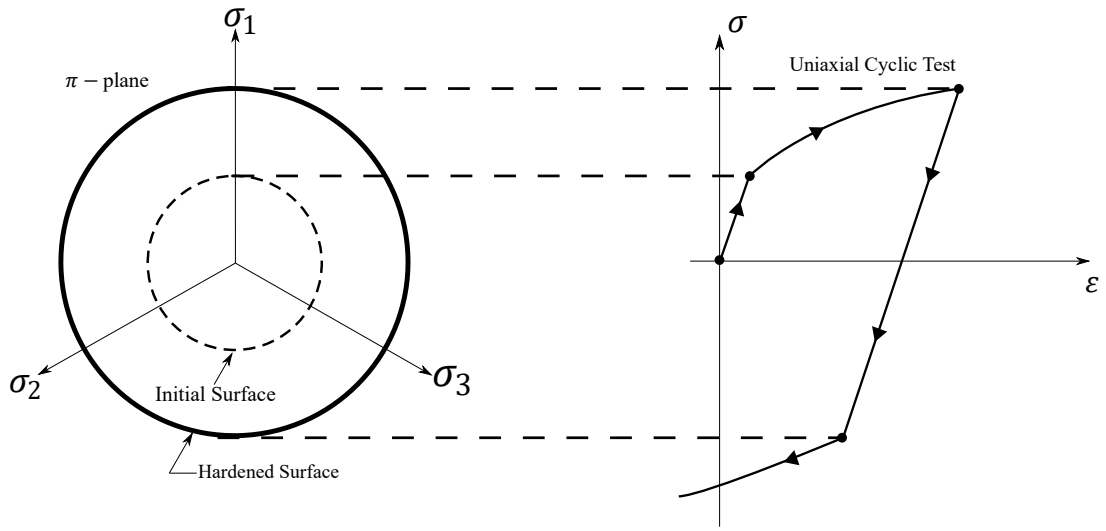

Figure 3.2 – Evolution of the Mises yield surface represented on the π-plane and the predicted Mises-based model with isotropic hardening response for a uniaxial cyclic test. Adapted from de Souza Neto et al. (2011).

Following the thermodynamic framework as in Lemaitre and Chaboche (1994) and de Souza Neto et al. (2011), the choice of the set of hardening internal variables $\{\alpha_i\}$ depend on the specific characteristics of the phenomenon and material being studied. In the case of isotropic hardening, the hardening variable is intrinsically connected with the increase in dislocation density within the metal crystallographic structure, which leads to the augmentation in the material yield strength. The classical constitutive formulations on isotropic hardening often consider $\{\boldsymbol{\alpha}_i\}$ to be composed of a single scalar internal variable. In this setting, two approaches are popular in the plasticity community for the modelling of isotropic hardening of metallic materials: strain hardening and work hardening.

3.2.2.1 Strain Hardening Approach

As the name may suggest, strain hardening models are methodologies that consider some suitably scalar measure of strain as the hardening internal variable. A widely used example is von Mises's accumulated plastic strain $\bar{\varepsilon}^p$:

$$\bar{\varepsilon}^p = \int_0^t \sqrt{\frac{2}{3}\dot{\boldsymbol{\varepsilon}}^p : \dot{\boldsymbol{\varepsilon}}^p}\, dt \Longrightarrow \dot{\bar{\varepsilon}}^p = \sqrt{\frac{2}{3}\dot{\boldsymbol{\varepsilon}}^p : \dot{\boldsymbol{\varepsilon}}^p}, \tag{3.10}$$

in which $\dot{\bar{\varepsilon}}^p$,$t$, $\dot{\boldsymbol{\varepsilon}}^p$, represent the rate evolution of $\bar{\varepsilon}^p$, the (pseudo) time variable and the rate evolution of the plastic strain tensor $\boldsymbol{\varepsilon}^p$. Therefore, a von Mises isotropic strain-hardening model asserts that the uniaxial yield stress σ_y is a function of $\bar{\varepsilon}^p$:

$$\sigma_y = \sigma_y\left(\bar{\varepsilon}^p\right), \tag{3.11}$$

or alternatively:

$$\sigma_y = \sigma_{y0} + R\left(\bar{\varepsilon}^p\right), \tag{3.12}$$

where σ_{y0}, R denote the initial yield stress and the power-conjugate of $\bar{\varepsilon}^p$ respectively. Equation (3.11) defines the strain hardening law.

3.2.2.2 Work Hardening Approach

Before introducing formally work hardening models, it is worth considering first Fig.3.3, which presents a hypothetical uniaxial tension test.

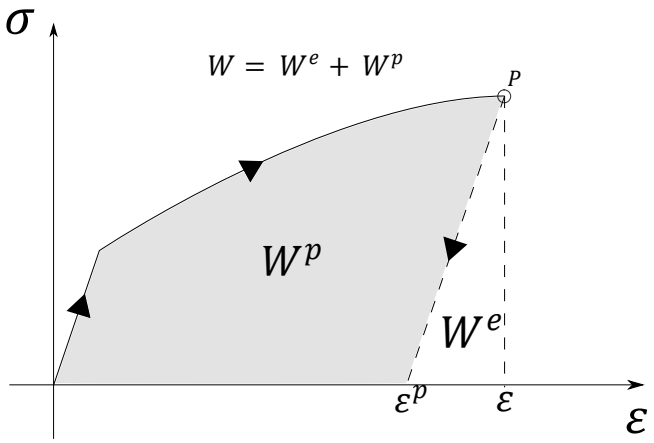

Figure 3.3 – Schematic representation of uniaxial tension test, displaying the decomposition of the total work W into elastic W^e and plastic W^p . Adapted from de Souza Neto et al. (2011).

The total work W required to deform the material to point P, followed by an elastic unloading is determined by the computation of the area under the stress-strain curve. Part of W is fully recovered in the unloading stage, and it represents the elastic work W^e. The remaining part (shaded area) W^p consists of the dissipation provoked by plasticity, and it is the plastic work, which cannot be recovered. Thus, W^p is defined by:

$$W^p = \int_0^t \boldsymbol{\sigma} : d\boldsymbol{\varepsilon}^p \Longrightarrow \dot{W}^p = \boldsymbol{\sigma} : \dot{\boldsymbol{\varepsilon}}^p. \tag{3.13}$$

For work-hardening isotropic models, σ_y is a function of W^p:

$$\sigma_y = \sigma_y\left(W^p\right), \tag{3.14}$$

or equivalently:

$$\sigma_y = \sigma_{y0} + R\left(W^p\right). \tag{3.15}$$

Therefore, Eq.(3.14) defines the work-hardening law.

3.2.2.3 Equivalence Between Strain and Work Hardening

It can be shown (see de Souza Neto et al. (2011)) that for some situations, such as associative plasticity models, strain and work hardening formulations are equivalent. This equivalence is mathematically expressed by:

$$\dot{W}^p = \boldsymbol{\sigma} : \dot{\boldsymbol{\varepsilon}}^p = \sigma_y \left(\bar{\varepsilon}^p\right) \dot{\bar{\varepsilon}}^p, \tag{3.16}$$

which enables a general definition for the evolution of the accumulated plastic strain:

$$\dot{\bar{\varepsilon}}^p = \frac{\boldsymbol{\sigma} : \dot{\boldsymbol{\varepsilon}}^p}{\sigma_y \left(\bar{\varepsilon}^p\right)} \tag{3.17}$$

Finally, two important remarks follow from Eq.(3.16). First, for an isotropic hardening von Mises formulation, Eq.(3.16) reduces to Prandtl–Reuss flow relation:

$$\dot{\bar{\varepsilon}}^p = \dot{\gamma}, \tag{3.18}$$

with $\dot{\gamma}$ denoting the plastic multiplier. Second, Eq.(3.16) can be written in terms of σ_{eq} by simple replacing σ_y by σ_{eq} in 3.16. Nevertheless, the version displayed in Eq.(3.16) is preferred in the present work.

3.2.2.4 Typical Isotropic (Strain) Hardening Laws

From this point forward and supported on the equivalence principle discussed previously, the isotropic strain-hardening law will be referred to as hardening law or hardening curve. One relatively simple hardening law is a linear relation between σ_y and $\bar{\varepsilon}^p$ (de Souza Neto et al., 2011):

$$\sigma_y = \sigma_{y0} + H^I \bar{\varepsilon}^p, \tag{3.19}$$

where H^I represents the isotropic hardening modulus. In spite of the simplicity of Eq.(3.19), it is not in general suitable for describing metal plasticity, since this phenomenon is nonlinear. Thus, nonlinear laws provide more realistic responses. In general, such relations may be expressed by:

$$\sigma_y = \sigma_{y0} + H^I \left(\bar{\varepsilon}^p\right) \bar{\varepsilon}^p. \tag{3.20}$$

One notorious nonlinear proposal is the one due to Ludwik (1909):

$$\sigma_y = \sigma_{y0} + H^I \left(\bar{\varepsilon}^p\right)^n, \tag{3.21}$$

in which n is the hardening exponent. Several other nonlinear laws are available in the literature (see Lemaitre and Chaboche (1994), Khan and Huang (1995) and Hosford (2013)). In this work, the four-parameter hardening law proposed by Kleinermann and Ponthot (2003) is used due to its good results and flexibility on describing the elatoplastic behavior of a range o materials in different geometries (Machado and Malcher, 2019):

$$\sigma_y = \sigma_{y0} + \omega\bar{\varepsilon}^p + (\sigma_\infty - \sigma_{y0})\left[1 - \exp\left(-\delta\bar{\varepsilon}^p\right)\right], \tag{3.22}$$

with ω, σ_∞ and δ material parameters that need to be calibrated based on experimental data (e.g. tensile tests.).

3.2.3 Kinematic Hardening

Kinematic hardening was proposed to model the Bauschinger effect, which is the empirical observation that materials after being loaded in one direction, often exhibit reduced resistance to plastic flow in the opposite direction (Lemaitre and Chaboche, 1994). In such experiments, isotropic hardening fails to predict this behavior.

From the yield surface perspective, kinematic hardening leads to a rigid translation in the stress space. Figure 3.4 shows the evolution of a von Mises yield surface upon kinematic hardening and the predicted response by Mises-based model with this type of hardening.

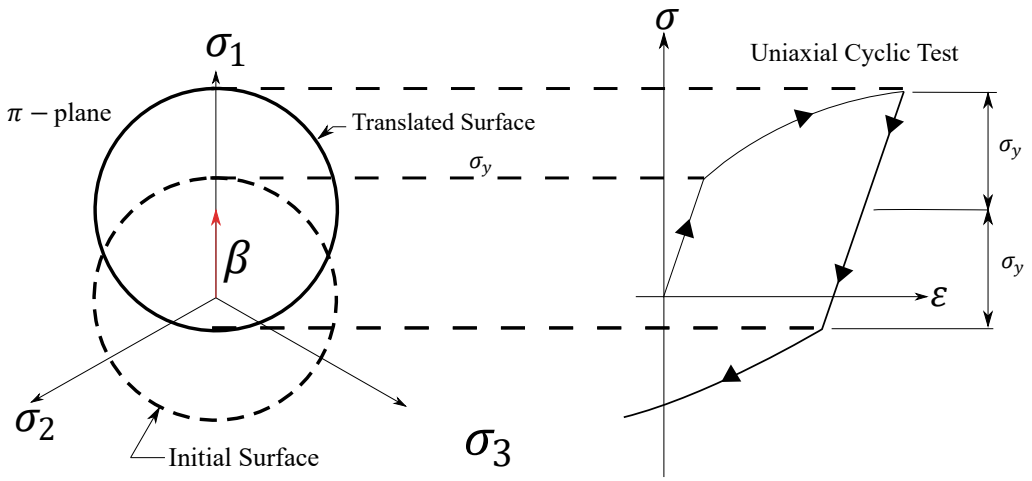

Figure 3.4 – Kinematic Hardening and the Bauschinger effect. Adapted from de Souza Neto et al. (2011).

For Mises formulations with kinematic hardening, the yield criterion is a function of $\boldsymbol{\sigma}$ and the backstress tensor $\boldsymbol{\beta}$:

$$\phi(\boldsymbol{\sigma}, \boldsymbol{\beta}) = \sqrt{J_2(\boldsymbol{\eta}(\boldsymbol{\sigma}, \boldsymbol{\beta}))} - \sigma_{y0},\ \boldsymbol{\eta}(\boldsymbol{\sigma}, \boldsymbol{\beta}) := \mathbf{S} - \boldsymbol{\beta}. \tag{3.23}$$

where $\boldsymbol{\eta}$ represents the relative stress tensor defined in this case as the difference between $\mathbf{S}$ and $\boldsymbol{\beta}$. In the particular model considered, both $\boldsymbol{\eta}$ and $\boldsymbol{\beta}$ are deviatoric tensors. The backstress tensors is the thermodynamic force linked with kinematic hardening, and represents the translation of the center of the yield surface. Besides, σ_{y0} is the radius of Mises cylinder. It worth noting that at the imminence of plastic flow ($\boldsymbol{\beta} = \mathbf{0}$), the yield surface coincides with the one for isotropic hardening.

Kinematic hardening models are important for the description of cyclic plasticity, and hence relevant for fatigue applications. In this setting, σ_{y0} is taken as the cyclic initial yield strength, which is not in general equal to the monotonic yield stress. Phenomenologically, the backstress is related to the self-equilibrated residual stresses that remain after unloading (de Souza Neto et al., 2011).

Formulations that account for kinematic hardening require a kinematic hardening law to be well-posed. This equation is the evolution relation of $\boldsymbol{\beta}$. In the next lines, one presents the most used and classical kinematic hardening laws.

3.2.3.1 Prager's Kinematic Hardening Law

Prager (1955) was the first to successfully capture Bauschinger behavior with the linear kinematic hardening law:

$$\dot{\boldsymbol{\beta}} = \frac{2}{3} H^K \dot{\boldsymbol{\varepsilon}}^p, \tag{3.24}$$

with $\dot{\boldsymbol{\beta}}$ and H^K denoting the evolution rate of $\boldsymbol{\beta}$ and the kinematic hardening modulus respectively. Regardless of the capability of predicting decreased yield strength upon load reversal, Prager's relation does not capture the nonlinear effects often observed in cyclic plasticity experiments (Chaboche, 1989).

3.2.3.2 Armstrong-Frederick Kinematic Hardening Law

Armstrong and Frederick (1966) proposed the addition of a nonlinear term to Eq.(3.24) to describe the nonlinearities observed experimentally:

$$\dot{\boldsymbol{\beta}} = \frac{2}{3} H^K \dot{\boldsymbol{\varepsilon}}^p - \dot{\bar{\varepsilon}}^p b^K \boldsymbol{\beta}, \tag{3.25}$$

in which b^K represents a material parameter, sometimes called saturation coefficient, since the term $\dot{\gamma} b \boldsymbol{\beta}$ produces a saturation effect. Despite predicting nonlinear responses, Eq.(3.25) possess some limitations. For instance, it overestimates ratchetting effects in force-controlled situations (Chaboche, 1989).

3.2.3.3 Chaboche's Kinematic Hardening Law

To overcome the limitations of Armstrong-Frederick relation, Chaboche (1989) proposed a kinematic hardening law generalizing Eq.(3.25) through a sum of m Armstrong-Frederick hardening terms:

$$\dot{\boldsymbol{\beta}} = \sum_{i=1}^{m} \left(\frac{2}{3} H_i^K \dot{\boldsymbol{\varepsilon}}^p - \dot{\bar{\varepsilon}}^p b_i^K \boldsymbol{\beta}_i \right), \tag{3.26}$$

By the introduction of more material constants, Chaboche's formulation allows a greater fitting flexibility in addition to the desired nonlinear response. Regarding the number backstress terms, Chaboche (1989) recommends $m = 3$, as it provides satisfactory correlations with experimental data.

3.2.4 Mixed Hardening

In general, real materials exhibit combined hardening behavior; that is, the yield surface translates and increases its size at the same time in the presence of plastic flow. Therefore, one may get more realistic models by mixing both kinematic and isotropic hardening (de Souza Neto et al., 2011). For instance, formulations that consider Mises yield criterion may accomplish this by letting:

$$\phi\left(\boldsymbol{\sigma}, \boldsymbol{\beta}, \bar{\varepsilon}^p\right) = \sqrt{J_2\left(\boldsymbol{\eta}\left(\boldsymbol{\sigma}, \boldsymbol{\beta}\right)\right)} - \sigma_{y0} - R\left(\bar{\varepsilon}^p\right). \tag{3.27}$$

and hence embodying the framework from both hardening types. It is worth mentioning that isotropic and kinematic hardening may be used individually as approximations for material mechanical responses in some situations. For instance, in Ductile Fracture applications, models usually consider isotropic hardening, while LCF ones take into consideration only kinematic hardening. Nevertheless, some cases require the incorporation of both hardenings, such as ULCF regime.

3.3 Gao's Equivalent Stress

As presented in Chapter 2, hydrostatic stress p and third invariant J_3 have a strong influence on the behavior of metallic materials. In this regard, the present work considers the model proposed by Gao et al. (2011), who proposed a new equivalent stress σ_{eq} incorporating I_1 and J_3:

$$\sigma_{eq} = c\left(aI_1^6 + 27J_2^3 + bJ_3^2\right)^{\frac{1}{6}}, \tag{3.28}$$

with a, b and c denoting material parameters. c is constrained by a and b by the relation:

$$c = \left(a + \frac{4}{729}b + 1\right)^{\frac{-1}{6}}, \tag{3.29}$$

which can be demonstrated by considering a uniaxial loading condition. Two remarks should be noted. Firstly, Gao's equivalent stresss reduces to von Mises's when $a = b = 0$. Secondly, under uniaxial loading conditions, the Gao's and Mises yield surfaces coincide.

3.4 Gao-Based Model with Mixed Kinematic Hardening

3.4.1 Preliminary Aspects

In this dissertation, a Gao-based model with mixed hardening is proposed. One opts for a mixed hardening approach because it not only comprises all the phenomenons studied but also allows the particularization to one specific hardening type (isotropic and kinematic) by simply setting to zero some material parameters. Furthermore, the model is presented in small deformation context.

3.4.2 Thermodynamics: Basic Concepts

Within the context of thermodynamically consistent formulations, every constitutive process must satisfy the free-energy imbalance (Gurtin et al., 2010). For purely mechanical theories (e.g plasticity), this imbalance simplifies to a dissipation inequality. In general, for plasticity models, the dissipation imbalance has the form

$$\delta = \boldsymbol{\sigma} : \dot{\boldsymbol{\varepsilon}}^p - \boldsymbol{A}_i * \dot{\boldsymbol{\alpha}}_i \geq 0 \tag{3.30}$$

with δ and $\boldsymbol{A}_i$ denoting the dissipation per unit volume and the set of thermodyncamic forces respectively, while $*$ represents the proper product between $\boldsymbol{A}_i$ and $\dot{\boldsymbol{\alpha}}_i$. The convexity of the yield surface is directly connected to Eq.(3.30).

The evolution equations of $\boldsymbol{A}_i$ are determined by the specification of the dissipation potential Ψ, while the state laws are given by the free-energy potential ϕ. In associative plasticity models, Φ is equal to model yield function.

Despite of being cited throughout the text, thermodynamics of continua framework and concepts are not the aim of this work, and hence will not be discussed in full details. They are presented in this section to provide a basic notion of what are the physical constraints that plasticity (and all constitutive modelling) is subjected. Interested readers on this topics can refer to Gurtin et al. (2010) and Lemaitre and Chaboche (1994) for a detailed explanations of the mechanics and thermodynamics of continua.

3.4.3 Additive Strain Decomposition

The strain tensor $\boldsymbol{\varepsilon}$ is decomposed into an elastic $\boldsymbol{\varepsilon}^e$ and plastic $\boldsymbol{\varepsilon}^p$ parts:

$$\boldsymbol{\varepsilon} = \boldsymbol{\varepsilon}^e + \boldsymbol{\varepsilon}^p \Longrightarrow \boldsymbol{\varepsilon}^e = \boldsymbol{\varepsilon} - \boldsymbol{\varepsilon}^p. \tag{3.31}$$

3.4.4 Hooke's Law

The Cauchy stress tensor $\boldsymbol{\sigma}$ is related with $\boldsymbol{\varepsilon}^e$ via Hoooke's Law:

$$\boldsymbol{\sigma} = \mathbb{D}^e : \boldsymbol{\varepsilon}^e = \mathbb{D}^e : \left(\boldsymbol{\varepsilon} - \boldsymbol{\varepsilon}^p\right) \tag{3.32}$$

in which $\mathbb{D}^e$ represents the the fourth order elasticity tensor. For isotropic materials and with aid of the Representation Theorem for Isotropic Linear Tensor Functions (see Gurtin et al. (2010)), $\mathbb{D}^e$ has the form:

$$\mathbb{D}^e = 2G\mathbb{I}^D + K\boldsymbol{I} \otimes \boldsymbol{I}, \tag{3.33}$$

where G and K are the shear and bulk moduli respectively, while $\mathbb{I}^D$ and $\mathbf{I}$ denote the fourth order deviatoric projector and second order identity tensor respectively. $\mathbb{I}^D$ is defined as:

$$\mathbb{I}^D = \mathbb{I} - \frac{1}{3}\boldsymbol{I} \otimes \boldsymbol{I}, \tag{3.34}$$

with $\mathbb{I}$ and $\otimes$ respectively represening the fourth order identity tensor and the tensor product operation.

3.4.5 Yield Criterion

Following a similar structure as displayed in Eq.(3.27), one proposes a yield function based on Gao's equivalent stress:

$$\phi = \sigma_{eq}\left(\boldsymbol{\eta}\right) - \sigma_y\left(\bar{\varepsilon}^p\right) \leq 0. \tag{3.35}$$

The notation $\sigma_{eq}\left(\boldsymbol{\eta}\right)$ in Eq.(3.35) is to emphasize that the invariants needed to compute σ_{eq} are the ones of $\boldsymbol{\eta}$. Equation (3.35) also defines the elastic domain $\phi < 0$ and the yield surface $\phi = 0$.

Since the model is pressure sensitive, the definition of the relative stress tensor in Eq.(3.23) cannot be used. Instead, a generalized definition is used:

$$\boldsymbol{\eta}\left(\boldsymbol{\sigma},\,\boldsymbol{\beta}\right) \coloneqq \boldsymbol{\sigma} - \boldsymbol{\beta}. \tag{3.36}$$

It is worth observing that in this case, neither $\boldsymbol{\eta}$ nor $\boldsymbol{\beta}$ are deviatoric due to model pressure sensitivity. Therefore, $\boldsymbol{\eta}$ may be expressed as the sum of a spherical $\eta^V\mathbf{I}$ and deviatoric $\boldsymbol{\eta}^D$ components:

$$\boldsymbol{\eta} = \eta^V\boldsymbol{I} + \boldsymbol{\eta}^D, \tag{3.37}$$

which further implies the relations:

$$\begin{cases} \boldsymbol{\eta}^D = \boldsymbol{S} - \boldsymbol{\beta}^D, \\ \eta^V = p - \beta^V, \end{cases} \tag{3.38}$$

where $\boldsymbol{\beta}^D$ is the deviatoric component of $\boldsymbol{\beta}$ and

$$\beta^V = \frac{1}{3}\mathrm{tr}\left(\boldsymbol{\beta}\right), \tag{3.39}$$

is related with the volumetric part of $\boldsymbol{\beta}$.

3.4.6 Flow Law

The Flow Law is the evolution equation of $\boldsymbol{\varepsilon}^p$. Assuming an associative approach, it follows:

$$\dot{\boldsymbol{\varepsilon}^p} = \dot{\gamma}\frac{\partial\phi}{\partial\boldsymbol{\sigma}} = \dot{\gamma}\boldsymbol{N}, \tag{3.40}$$

with $\boldsymbol{N}$ denoting the flow vector. By the chain rule, it is possible to show that:

$$\boldsymbol{N} = \frac{\partial\phi}{\partial\boldsymbol{\sigma}} = \frac{\partial\phi}{\partial\boldsymbol{\eta}}. \tag{3.41}$$

Next, by Eq.(3.35), one may conclude:

$$\mathbf{N} = \frac{c}{6}\Lambda^{\frac{-5}{6}}\left[6aI_1^5\left(\boldsymbol{\eta}\right)\boldsymbol{I} + 81J_2^2\left(\boldsymbol{\eta}^D\right) + 2bJ_3\left(\boldsymbol{\eta}^D\right)\det\left(\boldsymbol{\eta}^D\right)\left(\boldsymbol{\eta}^D\right)^{-T} : \mathbb{I}^D\right], \tag{3.42}$$

where $\left(\boldsymbol{\eta}^D\right)^{-T}$ is the inverse of the transpose of $\boldsymbol{\eta}^D$ and :

$$\Lambda = aI_1^6\left(\boldsymbol{\eta}\right) + 27J_2^3\left(\boldsymbol{\eta}^D\right) + bJ_3^2\left(\boldsymbol{\eta}^D\right). \tag{3.43}$$

Since $\boldsymbol{N}$ is a second order tensor, it admits a decomposition as in Eq.(3.1):

$$\boldsymbol{N} = N^V \boldsymbol{I} + \boldsymbol{N}^D, \tag{3.44}$$

and hence by Eq.(3.42):

$$\begin{cases} \boldsymbol{N}^D = \frac{c}{6}\Lambda^{\frac{-5}{6}} \left[81 J_2^2 \left(\boldsymbol{\eta}^D\right) + 2bJ_3 \left(\boldsymbol{\eta}^D\right) \det\left(\boldsymbol{\eta}^D\right) \left(\boldsymbol{\eta}^D\right)^{-T} : \mathbb{I}^D \right], \\ \\ N^V = ac\Lambda^{\frac{-5}{6}} I_1^5 \left(\boldsymbol{\eta}\right). \end{cases} \tag{3.45}$$

3.4.7 Accumulated Plastic Strain Evolution and Hardening Law

The evolution equation for $\bar{\varepsilon}^p$ presented in Eq.(3.17) needs to be adapted to account for kinematic hardening. In this regard, $\dot{\bar{\varepsilon}}^p$ is given by

$$\dot{\bar{\varepsilon}}^p = \dot{\gamma} \frac{\boldsymbol{\eta} : \boldsymbol{N}}{\sigma_y\left(\bar{\varepsilon}^p\right)}. \tag{3.46}$$

Equations 3.37 and 3.44 leads to alternative form of Eq.(3.46):

$$\dot{\bar{\varepsilon}}^p = \frac{\dot{\gamma}}{\sigma_y\left(\bar{\varepsilon}^p\right)} \left(\boldsymbol{\eta}^D : \boldsymbol{N}^D + 3\eta^V N^V \right). \tag{3.47}$$

The hardening law chosen is the Kleinermann and Ponthot (2003) relation displayed in Eq.(3.22).

3.4.8 Kinematic Hardening Law

The backstress tensor evolution is assumed to follow Armstrong-Frederick kinematic hardening law as displayed in Eq.(3.25).

3.4.9 Complementary Conditions

The complementary conditions provide the constraints on the plastic flow. Basically, the stress state can only be within the elastic domains or on the yield surface if yielding takes place. Mathematically:

$$\dot{\gamma} \geq 0, \ , \phi \leq 0, \dot{\gamma}\phi = 0 \tag{3.48}$$

3.4.10 Persistence Conditions

The persistence conditions assert that during plastic flow, the stress state must remain on the yield surface. Theses conditions are expressed by the inequalities:

$$\text{if } \phi = 0 \Longrightarrow \dot{\gamma} \geq 0,\ \dot{\phi} \leq 0,\ \dot{\gamma}\dot{\phi} = 0. \tag{3.49}$$

4 Numerical Methodology

The mathematical model presented in Chapter 3 is formed by a set of equations needed to compute the history of the internal variables for a given loading path. However, only a limited number of loading conditions have analytical solutions, and hence numerical techniques must be employed in general cases.

The numerical methodology is divided into two parts(de Souza Neto et al., 2011) :

- First, the update of the internal variables is carried out at the Gauss point level for each (pseudo) time increment. This is the local phase of the numerical solution,
- Second, the updated variables are used to calculate the consistent tangent operator, which is required assemble the stofness matrix for the Finite Element Method (FEM). This is the global phase of the numerical technique.

The local part of the numerical solution is based on the operator decomposition procedure (Simo and Hughes, 1998) and it is addressed in the next section.

4.1 State Update Procedure-The Return Mapping Algorithm

The first step to numerically solve the local problem consists of using some numerical scheme to discretize the constitutive equations. The problem can be summarized as follows: given the total strain increment $\Delta\boldsymbol{\varepsilon}$ and the value of internal variables $(*)_n$ at the time instant t_n(i.e at the beginning of the increment), one desires to compute the updated internal variables $(*)_{n+1}$ at the end of the increment (i.e at t_{n+1}).

In this regard, the operator decomposition method, also called elastic predictor/-plastic corrector algorithm, to obtain $(*)_{n+1}$ (Simo and Hughes, 1998; de Souza Neto et al., 2011). This methodology consists of two steps: firstly, it is assumed that $\Delta\boldsymbol{\varepsilon}$ does not cause yielding, and hence and elastic step. Next, supported by this assumption, the trial state is constructed $(*)^T_{n+1}$ and one evaluates the yield criterion ϕ^T_{n+1} given in Eq.(3.35). If $\phi^T_{n+1} < 0$ then $\Delta\boldsymbol{\varepsilon}$ is indeed purely elastic, $(*)_{n+1} = (*)^T_{n+1}$, and another increment is performed. If $\phi^T_{n+1} \geq 0$, plastic flow takes place and one activates the plastic corrector to obtain $(*)_{n+1}$. This latter often is referred to as the Return Mapping Algorithm (see de Souza Neto et al. (2011) for a geometrical explanation about this nomenclature).

Euler's discretization techniques are common options used in plastic corrector phase. Within this methodology, three approaches are possible: explicit, mid-point (or trapezoidal) and implicit Euler integration schemes (Simo and Hughes, 1998; de Souza Neto et al., 2011). This work formulates its numerical strategy employing the latter strategy, due to some of its advantageous features (de Souza Neto et al., 2011). In implicit frameworks, the plastic corrector consists ,in general, of a set of nonlinear equations formed by the evolution equations of the internal variables (or their power-conjugates), and the yield function. To solve the nonlinear system, Newton-Raphson method is chosen due to its quadratic convergence rate for good initial guesses (Simo and Hughes, 1998; de Souza Neto et al., 2011). Particularly, the trial state is used as the initial guess in the iterative process, which is carried out until some stop condition is satisfied.

This procedure was implemented in the academic Finite Element code HYPLAS(Simo and Hughes, 1998; de Souza Neto et al., 2011) through a user defined State Update subroutine.

4.1.1 Trial State-Elastic Predictor

Assuming that $\Delta\boldsymbol{\varepsilon}$ has only elastic component $\Delta\boldsymbol{\varepsilon}^e$, it follows from Eq.(3.31):

$$\begin{cases} \boldsymbol{\varepsilon}_{n+1}^{eT} = \boldsymbol{\varepsilon}_n^e + \Delta\boldsymbol{\varepsilon}, \\ \boldsymbol{\varepsilon}_{n+1}^{pT} = \boldsymbol{\varepsilon}_n^p, \end{cases} \tag{4.1}$$

with $\boldsymbol{\varepsilon}_{n+1}^{eT}$, $\boldsymbol{\varepsilon}_n^e$,$\boldsymbol{\varepsilon}_{n+1}^{pTrial}$ and $\boldsymbol{\varepsilon}_n^p$ respectively denoting the trial elastic strain tensor, the elastic strain tensor at the t_n, the trial plastic strain tensor and the plastic strain tensor at t_n. From this point forward, the upper script T will always express a trial state variable, unless specifically stated otherwise. Equation (4.1) in association with Eq.(3.32) lead to the trial Cauchy stress tensor $\boldsymbol{\sigma}_{n+1}^T$:

$$\boldsymbol{\sigma}_{n+1}^T = \mathbb{D}^e : \boldsymbol{\varepsilon}_{n+1}^{eT}, \tag{4.2}$$

which further enables of the computation of the trial deviatoric stress tensor $\boldsymbol{S}_{n+1}^T$ and trial hydrostatic stress p_{n+1}^T:

$$\begin{cases} \boldsymbol{S}_{n+1}^T = \boldsymbol{\sigma}_{n+1}^T - \frac{1}{3}\mathrm{tr}\left(\boldsymbol{\sigma}_{n+1}^T\right), \\ p_{n+1}^T = \frac{1}{3}\mathrm{tr}\left(\boldsymbol{\sigma}_{n+1}^T\right). \end{cases} \tag{4.3}$$

In the absence of yielding, there is no hardening-associated ($\bar{\varepsilon}^p$ and $\boldsymbol{\beta}$) variables

evolution:

$$\begin{cases} \bar{\varepsilon}_{n+1}^{pT} = \bar{\varepsilon}_n^p, \\ \boldsymbol{\beta}_{n+1}^T = \boldsymbol{\beta}_n, \\ \sigma_y^T = \sigma_y\left(\bar{\varepsilon}_n^p\right), \end{cases} \tag{4.4}$$

and hence the trial relative stress tensor $\boldsymbol{\eta}_{n+1}^T$ is:

$$\boldsymbol{\eta}_{n+1}^T = \boldsymbol{\sigma}_{n+1}^T - \boldsymbol{\beta}_n. \tag{4.5}$$

The validation of the trial state depends on the evaluation of the yield criterion (3.35):

$$\phi_{n+1}^T = \sigma_{eq}\left(\boldsymbol{\eta}_{n+1}^T\right) - \sigma_y^T. \tag{4.6}$$

If $\phi_{n+1}^T < 0$, the elasticity assumption is true, and the trial state is the actual updated state. However, if $\phi_{n+1}^T \geq 0$, the strain increment produces plastic flow and the plastic corrector is activated.

4.1.2 Plastic Corrector

Since plasticity takes place, it follows that $\Delta\boldsymbol{\varepsilon}$ possesses a plastic component $\Delta\boldsymbol{\varepsilon}^p$ and from Eq.(3.31) it is possible to show:

$$\boldsymbol{\varepsilon}_{n+1}^e = \boldsymbol{\varepsilon}_{n+1}^{eT} - \Delta\boldsymbol{\varepsilon}^p, \tag{4.7}$$

and thus the updated Cauchy stress tensor $\boldsymbol{\sigma}_{n+1}$ is expressed by:

$$\boldsymbol{\sigma}_{n+1} = \boldsymbol{\sigma}_{n+1}^T - \mathbb{D}^e : \Delta\boldsymbol{\varepsilon}^p. \tag{4.8}$$

Following an implicit integration scheme, one can compute:

$$\Delta\boldsymbol{\varepsilon}^p = \Delta\gamma \boldsymbol{N}_{n+1} \tag{4.9}$$

with $\Delta\gamma$ denoting the plastic multiplier increment and $\mathbf{N}_{n+1}$ representing the flow vector evaluated at t_{n+1}. Therefore, one can rewrite Eq.(4.8) as:

$$\boldsymbol{\sigma}_{n+1} = \boldsymbol{\sigma}_{n+1}^T - \Delta\gamma\mathbb{D}^e : \boldsymbol{N}_{n+1}. \tag{4.10}$$

It follows from Eq.(3.33) and (3.44) that:

$$\mathbb{D}^e\colon \boldsymbol{N}_{n+1} = 2G\boldsymbol{N}^D_{n+1} + 3KN^V_{n+1}\boldsymbol{I}, \tag{4.11}$$

which finally leads to:

$$\boldsymbol{\sigma}_{n+1} = \boldsymbol{\sigma}^T_{n+1} - 2G\Delta\gamma\boldsymbol{N}^D_{n+1} - 3K\Delta\gamma N^V_{n+1}\boldsymbol{I}. \tag{4.12}$$

For implementation purposes, it is more convenient to decompose Eq.(4.12) in spherical and deviatoric parts:

$$\begin{cases} \boldsymbol{S}_{n+1} = \boldsymbol{S}^T_{n+1} - 2G\Delta\gamma\boldsymbol{N}^D_{n+1}, \\ p_{n+1} = p^T_{n+1} - 3K\Delta\gamma N^V_{n+1}. \end{cases} \tag{4.13}$$

Next, by Eq.(3.47):

$$\bar{\varepsilon}^p_{n+1} = \bar{\varepsilon}^p_n + \left[\frac{\Delta\gamma}{\sigma_y}\left(\boldsymbol{\eta}^D\colon \boldsymbol{N}^D + 3\eta^V N^V\right)\right]\Big|_{n+1}. \tag{4.14}$$

The yield criterion constitutes the update equation for $\Delta\gamma$:

$$\phi_{n+1} = \sigma_{eq}\left(\boldsymbol{\eta}_{n+1}\right) - \sigma_y\left(\bar{\varepsilon}^p_{n+1}\right). \tag{4.15}$$

For Finite Element Calculations, Eq.(3.20) is used to approximate the calibrated hardening curve based on Eq.(3.22), and hence:

$$\phi_{n+1} = \sigma_{eq}\left(\boldsymbol{\eta}_{n+1}\right) - \sigma_{y0} - H^I\left(\bar{\varepsilon}^p_{n+1}\right)\bar{\varepsilon}^p_{n+1}, \tag{4.16}$$

where:

$$\left.\frac{d\sigma_y}{d\bar{\varepsilon}^p}\right|_{n+1} = H^I\left(\bar{\varepsilon}^p_{n+1}\right). \tag{4.17}$$

The implicit integration of Eq.(3.25) associated with Eq.(3.47) and (4.9) leads to the update equation for the backstress tensor:

$$\boldsymbol{\beta}_{n+1} = \boldsymbol{\beta}_n + \frac{2}{3}H^K\Delta\gamma\boldsymbol{N}_{n+1} - \left[\frac{b^K\Delta\gamma}{\sigma_y}\left(\boldsymbol{\eta}^D\colon \boldsymbol{N}^D + 3\eta^V N^V\right)\right]\Big|_{n+1}\boldsymbol{\beta}_{n+1}, \tag{4.18}$$

and hence the updated relative stress tensor $\boldsymbol{\eta}_{n+1}$ is given by:

$$\boldsymbol{\eta}_{n+1} = \boldsymbol{\sigma}_{n+1} - \boldsymbol{\beta}_{n+1}. \tag{4.19}$$

According to (3.38) and (4.18), the update equations for the deviatotric $\boldsymbol{\beta}^D_{n+1}$ and volumetric β^V_{n+1} components of $\boldsymbol{\beta}_{n+1}$ are then:

$$\begin{cases} \boldsymbol{\beta}^D_{n+1} = \boldsymbol{\beta}^D_n + \frac{2}{3} H^K \Delta\gamma \boldsymbol{N}^D_{n+1} - \left[\dfrac{b^K \Delta\gamma}{\sigma_y} \left(\boldsymbol{\eta}^D : \boldsymbol{N}^D + 3\eta^V N^V \right) \right] \Big|_{n+1} \boldsymbol{\beta}^D_{n+1}, \\ \beta^V_{n+1} = \beta^V_n + \frac{2}{3} H^K \Delta\gamma N^V_{n+1} - \left[\dfrac{b^K \Delta\gamma}{\sigma_y} \left(\boldsymbol{\eta}^D : \boldsymbol{N}^D + 3\eta^V N^V \right) \right] \Big|_{n+1} \beta^V_{n+1}. \end{cases} \tag{4.20}$$

Therefore the nonlinear system of equations is formed by:

$$\begin{cases} \boldsymbol{S}_{n+1} = \boldsymbol{S}^T_{n+1} - 2G\Delta\gamma \boldsymbol{N}^D_{n+1}, \\ \bar{\varepsilon}^p_{n+1} = \bar{\varepsilon}^p_n + \left[\dfrac{\Delta\gamma}{\sigma_y} \left(\boldsymbol{\eta}^D : \boldsymbol{N}^D + 3\eta^V N^V \right) \right] \Big|_{n+1}, \\ \phi_{n+1} = \sigma_{eq} \left(\boldsymbol{\eta}_{n+1} \right) - \sigma_{y0} - H^I \left(\bar{\varepsilon}^p_{n+1} \right) \bar{\varepsilon}^p_{n+1}, \\ p_{n+1} = p^T_{n+1} - 3K\Delta\gamma N^V_{n+1}, \\ \boldsymbol{\beta}^D_{n+1} = \boldsymbol{\beta}^D_n + \frac{2}{3} H^K \Delta\gamma \boldsymbol{N}^D_{n+1} - \left[\dfrac{b^K \Delta\gamma}{\sigma_y} \left(\boldsymbol{\eta}^D : \boldsymbol{N}^D + 3\eta^V N^V \right) \right] \Big|_{n+1} \boldsymbol{\beta}^D_{n+1}, \\ \beta^V_{n+1} = \beta^V_n + \frac{2}{3} H^K \Delta\gamma N^V_{n+1} - \left[\dfrac{b^K \Delta\gamma}{\sigma_y} \left(\boldsymbol{\eta}^D : \boldsymbol{N}^D + 3\eta^V N^V \right) \right] \Big|_{n+1} \beta^V_{n+1}. \end{cases} \tag{4.21}$$

The system (4.21) can be solved by the Newton-Raphson method, which in general is expressed by:

$$\mathbf{J}^k \delta^{k+1} = -R^k, \tag{4.22}$$

where $\mathbf{J}$, δ,R and k respectively express the Jacobian matrix of the nonlinear system, the variables increment and residual equations arrays, and the Newton-Raphson iteration counter. It is worth noting that Eq.(4.22) represents a linear system. In this setting, system

(4.21) need to be written in residual form:

$$\begin{cases} R_{\mathbf{S}} = \boldsymbol{S}_{n+1} - \boldsymbol{S}^{T}_{n+1} + 2G\Delta\gamma \boldsymbol{N}^{D}_{n+1} = \mathbf{0}, \\ R_{\bar{\varepsilon}^p} = \bar{\varepsilon}^{p}_{n+1} - \bar{\varepsilon}^{p}_{n} - \left[\dfrac{\Delta\gamma}{\sigma_y} \left(\boldsymbol{\eta}^{D} : \boldsymbol{N}^{D} + 3\eta^{V} N^{V} \right) \right] \Big|_{n+1} = 0, \\ R_{\Delta\gamma} = \sigma_{eq}\left(\boldsymbol{\eta}_{n+1}\right) - \sigma_{y0} - H^{I}\left(\bar{\varepsilon}^{p}_{n+1}\right) \bar{\varepsilon}^{p}_{n+1} = 0, \\ R_{p} = p_{n+1} - p^{T}_{n+1} + 3K\Delta\gamma N^{V}_{n+1} = 0, \\ R_{\boldsymbol{\beta}^D} = \boldsymbol{\beta}^{D}_{n+1} - \boldsymbol{\beta}^{D}_{n} - \frac{2}{3} H^{K}\Delta\gamma \boldsymbol{N}^{D}_{n+1} + \left[\dfrac{b^{K}\Delta\gamma}{\sigma_y} \left(\boldsymbol{\eta}^{D} : \boldsymbol{N}^{D} + 3\eta^{V} N^{V} \right) \right] \Big|_{n+1} \boldsymbol{\beta}^{D}_{n+1} = \mathbf{0}, \\ R_{\beta^V} = \beta^{V}_{n+1} - \beta^{V}_{n} - \frac{2}{3} H^{K}\Delta\gamma N^{V}_{n+1} + \left[\dfrac{b^{K}\Delta\gamma}{\sigma_y} \left(\boldsymbol{\eta}^{D} : \boldsymbol{N}^{D} + 3\eta^{V} N^{V} \right) \right] \Big|_{n+1} \beta^{V}_{n+1} = 0. \end{cases} \tag{4.23}$$

with $R_{(.)}$ representing the residual equation of the variable $(\cdot)$. Thus, the complete linearized system is:

$$\begin{bmatrix} \frac{\partial R_{\mathbf{S}}}{\partial \mathbf{S}} & \frac{\partial R_{\mathbf{S}}}{\partial \bar{\varepsilon}^p} & \frac{\partial R_{\mathbf{S}}}{\partial \Delta\gamma} & \frac{\partial R_{\mathbf{S}}}{\partial p} & \frac{\partial R_{\mathbf{S}}}{\partial \boldsymbol{\beta}^D} & \frac{\partial R_{\mathbf{S}}}{\partial \beta^V} \\ \frac{\partial R_{\bar{\varepsilon}^p}}{\partial \mathbf{S}} & \frac{\partial R_{\bar{\varepsilon}^p}}{\partial \bar{\varepsilon}^p} & \frac{\partial R_{\bar{\varepsilon}^p}}{\partial \Delta\gamma} & \frac{\partial R_{\bar{\varepsilon}^p}}{\partial p} & \frac{\partial R_{\bar{\varepsilon}^p}}{\partial \boldsymbol{\beta}^D} & \frac{\partial R_{\bar{\varepsilon}^p}}{\partial \beta^V} \\ \frac{\partial R_{\Delta\gamma}}{\partial \mathbf{S}} & \frac{\partial R_{\Delta\gamma}}{\partial \bar{\varepsilon}^p} & \frac{\partial R_{\Delta\gamma}}{\partial \Delta\gamma} & \frac{\partial R_{\Delta\gamma}}{\partial p} & \frac{\partial R_{\Delta\gamma}}{\partial \boldsymbol{\beta}^D} & \frac{\partial R_{\Delta\gamma}}{\partial \beta^V} \\ \frac{\partial R_{p}}{\partial \mathbf{S}} & \frac{\partial R_{p}}{\partial \bar{\varepsilon}^p} & \frac{\partial R_{p}}{\partial \Delta\gamma} & \frac{\partial R_{p}}{\partial p} & \frac{\partial R_{p}}{\partial \boldsymbol{\beta}^D} & \frac{\partial R_{p}}{\partial \beta^V} \\ \frac{\partial R_{\boldsymbol{\beta}^D}}{\partial \mathbf{S}} & \frac{\partial R_{\boldsymbol{\beta}^D}}{\partial \bar{\varepsilon}^p} & \frac{\partial R_{\boldsymbol{\beta}^D}}{\partial \Delta\gamma} & \frac{\partial R_{\boldsymbol{\beta}^D}}{\partial p} & \frac{\partial R_{\boldsymbol{\beta}^D}}{\partial \boldsymbol{\beta}^D} & \frac{\partial R_{\boldsymbol{\beta}^D}}{\partial \beta^V} \\ \frac{\partial R_{\beta^V}}{\partial \mathbf{S}} & \frac{\partial R_{\beta^V}}{\partial \bar{\varepsilon}^p} & \frac{\partial R_{\beta^V}}{\partial \Delta\gamma} & \frac{\partial R_{\beta^V}}{\partial p} & \frac{\partial R_{\beta^V}}{\partial \boldsymbol{\beta}^D} & \frac{\partial R_{\beta^V}}{\partial \beta^V} \end{bmatrix}^{k} \begin{bmatrix} \delta_{\mathbf{S}} \\ \delta_{\bar{\varepsilon}^p} \\ \delta_{\Delta\gamma} \\ \delta_{p} \\ \delta_{\boldsymbol{\beta}^D} \\ \delta_{\beta^V} \end{bmatrix}^{k+1} = - \begin{bmatrix} R_{\mathbf{S}} \\ R_{\bar{\varepsilon}^p} \\ R_{\Delta\gamma} \\ R_{p} \\ R_{\boldsymbol{\beta}^D} \\ R_{\beta^V} \end{bmatrix}^{k}, \tag{4.24}$$

in which $\delta_{(.)}$ is the increment of the unknowns $(\cdot)$:

$$(\cdot)^{k+1} = (\cdot)^{k} + \delta^{k+1}_{(\cdot)}. \tag{4.25}$$

The linear system (4.24) is iteratively solved until a converge criterion is satisfied. The stop condition chosen is based on the residuals norm:

$$\text{Error} = \sum_{i=1}^{k} \left\| \frac{R_{x_i}}{x_i} \right\|, \tag{4.26}$$

where x_i represents the $i-$th system unknown.

When Error is lesser or equal to a given tolerance ϵ, convergence is achieved, the internal variables and their power-conjugates are updated and the numerical methodology

continues. The explicit computation of the derivatives present in the coefficient matrix in Eq.(4.24) can be found on the appendix of this work.

4.2 Consistent Tangent Operator

To solve the global equilibrium equations generated by the Finite Element Method, one needs to construct the elements stiffness matrix K^{el}, which is later used to assemble global stiffness matrix K. The assembly of K^{el} requires the computation of the consistent tangent operator $\mathbb{D}$:

$$\mathbb{D} = \frac{\partial \boldsymbol{\sigma}_{n+1}}{\partial \boldsymbol{\varepsilon}_{n+1}}. \tag{4.27}$$

Only a limited number of constitutive elastoplastic models possess a closed form of $\mathbb{D}$, and hence a numerical approach is advisable for more general formulations. In this regard, one follows the framework presented in de Souza Neto et al. (2011).

First, if the elasticity assumption of the trial state is true, then no hardening takes place, and $\mathbb{D}$ is simply the elasticity tensor $\mathbb{D}^e$. Thus:

$$\mathbb{D} = \mathbb{D}^e. \tag{4.28}$$

Nevertheless, if plastic flow occurred the derivative (4.27) is not easily computed. If $\hat{\boldsymbol{\sigma}}$ denotes the algorithmic stress update function in the plastic corrector phase, it follows:

$$\mathbb{D} = \mathbb{D}^{ep} = \frac{\partial \boldsymbol{\sigma}_{n+1}}{\partial \boldsymbol{\varepsilon}_{n+1}} = \frac{\partial \hat{\boldsymbol{\sigma}}}{\partial \boldsymbol{\varepsilon}_{n+1}}, \tag{4.29}$$

with $\mathbb{D}^{ep}$ representing the elastoplastic tangent. It is possible to show that (de Souza Neto et al., 2011):

$$\mathbb{D}^{ep} = \frac{\partial \boldsymbol{\sigma}_{n+1}}{\partial \boldsymbol{\varepsilon}_{n+1}} = \frac{\partial \boldsymbol{\sigma}_{n+1}}{\partial \boldsymbol{\varepsilon}^{eT}_{n+1}}. \tag{4.30}$$

One way to calculate Eq.(4.30) is by a consistent linearization of the nonlinear system (4.21) (de Souza Neto et al., 2011). Before that, it is important to observe the following relation:

$$\mathbb{D}^{ep} = \frac{\partial \boldsymbol{S}_{n+1}}{\partial \boldsymbol{\varepsilon}^{eT}_{n+1}} + \boldsymbol{I} \otimes \frac{\partial p_{n+1}}{\partial \boldsymbol{\varepsilon}^{eT}_{n+1}}. \tag{4.31}$$

Further, the expressions:

$$\begin{cases} d\boldsymbol{S}_{n+1}^{T} = 2Gd\boldsymbol{\varepsilon}_{n+1}^{eDT} = 2G\mathbb{I}^{D} \colon d\boldsymbol{\varepsilon}_{n+1}^{eT}, \\ dp_{n+1}^{T} = Kd\varepsilon_{n+1}^{VT} = K\boldsymbol{I} \colon d\boldsymbol{\varepsilon}_{n+1}^{eT}, \end{cases} \tag{4.32}$$

are useful to determine $\mathbb{D}^{ep}$, with $\boldsymbol{\varepsilon}_{n+1}^{eDT}$ and $\varepsilon_{n+1}^{VT}\boldsymbol{I}$ denoting the deviatoric and volumetric parts of $\boldsymbol{\varepsilon}_{n+1}^{eT}$, while d represents the differential operator.

The consistent linearization of Eq.(4.21) leads to the linear system:

$$\begin{bmatrix} \frac{\partial R_{\mathbf{S}}}{\partial \mathbf{S}} & \frac{\partial R_{\mathbf{S}}}{\partial \bar{\varepsilon}^{p}} & \frac{\partial R_{\mathbf{S}}}{\partial \Delta\gamma} & \frac{\partial R_{\mathbf{S}}}{\partial p} & \frac{\partial R_{\mathbf{S}}}{\partial \boldsymbol{\beta}^{D}} & \frac{\partial R_{\mathbf{S}}}{\partial \beta^{V}} \\ \frac{\partial R_{\bar{\varepsilon}^{p}}}{\partial \mathbf{S}} & \frac{\partial R_{\bar{\varepsilon}^{p}}}{\partial \bar{\varepsilon}^{p}} & \frac{\partial R_{\bar{\varepsilon}^{p}}}{\partial \Delta\gamma} & \frac{\partial R_{\bar{\varepsilon}^{p}}}{\partial p} & \frac{\partial R_{\bar{\varepsilon}^{p}}}{\partial \boldsymbol{\beta}^{D}} & \frac{\partial R_{\bar{\varepsilon}^{p}}}{\partial \beta^{V}} \\ \frac{\partial R_{\Delta\gamma}}{\partial \mathbf{S}} & \frac{\partial R_{\Delta\gamma}}{\partial \bar{\varepsilon}^{p}} & \frac{\partial R_{\Delta\gamma}}{\partial \Delta\gamma} & \frac{\partial R_{\Delta\gamma}}{\partial p} & \frac{\partial R_{\Delta\gamma}}{\partial \boldsymbol{\beta}^{D}} & \frac{\partial R_{\Delta\gamma}}{\partial \beta^{V}} \\ \frac{\partial R_{p}}{\partial \mathbf{S}} & \frac{\partial R_{p}}{\partial \bar{\varepsilon}^{p}} & \frac{\partial R_{p}}{\partial \Delta\gamma} & \frac{\partial R_{p}}{\partial p} & \frac{\partial R_{p}}{\partial \boldsymbol{\beta}^{D}} & \frac{\partial R_{p}}{\partial \beta^{V}} \\ \frac{\partial R_{\boldsymbol{\beta}^{D}}}{\partial \mathbf{S}} & \frac{\partial R_{\boldsymbol{\beta}^{D}}}{\partial \bar{\varepsilon}^{p}} & \frac{\partial R_{\boldsymbol{\beta}^{D}}}{\partial \Delta\gamma} & \frac{\partial R_{\boldsymbol{\beta}^{D}}}{\partial p} & \frac{\partial R_{\boldsymbol{\beta}^{D}}}{\partial \boldsymbol{\beta}^{D}} & \frac{\partial R_{\boldsymbol{\beta}^{D}}}{\partial \beta^{V}} \\ \frac{\partial R_{\beta^{V}}}{\partial \mathbf{S}} & \frac{\partial R_{\beta^{V}}}{\partial \bar{\varepsilon}^{p}} & \frac{\partial R_{\beta^{V}}}{\partial \Delta\gamma} & \frac{\partial R_{\beta^{V}}}{\partial p} & \frac{\partial R_{\beta^{V}}}{\partial \boldsymbol{\beta}^{D}} & \frac{\partial R_{\beta^{V}}}{\partial \beta^{V}} \end{bmatrix} \begin{bmatrix} d\boldsymbol{S}_{n+1} \\ d\bar{\varepsilon}_{n+1}^{p} \\ d\Delta\gamma \\ dp_{n+1} \\ d\boldsymbol{\beta}_{n+1}^{D} \\ d\beta_{n+1}^{V} \end{bmatrix} = \begin{bmatrix} 2G\mathbb{I}^{D} \colon d\boldsymbol{\varepsilon}_{n+1}^{eT} \\ 0 \\ 0 \\ K\mathbf{I} \colon d\boldsymbol{\varepsilon}_{n+1}^{eT} \\ \mathbf{0} \\ 0 \end{bmatrix}, \tag{4.33}$$

or equivalently:

$$\begin{bmatrix} d\boldsymbol{S}_{n+1} \\ d\bar{\varepsilon}_{n+1}^{p} \\ d\Delta\gamma \\ dp_{n+1} \\ d\boldsymbol{\beta}_{n+1}^{D} \\ d\beta_{n+1}^{V} \end{bmatrix} = \begin{bmatrix} \mathbb{C}_{11} & \mathbf{C}_{12} & \mathbf{C}_{13} & \mathbf{C}_{14} & \mathbb{C}_{15} & \mathbf{C}_{16} \\ \mathbf{C}_{21} & C_{22} & C_{23} & C_{24} & \mathbf{C}_{25} & C_{26} \\ \mathbf{C}_{31} & C_{32} & C_{33} & C_{34} & \mathbf{C}_{35} & C_{36} \\ \mathbf{C}_{41} & C_{42} & C_{43} & C_{44} & \mathbf{C}_{45} & C_{46} \\ \mathbb{C}_{51} & \mathbf{C}_{52} & \mathbf{C}_{53} & \mathbf{C}_{54} & \mathbb{C}_{55} & \mathbf{C}_{56} \\ \mathbf{C}_{61} & C_{62} & C_{63} & C_{64} & \mathbf{C}_{65} & C_{66} \end{bmatrix} \begin{bmatrix} 2G\mathbb{I}^{D} \colon d\boldsymbol{\varepsilon}_{n+1}^{eT} \\ 0 \\ 0 \\ K\mathbf{I} \colon d\boldsymbol{\varepsilon}_{n+1}^{eT} \\ \mathbf{0} \\ 0 \end{bmatrix}, \tag{4.34}$$

where:

$$\begin{bmatrix} \mathbb{C}_{11} & \mathbf{C}_{12} & \mathbf{C}_{13} & \mathbf{C}_{14} & \mathbb{C}_{15} & \mathbf{C}_{16} \\ \mathbf{C}_{21} & C_{22} & C_{23} & C_{24} & \mathbf{C}_{25} & C_{26} \\ \mathbf{C}_{31} & C_{32} & C_{33} & C_{34} & \mathbf{C}_{35} & C_{36} \\ \mathbf{C}_{41} & C_{42} & C_{43} & C_{44} & \mathbf{C}_{45} & C_{46} \\ \mathbb{C}_{51} & \mathbf{C}_{52} & \mathbf{C}_{53} & \mathbf{C}_{54} & \mathbb{C}_{55} & \mathbf{C}_{56} \\ \mathbf{C}_{61} & C_{62} & C_{63} & C_{64} & \mathbf{C}_{65} & C_{66} \end{bmatrix} = \begin{bmatrix} \frac{\partial R_{\mathbf{S}}}{\partial \mathbf{S}} & \frac{\partial R_{\mathbf{S}}}{\partial \bar{\varepsilon}^{p}} & \frac{\partial R_{\mathbf{S}}}{\partial \Delta\gamma} & \frac{\partial R_{\mathbf{S}}}{\partial p} & \frac{\partial R_{\mathbf{S}}}{\partial \boldsymbol{\beta}^{D}} & \frac{\partial R_{\mathbf{S}}}{\partial \beta^{V}} \\ \frac{\partial R_{\bar{\varepsilon}^{p}}}{\partial \mathbf{S}} & \frac{\partial R_{\bar{\varepsilon}^{p}}}{\partial \bar{\varepsilon}^{p}} & \frac{\partial R_{\bar{\varepsilon}^{p}}}{\partial \Delta\gamma} & \frac{\partial R_{\bar{\varepsilon}^{p}}}{\partial p} & \frac{\partial R_{\bar{\varepsilon}^{p}}}{\partial \boldsymbol{\beta}^{D}} & \frac{\partial R_{\bar{\varepsilon}^{p}}}{\partial \beta^{V}} \\ \frac{\partial R_{\Delta\gamma}}{\partial \mathbf{S}} & \frac{\partial R_{\Delta\gamma}}{\partial \bar{\varepsilon}^{p}} & \frac{\partial R_{\Delta\gamma}}{\partial \Delta\gamma} & \frac{\partial R_{\Delta\gamma}}{\partial p} & \frac{\partial R_{\Delta\gamma}}{\partial \boldsymbol{\beta}^{D}} & \frac{\partial R_{\Delta\gamma}}{\partial \beta^{V}} \\ \frac{\partial R_{p}}{\partial \mathbf{S}} & \frac{\partial R_{p}}{\partial \bar{\varepsilon}^{p}} & \frac{\partial R_{p}}{\partial \Delta\gamma} & \frac{\partial R_{p}}{\partial p} & \frac{\partial R_{p}}{\partial \boldsymbol{\beta}^{D}} & \frac{\partial R_{p}}{\partial \beta^{V}} \\ \frac{\partial R_{\boldsymbol{\beta}^{D}}}{\partial \mathbf{S}} & \frac{\partial R_{\boldsymbol{\beta}^{D}}}{\partial \bar{\varepsilon}^{p}} & \frac{\partial R_{\boldsymbol{\beta}^{D}}}{\partial \Delta\gamma} & \frac{\partial R_{\boldsymbol{\beta}^{D}}}{\partial p} & \frac{\partial R_{\boldsymbol{\beta}^{D}}}{\partial \boldsymbol{\beta}^{D}} & \frac{\partial R_{\boldsymbol{\beta}^{D}}}{\partial \beta^{V}} \\ \frac{\partial R_{\beta^{V}}}{\partial \mathbf{S}} & \frac{\partial R_{\beta^{V}}}{\partial \bar{\varepsilon}^{p}} & \frac{\partial R_{\beta^{V}}}{\partial \Delta\gamma} & \frac{\partial R_{\beta^{V}}}{\partial p} & \frac{\partial R_{\beta^{V}}}{\partial \boldsymbol{\beta}^{D}} & \frac{\partial R_{\beta^{V}}}{\partial \beta^{V}} \end{bmatrix}^{-1}. \tag{4.35}$$

Therefore, it follows from Eq.(4.34):

$$\begin{cases} \dfrac{\partial \boldsymbol{S}_{n+1}}{\partial \boldsymbol{\varepsilon}_{n+1}^{eT}} = 2G\mathbb{C}_{11} \colon \mathbb{I}^{D} + K\mathbf{C}_{14} \otimes \boldsymbol{I}, \\ \dfrac{\partial p_{n+1}}{\partial \boldsymbol{\varepsilon}_{n+1}^{eT}} = 2G\mathbf{C}_{41} \colon \mathbb{I}^{D} + KC_{44}\boldsymbol{I}, \end{cases} \tag{4.36}$$

which completes the computation of $\mathbb{D}^{ep}$ according to Eq.(4.31). At this point, two remarks are important:

- the systems (4.24) and (4.33) share the same coefficient matrices. This feature illustrates one of the benefits of the implicit scheme used, since the referf matrix is computed in the state update phase;
- the assembly of the consistent tangent operator occurs after the state update procedure, since $\mathbb{D}$ requires the updated internal variables for its calculation.

The presented framework was also implement in HYPLAS via user defined subroutine.

4.3 Meshes and Boundary Conditions

Mesh definition is vital for the numerical solution of the Boundary Value Problem (BVP) since the mesh represents the spatial discretization of the BVP domain. In this dissertation, the butterfly and smooth cylindrical specimens of SAE 1045 steel investigated by Bai (2008) were simulated in HYPLAS. The meshing of these specimens was conducted with aid of the Evaluation version of the software GiD®. In the next lines, one presents the mesh options used for each geometry, as well as the boundary conditions applied in the simulations.

4.3.1 Butterfly Specimen Mesh

After a preliminary analysis, one opts to use a mesh formed by quadratic 10-noded tetrahedric elements to mesh the butterfly specimen. This decision was based on the computational time spent during each simulation test. The best trade-off relation was achieved with a mesh of 1654 quadratic 10-noded tetrahedral elements (TETRA10 in HYPLAS) and 3588 nodes. Regardless of being relatively coarse, this mesh is suitable for the purposes of this work. The mesh constructed is displayed in Fig.4.1.

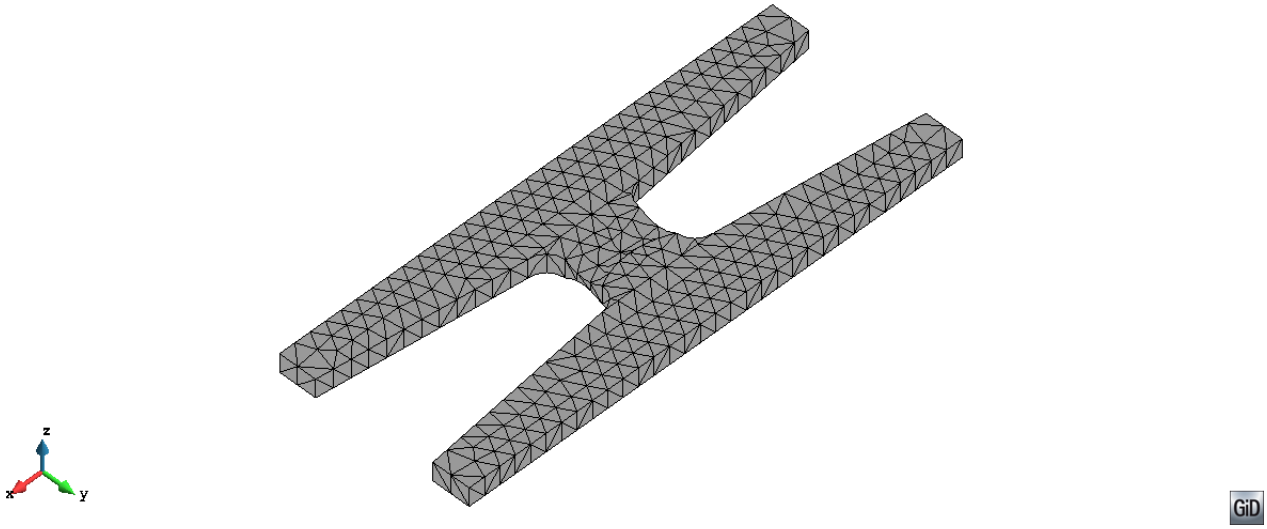

Figure 4.1 – Butterfly specimen mesh used in the Finite Elements simulations.

Figure 4.2 displays the location where boundary conditions are applied in the Finite Elements simulations. The nodes on the top "shoulder" are subjected to some prescribed horizontal and/or vertical displacement, while the nodes at the bottom are fixed.

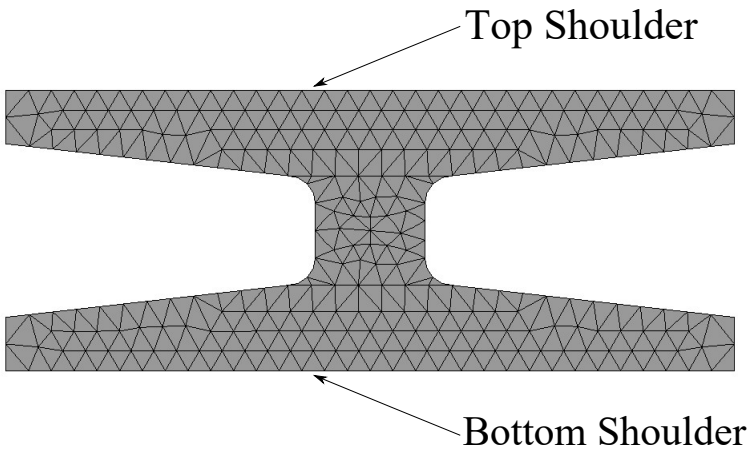

Figure 4.2 – Location of the regions where the boundary conditions are applied on butterfly specimens simulations.

Details about the geometry (e.g. dimensions) of the butterfly specimen can be found in Bai (2008). According to Bai (2008), the crack initiation was experimentally observed in the central region of the gauge section of the butterfly specimen for the majority of the tests. Therefore, a node in the referred region is selected for extracting local quantities (e.g accumulated plastic strain).

4.3.2 Smooth Cylindrical Specimen

Supported by previous works (see Malcher et al. (2020) and Morales (2020)), one uses a mesh with 690 elements and 2177 quadratic 8-noded quadrilateral elements (QUAD8

in HYPLAS). The resulting mesh is presented Fig.4.3, and further information about the specimen dimensions can be found in Bai (2008).

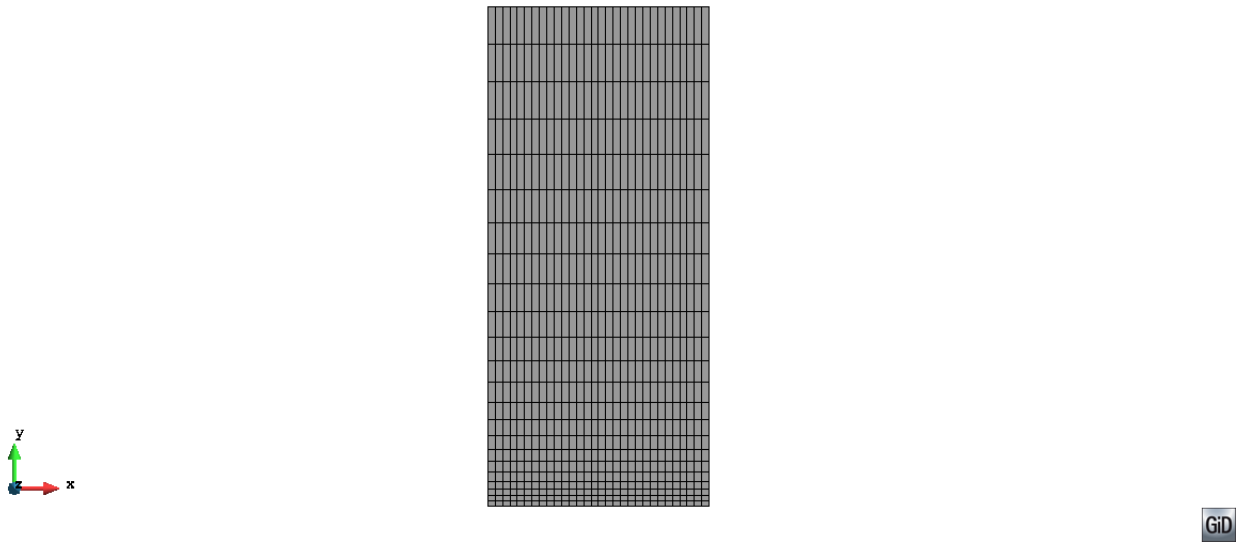

Figure 4.3 – Smooth cylindrical specimen mesh used in the Finite Elements simulations.

As Fig.4.3 demonstrates, only one fourth of the specimen gauge section is modeled due to its symmetry around its main axis. Figure 4.4 presents the boundary conditions employed in the Finite Elements simulations.

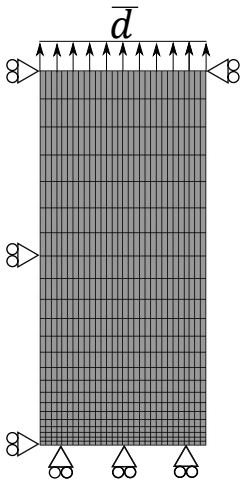

Figure 4.4 – Boundary conditions applied on smooth cylindrical specimens simulations .

A vertical prescribed displacement $\bar{d}$ is applied on the top nodes, while the nodes at the bottom are only free to move on the horizontal direction to emulate Poisson's effect. The nodes on the left side of the boundary are horizontally constrained. This geometry is important for the calibration of the hardening law, as it is used in the optimization technique.

4.4 Simulations at the Gauss Point

For some cyclic plasticity applications, such LCF regime, one can simulate the stress-strain hysteris loop at the Gauss level, which makes modeling process much easier as the complete FEM simulation. Low Cycle Fatigue data usually provide not only the loading path tested (see Leese and Socie (1989) for instance), but also the strain and stress amplitudes, and the fatigue life N_f.

In this regard, these simplified simulations were performed by taking advantage of the state update subroutine coded in HYPLAS. This code was adapted to MATLAB®, and receives experimental strain amplitude applied, as well as the material parameters, to carry out the calculations. The code accepts a number of proportional and non-proportional loading paths, which must be informed by the user.

4.5 Material Parameters by an Optimization Technique

Any constitutive model performance depends to a great extent on how well-calibrated its parameters are. This is especially critical for Ductile Fracture since the material elastoplastic behavior prediction relies on the identification of the hardening law parameters. One way to this is by conducting a standard tensile test on a smooth cylindrical specimen and treat the force F versus displacement d data (also called reaction curve) to extract the experimental hardening curve. With this information, one may carry out some fitting method using the hardening law as the model function on this curve to obtain the fitting parameters.

However, this approach shows limitations to describe the experimental reaction curve notably after the specimen necking, which is a phenomenon characterized by a dramatic reduction of the gauge cross-section. This inaccuracy is explained by the fact that at the neck region, the material response deviates considerably from the average cross-sectional behavior assumed by the previously mentioned calibration technique (Bai, 2008; Malcher et al., 2012; Machado and Malcher, 2019; Malcher et al., 2020).

Inverse methodologies are suitable options to overcome this issue (Kleinermann and Ponthot, 2003; Machado and Malcher, 2019), as the nonlinearities and necking are considered in the optimization procedure. In this regard, one uses such approach to calibrate the four parameters of the Kleinermann and Ponthot (2003) hardening law. The key idea of the performed technique is presented in Fig.4.5.

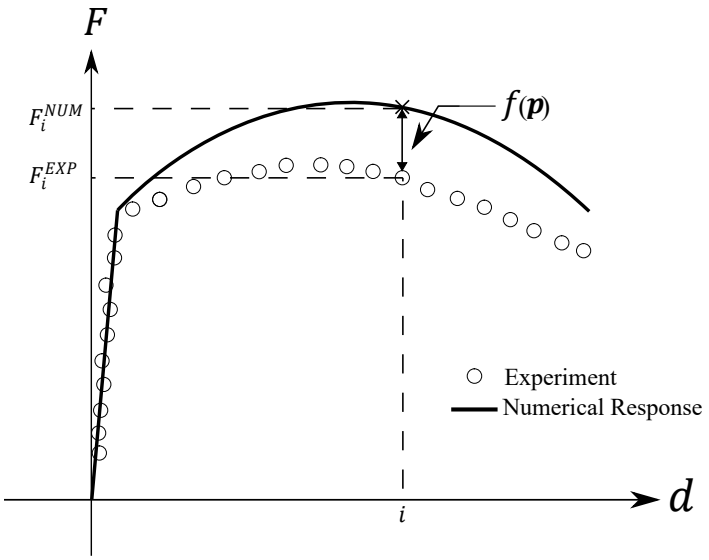

Figure 4.5 – Difference between the numerical and experimental reaction curves and the objective function.

The FEM method predicts the numerical force F^{NUM} versus displacement curve based on a set of input parameters $\mathbf{p}$, which will not in general accurately describe the experimental curve. To correct this discrepancy, one needs to minimize the following objective function $f(\mathbf{p})$:

$$f(\mathbf{p}) = \sqrt{\frac{1}{N}\sum_{i=1}^{N}\left(\frac{F_i^{NUM}(\mathbf{p}) - F_i^{EXP}}{F_i^{EXP}}\right)^2}, \tag{4.37}$$

where F^{EXP} and N denotes the experimental forces and number of data points, respectively. It is worth observing that the objective function (4.37) chosen is a least-squares type. The optimization problem consists of finding the optimal parameters set $\mathbf{p}^*$ that minimizes f . To do so, one uses an optimization MATLAB code, linked with HYPLAS, developed by Machado and Malcher (2019). The hardening law used in the Finite Elements simulation is given in Eq.(3.22) and thus:

$$\mathbf{p} = \begin{bmatrix}\sigma_{y0} & \omega & \sigma_\infty & \delta\end{bmatrix} \tag{4.38}$$

To start the optimization iterations, an initial set $\mathbf{p}_0$ is needed, and one possible initial guess is set obtained by the fitting approach. Finally, the calibration process is conducted with $a = b = 0$, $H^K = 0$ and $b^K = 0$. In other words, it is an von Mises with isotropic hardening based calibration.

5 Material and Experimental Data

The SAE 1045 steel was the material chosen for the evaluation of the stress invariants effects. This alloy possess a considerably large amount of Ductile Fracture, Ultra-Low and Low Cycle Fatigue data available in the literature, besides from its industrial relevance. For example, this alloy is important in machining process, both as a cutting tool and as the machined material for engineering applications Courbon et al. (2013); Singh et al. (2021). Moreover, SAE 1045 steel is widely used in the manufacture vehicle shafts and in structural engineering (Leese and Socie, 1989; Thompson et al., 2021).

Regarding data on SAE 1045 steel, Bai (2008) performed monotonic and cyclic tests on SAE 1045 steel butterfly specimens, while Leese and Socie (1989) provide an extensive report with LCF data for this steel alloy. These 2 contributions were the base for the experimental data used to evaluate the performance of the model presented in Chapter 3 and for parameters calibration. In the next lines, one briefly details the main features and information in each work. Finally, the material parameters obtained by the data analysis will be presented.

5.1 Ductile Fracture and Ultra-Low Cycle Experiments from Bai (2008)

Bai (2008) conducted a series of monotonic and ULCF tests on butterfly specimens to investigate the effects of η and θ on SAE 1045 steel behavior. All the tests were displacement controlled and carried out until fracture. Figure 5.1 displays schematically how these experiments were elaborated and some of the load conditions considered.

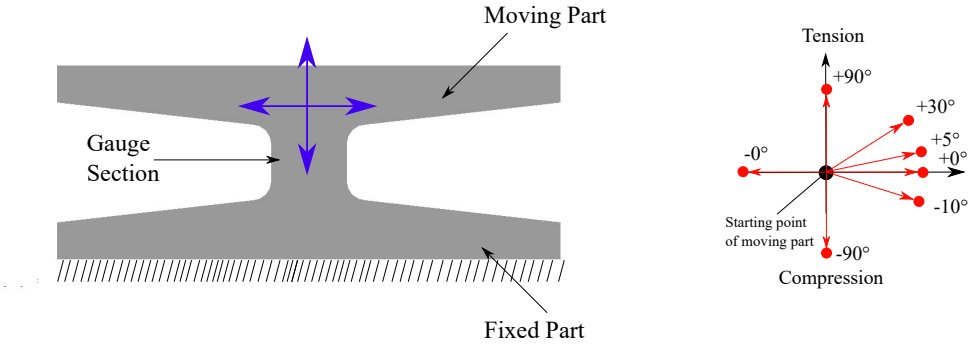

Figure 5.1 – Experiments performed on SAE 1045 butterfly specimens. On the left, the specimen regions that are fixed and where the prescribed displacement are applied. On the right, the loading directions investigated. Adapted from Bai (2008).

The butterfly geometry is especially useful for the study of materials pressure and third invariant dependence because it allows covering a wide range of η and ξ (or θ) values with a single specimen shape. For instance, approximate uniaxial tensile conditions ($\eta \geq 1/3$ and $\xi = 1$) can be obtained for vertical loads ($\pm 90°$ directions in Fig.5.1), and shear ($\eta \geq 0$ and $\xi = 0$) with horizontal loads ($\pm 0°$ directions in Fig.5.1). Combined scenarios can be achieved by varying the angle between the applied load direction and specimens moving part ($+30°$ direction in Fig.5.1 for example).

Besides the butterfly specimens, Bai (2008) performed similar experiments with other geometries, one the them the standard smooth cylindrical specimen, which is important to calibrate the hardening law. Table 5.1 presents the displacements to fracture of the monotonic tests considered in this dissertation.

Table 5.1 – Experimental displacements to fracture of the monotonic tests conducted by Bai (2008).

Test	Vertical Displacement to Fracture (mm)	Horizontal Displacement to Fracture (mm)
Smooth Cylindrical	1.54	-
Butterfly $+90°$	0.10	-
Butterfly $+0°$	-	1.15
Butterfly $+30°$	0.22	0.12
Butterfly $+5°$	0.40	0.04

Furthermore, Table 5.2 displays the displacement ranged of the cyclic tests (ULCF regime) carried out by Bai (2008).

Table 5.2 – Displacement ranges used in the cyclic tests conducted by Bai (2008).

Cyclic Test	Minimum Displacement (mm)	Maximal Displacement (mm)
Compression-Tension 1 $(-90°\text{to}+90°)$	-0.06	0.01
Compression-Tension 2 $(-90°\text{to}+90°)$	-0.15	0.06
Shear-Shear 1 $(-0°\text{to}+0°)$	-0.50	0.81
Shear-Shear 2 $(-0°\text{to}+0°)$	-0.71	0.81

The data contained in Tables 5.1 and 5.2 are used to assemble the boundary conditions for the Finite Elements simulations.

5.2 Low Cycle Fatigue Experiments from Leese and Socie (1989)

Leese and Socie (1989) performed a series of strain-controlled cyclic tests on SAE 1045 steel smooth cylindrical and thin walled specimens. This latter specimen allows to compute an analytical estimation of the shear stress amplitude in pure torsion experiments.

A number of proportional and nonproportional loading paths with different loading ratios R_a were investigated, and the data (calculated stress amplitudes and crack initiation fatigue life) from each test recorded. Table 5.3 shows the axial strain amplitudes ε_a, the calculated axial stress amplitudes σ_a for each test performed at ε_a, and the mean axial stress amplitude $\bar{\sigma}_a$ for the set of experiments carried out at ε_a for fully reversed $R_a = -1$ axial tests.

Table 5.3 – Data from the fully reversed cyclic axial tests conducted by Leese and Socie (1989).

ε_a (%)	σ_a (MPa)	$\bar{\sigma}_a$ (MPa)
2.00	524.0	524.0
1.50	499.0	499.0
1.00	465.0 452.0	458.5
0.80	440.0 445.0	442.5
0.60	420.0 440.0	430.0
0.50	372.0	372.0
0.40	353.0 351.0 360.0	354.7
0.30	315.0	354.7
0.25	302.0 298.0	300.0
0.2	269.9 270.0 274.0 280.0	273.2
0.15	241.0	241.0

Table 5.4 displays the shear strain amplitudes γ_a, the calculated shear stress amplitudes τ_a for each experiment performed at γ_a, and the mean axial stress amplitude $\bar{\tau}_a$ for the set of experiments carried out at γ_a for fully reversed $R_a = -1$ pure torsion tests.

Table 5.4 – Data from the fully reversed cyclic torsion tests conducted by Leese and Socie (1989).

γ_a (%)	τ_a (MPa)	$\bar{\tau}_a$ (MPa)
2.50	270.0 270.0 259.0	266.3
1.73	251.0 248.0	249.5
1.50	232.0 237.0 232.0	233.7
0.82	194.0 200.0 198.0	197.3
0.72	196.0	196.0
0.50	161.0 168.0 165.0	164.7
0.40	160.0 159.0 154.0	156.0
0.38	155.0 164.0 163.0	160.7
0.30	148.0	148.0

5.3 Material Parameters Identification by Data from Bai (2008)

To properly run the numerical model presented in Chapter 4, one needs to calibrate some material parameters namely: the Young or Elasticity Modulus E, Poisson's ratio ν, the Kleinermann and Ponthot (2003) σ_{y0}, ω, σ_∞, δ and the kinematic hardening H^K and b^K parameters, as well as, Gao's constants a and b. All of them can be identified from the monotonic and cyclic data from Bai (2008).

5.3.1 Calibration of Elasticity and Isotropic Hardening Law Parameters

The identification of E, ν, σ_{y0}, ω, σ_∞, and δ was conducted supported by the monotonic data. In this regard, the reaction curve from the tension test on the smooth cylindrical specimen is analyzed. It is assumed that $\nu = 0.3$, which is a common assumption for metallic materials (Leese and Socie, 1989; Lemaitre and Chaboche, 1994; Bai, 2008). Next, one converts the force F versus displacement d curve into a engineering stress σ versus engineering strain ε graph. Carrying out a linear regression on linear portion of the transformed plot, one obtains $E = 178.9\,\text{GPa}$.

To start the optimization process detailed in Chapter 4, one needs to extracts the experimental hardening curve for the estimation of the initial guess $\mathbf{p}_0$. To do so, first the initial monotonic yield stress σ_{y0} is estimated through the 0.2%-strain technique, which furnishes, $\sigma_{y0} = 813.9\,\text{MPa}$, enabling the extraction of the experimental hardening curve. Further, this curve is transformed to true measures by the relations:

$$\begin{cases} \sigma_v = \sigma\,(1+\varepsilon)\,, \\ \varepsilon_v = \ln\,(1+\varepsilon)\,, \end{cases} \tag{5.1}$$

with σ_v and ε_v respectively denoting the true stress and true strain. Equations (5.1) are valid until necking, and hence the transformed curve starts from σ_{y0} to the last experimental point prior to necking. Carrying out a nonlinear regression on the experimental σ_v versus ε_v hardening curve using Eq.(3.22) as the model function, one arrives at:

$$\mathbf{p}_0 = \begin{bmatrix} 813.9 & 289.0 & 887.3 & 291.1 \end{bmatrix} \tag{5.2}$$

By the end of the optimization process, the converged set $\mathbf{p}^*$ is:

$$\mathbf{p}^* = \begin{bmatrix} 725.0 & 347.6 & 890.4 & 405.5 \end{bmatrix} \tag{5.3}$$

Figure 5.2 displays graphically the result from the opmization methodology.

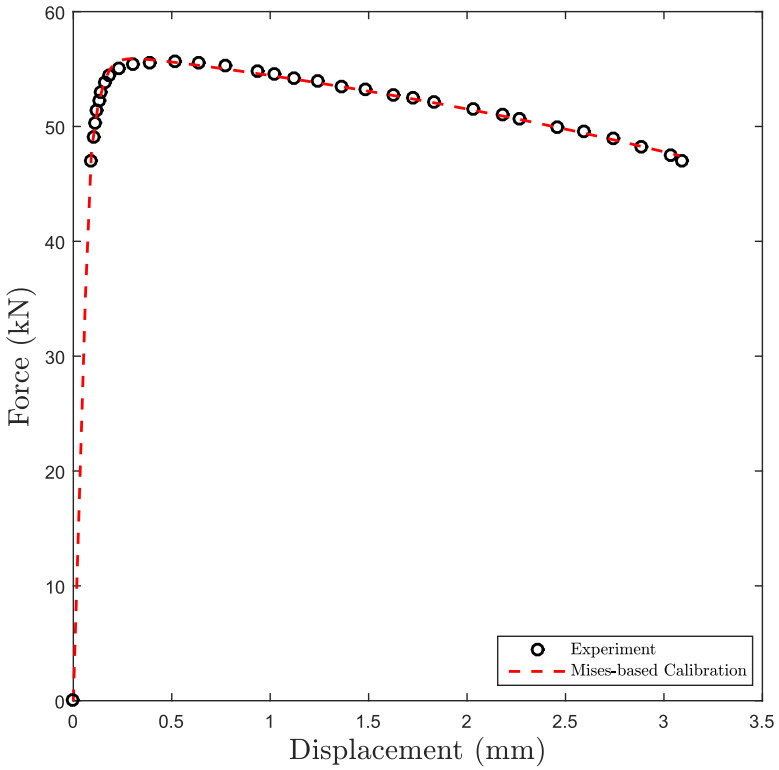

Figure 5.2 – Calibration of the hardening law parameters.

Since the accumulated plastic strain at the end of the simulation $\bar{\varepsilon}_f^p = 0.49$, the hardening law defined by the set (5.3) is valid up this value.

5.3.2 Calibration of the Kinematic Hardening Parameters

The calibration of kinematic hardening parameters rely on the kinematic hardening curve, which is obtained by performing a series of cyclic tests with different strain (or displacement) amplitudes. Bai (2008) conducted this test and furnished the experimental kinematic hardening curve for SAE 1045 Steel within the range of strain amplitudes investigated.

The calibration of H^K and b^K can be accomplished by a nonlinear regression on the experimental kinematic harderning curve, which is composed of set of pairs of stress σ_a and plastic strain $\bar{\varepsilon}_a^p$ amplitudes. First, it is possible to show that Eq.(3.25) may be redefined as:

$$\sigma_a = \sigma_{y0} + \frac{H^K}{b^K} \tanh\left(b^K \bar{\varepsilon}_a^p\right), \tag{5.4}$$

where is this case σ_{y0} is the cyclic yield strength. It is assumed that the cyclic yield stress is negligible with respect to the monotonic one in ULCF conditions, and hence can be taken as 0 in Eq.(5.4). Figure 5.3 shows graphically the result of the calibration based on Eq.(5.3).

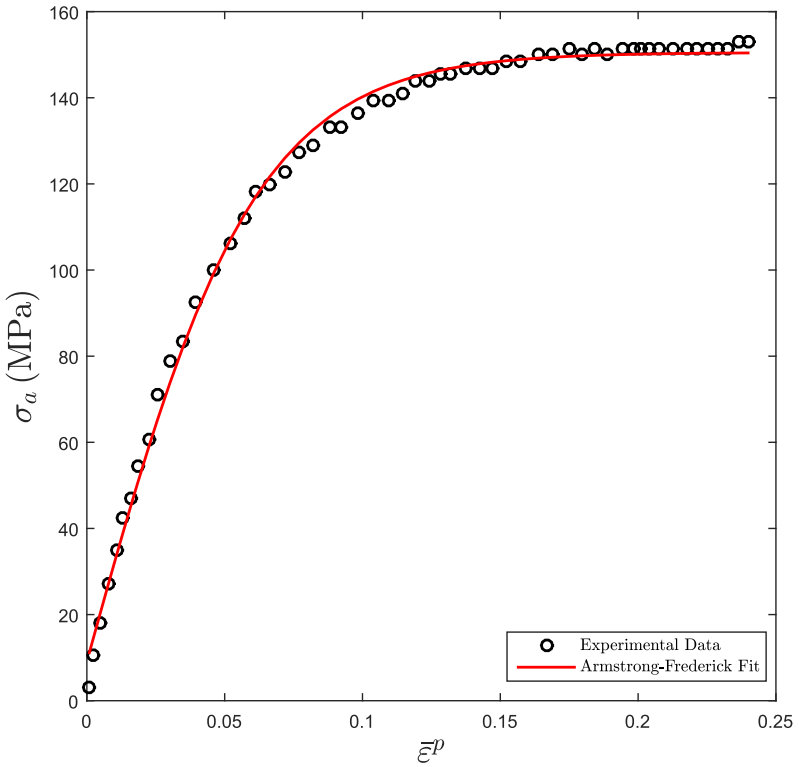

Figure 5.3 – Graphical result of the calibration of H^K and b^K in ULCF conditions.

The identified parameters were $H^K = 2319.1\,\text{MPa}$ and $b^K = 16.4$. Table 5.5 summarizes the material parameters identified.

Table 5.5 – Material parameters calibrated for the SAE 1045 in Monotonic and ULCF conditions based on the data from Bai (2008).

Parameter	Value
Elasticity Modulus E	178.9 GPa
Poisson's Ratio ν	0.3
Monotonic Yield Stress σ_{y0}	725.0 MPa
ω	347.6 MPa
σ_∞	890.4 MPa
δ	405.5
Kinematic Hardening Modulus H^K	2319.1 MPa
Saturation Coefficient b^K	16.4

5.3.3 Calibration of Gao's a and b Parameters

The identification of a and b require two calibration points. First, to calibrate a one uses a test in which the first invariant has an important influence, such as the tension test in the butterfly specimen, identified as "Butterfly +90°" in Table 5.1. Conversely, to calibrate b, a shear-predominant experiment is suitable, such as the horizontal tension test on the butterfly specimen, identified as "Butterfly +0°" in Table 5.1.

In this regard, a trial an error methodology was used to identify this two parameters. First, the horizontal tension test is analyzed to calibrate b, since the first invariant (and hence a) has a minor influence in shear situations. Once set a b value, the "Butterfly +90°" experiment is considered to identify a. The results are discussed in more details in Chapter 6.

Next, the values of a and b calculated via this process are used to simulate the ULCF experiments. If the numerical responses describe properly the ULCF tests, then a and b monotonically calibrated are suitable for these load conditions, otherwise a recalibration is conducted to compute new a and b following the same steps described previously for the monotonic case.

5.4 Material Parameters Identification by Data from Leese and Socie (1989)

In Low Cycle Fatigue conditions, only kinematic hardening is considered for modeling purposes, and thus, the kinematic parameters need to be identified. However, one cannot expect the values achieved for H^K and b^K in Table 5.5 to be same as if they were obtained by the data in Tables 5.3 and 5.4 because LCF and ULCF are different phenomenons. Therefore, one need to recalibrate H^K and b^K. Besides, the Young modulus computed by Leese and Socie (1989) was $E = 202.0$ GPa.

5.4.1 Calibration of the Kinematic Hardening Parameters

The strategy used was the same employed to identify H^K and b^K in previous the section. The main difference consist of the data set considered to perform the nonlinear regression with Eq.(5.4), and the cyclic initial yield stress cannot be neglected.

Firstly, the cyclic Ramberg-Osgood expression:

$$\sigma_a = K' \left(\bar{\varepsilon}_a^p\right)^{n'} , \tag{5.5}$$

with K' and n' are the cyclic hardening modulus and cyclic hardening exponent, is useful to calibrate Eq.(5.4). The linearization of Eq.(5.5) followed by a linear regression on the

data in Table 5.3 allows to compute K' and n'. The values obtained were K'=1255.1 MPa and n'=0.21, and Fig.5.4 illustrates the Ramberg-Osgood curve generated.

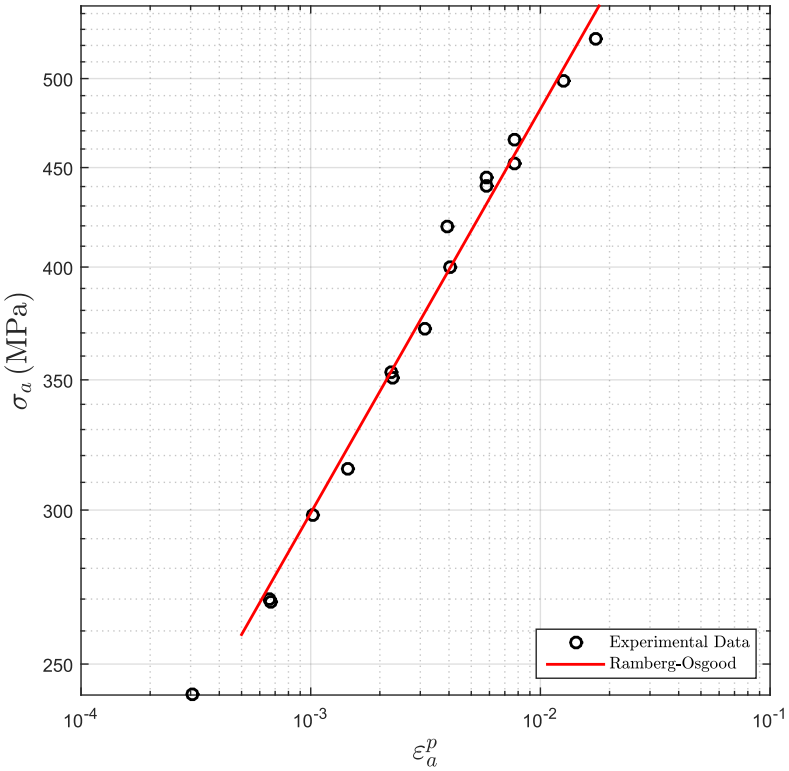

Figure 5.4 – Identification of the axial Ramberg-Osgood parameters K' and n'.

The previously mentioned curve is then considered to identify H^k and b^K according to Eq.(5.4), which furnishes and σ_{y0}=268.6 MPa, $H^K = 32355.0$ MPa, $b^K = 122.5$. Fig.5.5 displays graphically the calibration result.

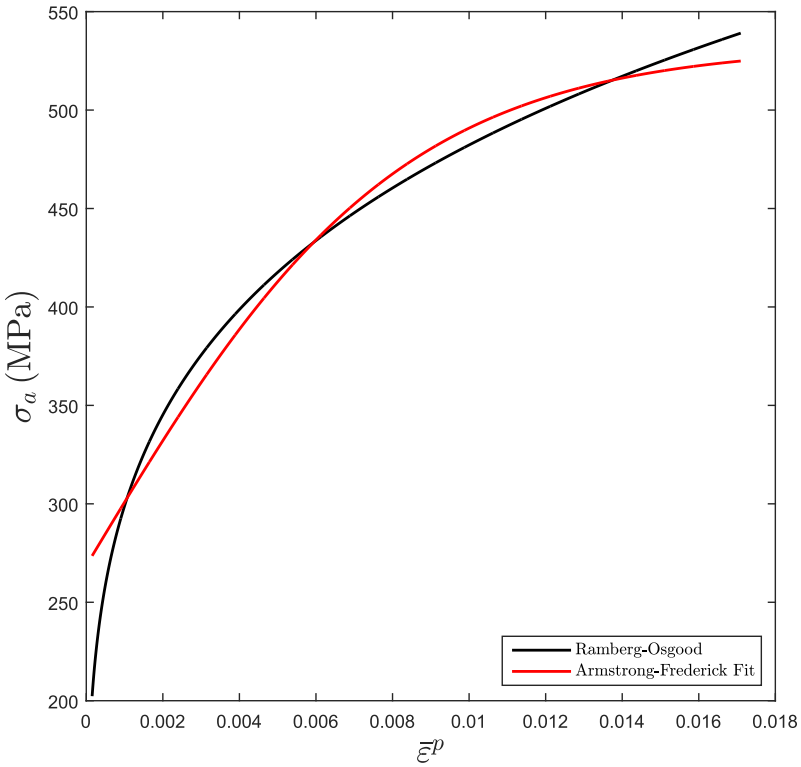

Figure 5.5 – Calibration of Armstrong-Frederick parameters based on the data in Table 5.3.

5.4.2 Calibration of Gao's b Parameter

The identification b followed the same idea used previously in monotonic conditions. In this regard, Table 5.4 contains the information required to compute b. First, Eq.(5.5) can be extended to shear conditions:

$$\tau_a = K_0' \left(\gamma_a^p\right)^{n_0'}, \tag{5.6}$$

where K_0',n_0' and γ_a^p respectevely express the cyclic shear hardening modulus, cyclic shear hardening exponent and plastic shear strain amplitude. Performing the same approach to calculate K' and n', one obtains K'=614.4 MPa and n'=0.22. Figure 5.6 shows the Ramberg-Osgood curve in shear conditions.

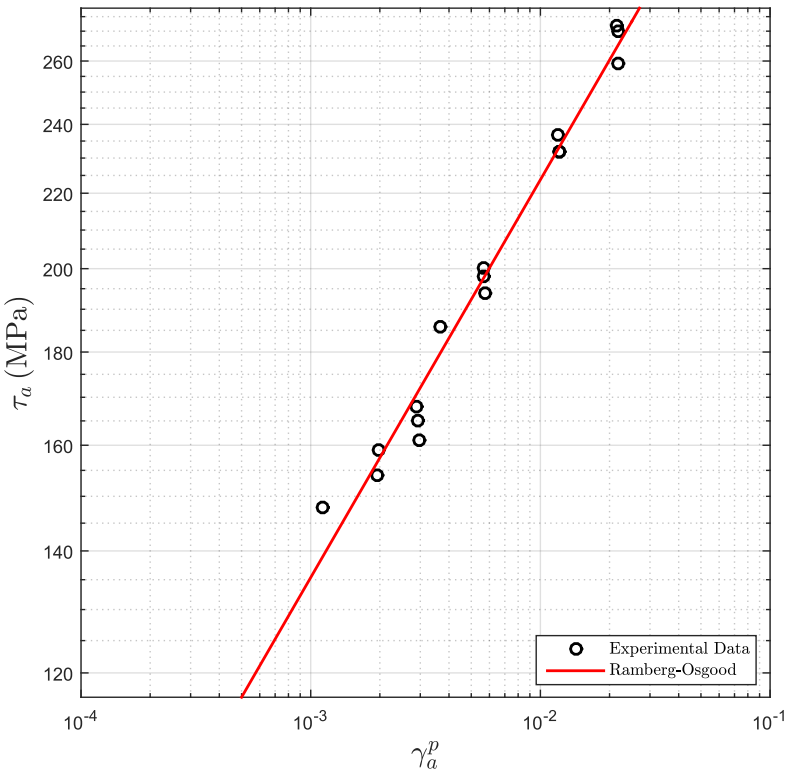

Figure 5.6 – Identification of the shear Ramberg-Osgood parameters K'_0 and n'_0.

If Mises behavior is assumed, one can convert shear amplitudes into von Mises equivalent measures and carry out the nonlinear regression of Eq.(5.4). The expressions used in this transformation are:

$$\begin{cases} \sigma_a = \sqrt{3}\tau_a, \\ \bar{\varepsilon}_a^p = \dfrac{\gamma_a^p}{\sqrt{3}}. \end{cases} \tag{5.7}$$

The analysis of the equivalent Ramberg-Osgood curve furnishes $\sigma_{y0} = 244.2$ MPa, $H^K = 30741.0$ MPa and $b^K = 137.4$. If the SAE 1045 steel behave as a von Mises material, σ_{y0} should be same (or at least extremely close) independently of the loading conditions considered. Since the values of σ_{y0} calculated with axial and torsion data are different, SAE 1045 steel has J_3 dependence. With this fact, one may estimate b by plotting the Mises yield surfaces calibrated in tension-compression and shear, and Gao's surface with different b values. The results obtained are discussed in more details in Chapter 7. Fig.5.7 displays the comparison of the kinematic hardening laws identified based on the data in Table 5.3 and 5.4.

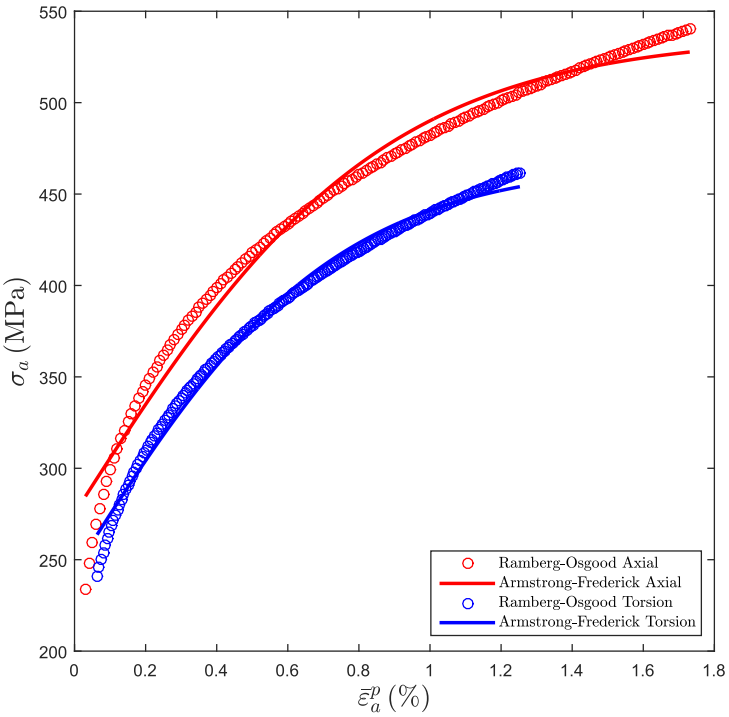

Figure 5.7 – Comparison between the kinematic hardening calibration results obtained by the analysis on the fully reversed axial and shear data.

Table 5.6 summarizes the parameters calibrated supported by the data of Leese and Socie (1989).

Table 5.6 – Material parameters calibrated for the SAE 1045 in LCF conditions based on the data from Leese and Socie (1989).

Parameter	Value
Elasticity Modulus E	202.0 GPa
Poisson's Ratio ν	0.3
Cyclic Yield Stress σ_{y0}	268.6 MPa
Kinematic Hardening Modulus H^K	32355.0 MPa
Saturation Coefficient b^K	122.5

It is worth noting that, as mentioned previously, the kinematic hardening constants in Tables 5.5 and 5.6 are not equal, not even approximately.

6 Monotonic and Ultra-Low Cycle Results

6.1 Gao's a and b Parameters

As described in Chapter 5, Gao's a and b constants are calibrated based on the monotonic tests on the butterfly specimens in the vertical and horizontal directions. Following the procedure detailed in Chapter 5, b is the first to be identified based on the horizontal tensile tests ("Butterfly +0°" in Table 5.1). Only isotropic hardening is considered in this case, and hence H^K and b^K are set as 0 in the mathematical and numerical models presented in Chapter 3 and 4 respectively. Furthermore, the hardening curve used in the the Finite Elements simulations is the defined by Eq.(3.22) with the optimized parameters in Table 5.5.

6.1.1 b Estimation

A simulation with $a = b = 0$ (recovering von Mises) is conducted to evaluate the influence of J_3 on the Ductile Fracture behavior of SAE 1045 steel. The result of this simulation enables to estimate a range of possible b values. Based on works in the literature (Gao et al., 2011; Cavalheiro and Malcher, 2017; Malcher et al., 2020) and on the predicted von Mises numerical response, one tests different b within the interval $[-100.0, -10.0]$. The lower bound of this range was chosen due convexity issues related with high negative b values (see Cavalheiro and Malcher (2017)).

The best trade-off relation (with respect to computational time and convergence) was achieved with $b = -60.0$. When higher (in absolute value) b were tested, convergence issues were observed, possibly related to convexity loss. This latter implies on non-positive dissipation δ in Eq.(3.30), which is reflected on the convergence problems of the numerical solution. On the left of Fig.6.1, the numerical reaction curves obtained with $a = b = 0$ and $a = 0$ (red star-dashed line), b = -60.0 (blue square-dashed line) are displayed and compared with the experimental data.

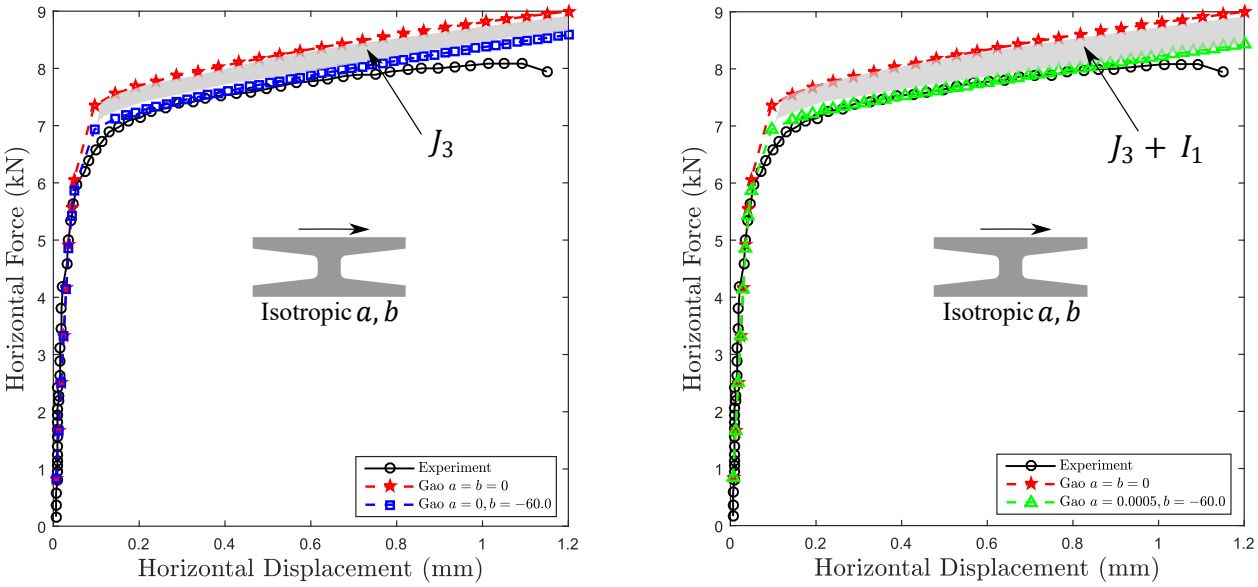

Figure 6.1 – Comparison between the numerical responses of Mises and Gao based formulations with the experimental reaction curve for the horizontal tension test (+0° loading direction). On the left, only b is activated, while on the left both a and b are considered.

It is noted from Fig.6.1 that the SAE 1045 steel is not a von Mises type material, since the J_2-formulation cannot describe its behavior in shear conditions. Therefore, this material Ductile Fracture response has J_3-dependence. Moreover, the blue square-dashed curve furnished by the simulation with $a = 0$ and b = -60.0 presents better agreement with the experimental reaction curve, which demonstrates that more accurate predictions are indeed achieved by considering J_3. The shaded region on the left portion of Fig.6.1 depicts the differences between von Mises and Gao's approaches due to the third invariant.

Interestingly, Fig.6.1 shows that the activation of b lowers the numerical reaction curve towards the experimental one. Actually, the higher b (limited by the model convexity), higher it is the downward movement produced.

6.1.2 a Estimation

With b =-60.0, a similar analysis is used to compute a by the experimental reaction curve from the vertical tensile test ("Butterfly +90°" in Table 5.1).

Thus, the Mises numerical response ($a = b = 0$) is registered to analyze whether or not I_1 influences the material behavior. The red star-dashed lines in Fig. 6.2 represents the referred numerical reaction curve.

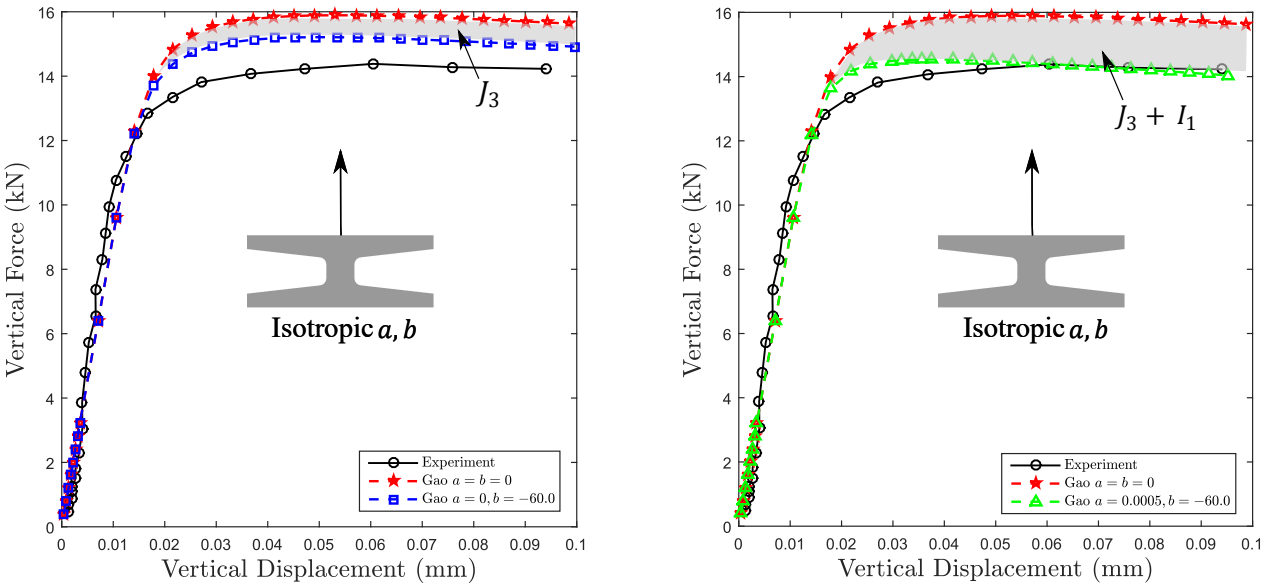

Figure 6.2 – Comparison between the numerical responses of Mises and Gao based formulations with the experimental reaction curve for the vertical tension test (+90° loading direction). On the left, only b is activated, while on the left both a and b are considered.

From Fig.6.2, it is observed that von Mises approach does not correctly predict the experimental behavior. One may wonder why the simulation with $a = b = 0$ and with the optimized parameters in Eq.(5.3) does not accurately describe the tension test in the +90° direction, if this test was supposed to be close to the uniaxial tensile conditions found in smooth cylindrical specimen. This apparent contraction can be explained by the butterfly specimen geometry. The (initial) uniaxial stress state on the smooth specimen is characterized by $\eta = 1/3$ and $\xi = 1$. If notches are made in cylindrical specimens, the triaxiality ratio increases with the reduction of the notch radius, and consequently, the effect of I_1 is enhanced (Gao et al., 2011; Bao and Wierzbicki, 2004; Bai, 2008; Driemeier et al., 2010; Malcher et al., 2020). The curvature in the gauge section of the butterfly specimen (see Bai (2008) and Fig.5.1) works as a notch, and hence the "Butterfly +90°" experiment has $\eta > 1/3$ and $\xi \neq 1$, which is different from the calibration point ($\eta = 1/3$ and $\xi = 1$).

Next, one performs a second simulation with $a = 0$ and $b = -60.0$ to evaluate the contribution from J_3 to the difference between the experimental and the red star-dashed curves. The result is displayed on the left plot of Fig.6.2. One can observe that some degree of correction is achieved, although less pronounced than in the similar simulation in Fig.6.1. This indicates that J_3 is not the most influential parameter in this loading condition, and further suggests that a need to be considered.

In this regard, one calibrates a with an analogous strategy as utilized for estimating b. Several simulations were conducted with different a values and keeping b = -60.0 fixed. The search interval was defined as $[0.0001, 1.0]$, also based on works in the literature. The best result was reached with $a = 0.0005$, and the numerical reaction curve (green

triangle-dashed line) is shown on the right graph in Fig.6.2. The correction obtained by the incorporation of I_1 is substantial and demonstrates the strong influence of this parameter in tensile (or compressive) conditions. The shaded region on the right plot in Fig.6.2 highlights the difference between von Mises and Gao's reaction curves due to J_3 and I_1.

With the identified a and b, a second simulation of the monotonic shear test with these two parameters is carried out to investigate the effect of I_1 in shear scenarios. The response computed is represented by the green triangle-dashed curve in the right portion in Fig.6.1. One notices that the usage of $a = 0.0005$ in this second simulation leads to a negligible effect, which corroborates to the empirical observation that the hydrostatic stress has a minor influence on material behavior in shear-predominant loads (Bai, 2008; Driemeier et al., 2010; Malcher et al., 2020; Morales, 2020).

At this point, some remarks based on the results so far can be made:

- In shear-predominant situations, J_3 displays a more pronounced influence of the Ductile Fracture Behavior of SAE 1045 steel;
- In tensile conditions, I_1 has a stronger effect on the SAE 1045 steel mechanical behavior.

6.1.3 Verification of The Mesh Used to Discretize the Butterfly Specimen

One simulated the monotonic shear test with a more refined mesh then the one presented in Fig.4.1 to prove that, for purposes of this work, the coarse mesh in Fig.4.1 is suitable. The refined mesh is formed my 1440 20-noded quadratic hexahedral elements totalizing 7773 nodes, with smaller elements in the central region of the butterfly specimen. More details of the refined mesh can be found in the work of Cavalheiro and Malcher (2017). It is worth mentioning that the parameters used in this simulation are the same as utilized to produce the red star-dashed reaction curves in Fig.6.1 and 6.2. Figure 6.3

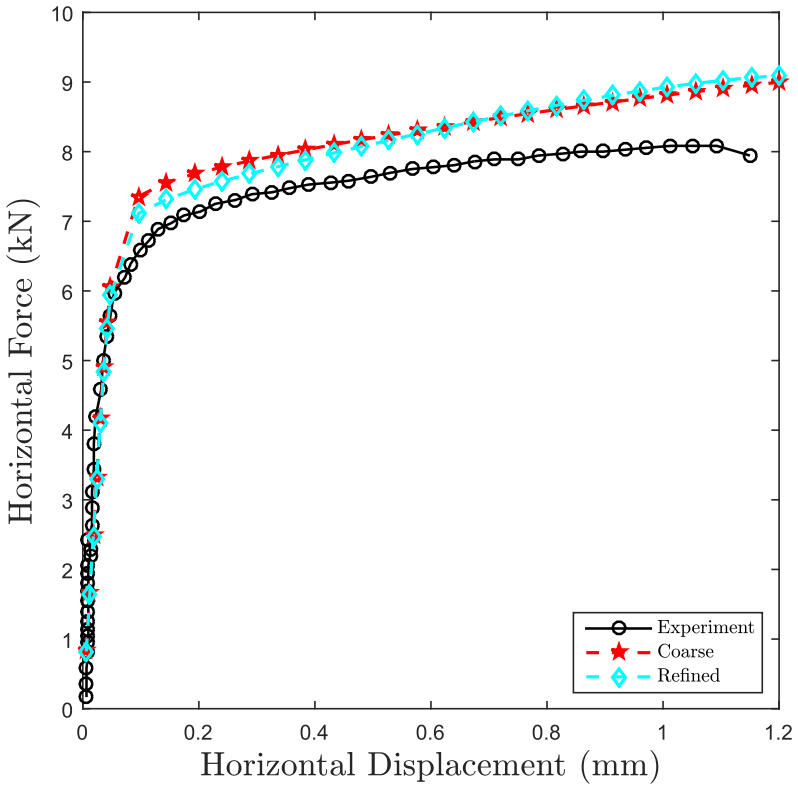

Figure 6.3 – Comparison between the numerical responses produced by FEM simulations using the mesh in Fig.4.1 (red star-dashed curve) and a more refined one(cyan diamond-dashed curve).

It is observed from Fig.6.3 that the numerical reaction curves are extremely similar, which confirms the suitability of the mesh shown in Fig.4.1. Furthermore, Fig.6.3 corroborate the lack of accuracy of traditional J_2-modeling for SAE 1045 steel. Finally, one acknowledges that refined meshes must be used to properly capture local phenomenons, such as crack initiation spot and damage, which are not the aim of this dissertation.

6.2 Combined Tension and Shear

With the model parameters fully identified, one analyzes the model performance with other loading conditions rather the calibration points utilized to determine a and b. In this setting, the monotonic tests on the $+30°$ and $+5°$ directions (see Fig.5.1) were simulated. These experiments are particularly interesting because they are mix between pure tension and pure shear situations, and thus have features from both. It is important to notice that the closer to the $0°$ orientation, the close to shear the test is. Once more, only isotropic hardening is considered.

6.2.1 +30° Monotonic Tension

Three simulations of the +30° monotonic tension experiment were conducted: first with $a = b = 0$ (red star-dashed line), second with $a = 0$ and $b = -60.0$ (blue square-dashed line), and finally with $a = 0.0005$ and b=-60.0 (green triangle-dashed line). Figure 6.4 shows the results for each simulation.

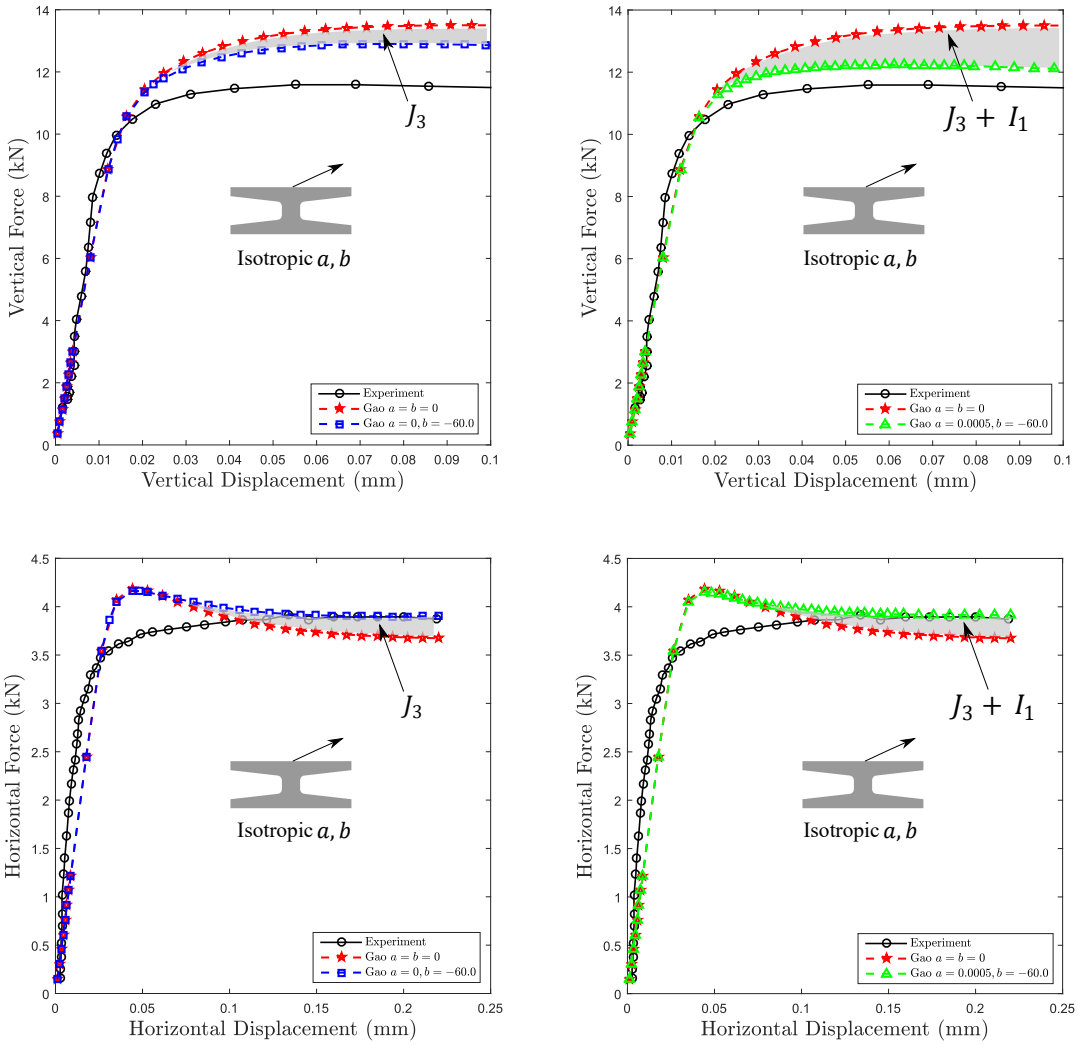

Figure 6.4 – Comparison between the numerical responses of Mises and Gao based formulations with the experimental reaction curve for the vertical tension test (+30° loading direction). On the top row, the vertical reaction curves, and on the bottom, the horizontal ones.

From the first row of images in Fig.6.4, one observers that the best description of the vertical F versus d curve is achieved by incorporating both I_1 and J_3. Furthermore, the top left plot suggests that J_3 has a less strong influence on the SAE 1045 steel behavior under +30° load than I_1. This was expected, as this test is closer to the +90° experiment, which is basically a monotonic load in the vertical direction. The bottom row further corroborates this remark, since the incorporation of J_3 does not produce a significant change in the horizontal reaction curve, and when associated with I_1, it remains unchanged.

6.2.2 +5° Monotonic Tension

The same three simulation conditions mentioned previously were used out to simulate the +5° monotonic tension experiment. Figure 6.5 displays the results obtained. The color identification for +30° is the same for +5°.

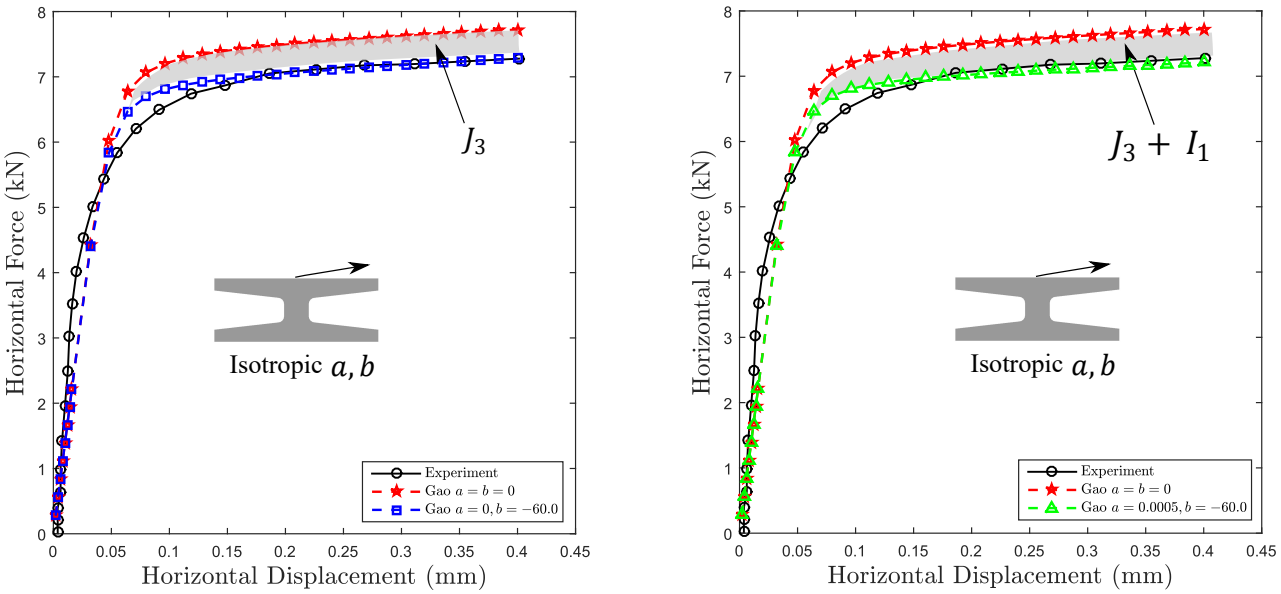

Figure 6.5 – Comparison between the numerical responses of Mises and Gao based formulations with the experimental reaction curve for the vertical tension test (+5° loading direction). On the top row, the vertical reaction curves, and on the bottom, the horizontal ones.

Differently from what was observed in Fig.6.4, J_3 is the most influential invariant for the +5° loading direction. Moreover, the hydrostatic stress has a negligible effect, which was feature shared with the monotonic shear case in Fig.6.1. This result was also foreseen since the +5° tension is closer to the +0° orientation and hence shear predominant.

Overall, both Fig.6.4 and 6.5 demonstrate the Mises-based modeling fails to describe the SAE 1045 steel Ductile Fracture behavior, which further corroborates the J_3 and I_1 dependence of this material.

6.3 Ultra-Low Cycle Results with a and b from the Monotonic Data

The Ultra-Low Cycles tests contained in Table 5.2 were simulated using the a and b values calibrated with the monotonic data. Thus, it is assumed at first that a and b obtained by considering isotropic hardening are suitable for Ultra-Low conditions. On the other hand, mixed hardening is considered due to the presence of load reversals, which requires kinematic hardening. The material parameters used in the simulations are contained in Table 5.5. It is worth pointing that the initial yield stress is taken as the monotonically calculated one for Ultra-Low simulations. This choice was made based on

the fact that only 1 load reversal is applied, and hence it is assumed that there is not enough time to cyclic (e.g. cyclic softening) effects to take place and modify σ_{y0}.

6.3.1 Compression-Tension $(-90° \text{ to } +90°)$ Results

Figures 6.6 and 6.7 display the numeric reaction curves obtained from the Finite Element simulations of the compression-tension tests $(-90° \text{to} +90°)$.

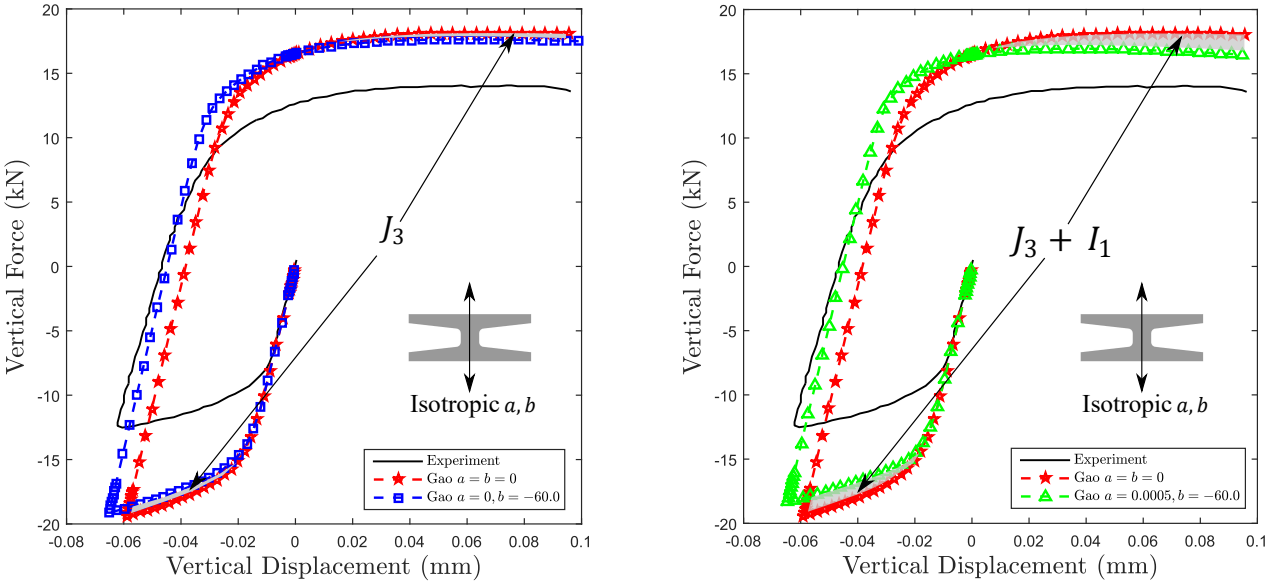

Figure 6.6 – Comparison between the numerical responses of Mises and Gao based formulations with the experimental reaction curve from the compression-tension $(-90° \text{ to } +90°)$ test 1. On the left, only b is activated, while on the left both a and b are considered. Gao's parameters a and b calibrated on monotonic conditions.

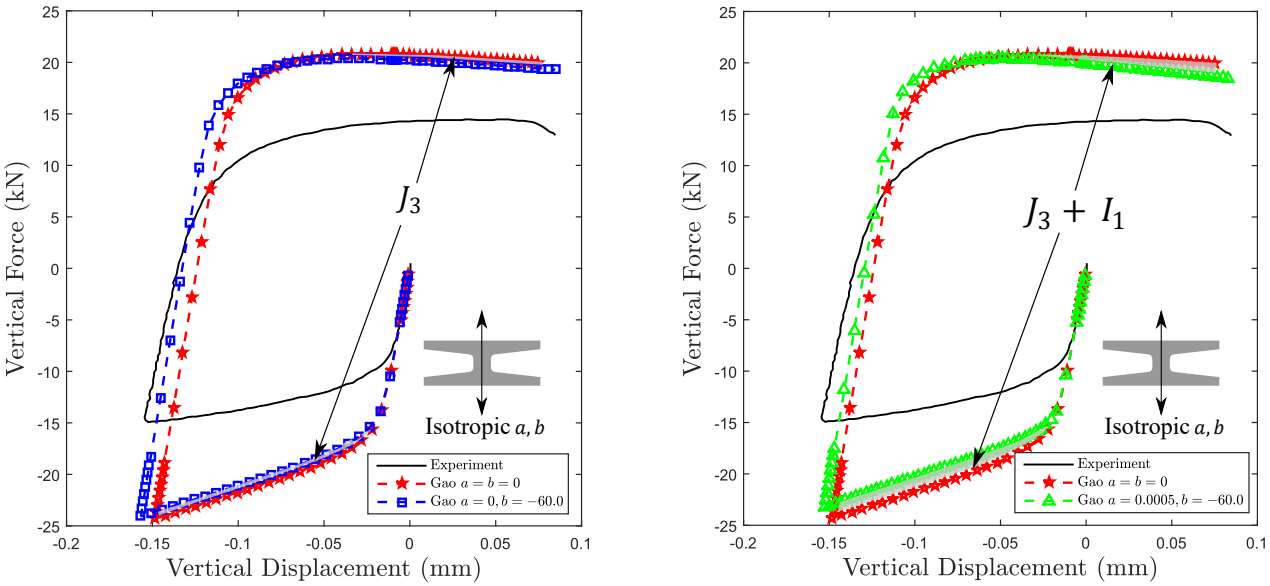

Figure 6.7 – Comparison between the numerical responses of Mises and Gao based formulations with the experimental reaction curve from the compression-tension test ($-90°$ to $+90°$) 2. On the left, only b is activated, while on the left both a and b are considered. Gao's parameters a and b calibrated on monotonic conditions.

As observed in Fig.6.2, in either cases the first invariant is the key factor controlling SAE 1045 ULCF behavior in compression-tension. This latter confirms the remarks pointed out previously in Fig.6.2. Nevertheless, the Gao's based simulations were not satisfactorily close the experimental F versus d data, as in the monotonic case. This suggests that perhaps a recalibration of a and b for ULCF applications is required. The shaded regions on the left plots of Fig.6.6 and 6.7 represent the effect of J_3, while on the left express the effect of both I_1 and J_3.

6.3.2 Shear-Shear ($-0°$ to $+0°$) Results

Figures 6.8 and 6.9 display the numeric reaction curves obtained from the Finite Element simulations of the shear-shear tests (-0°to $+0°$).

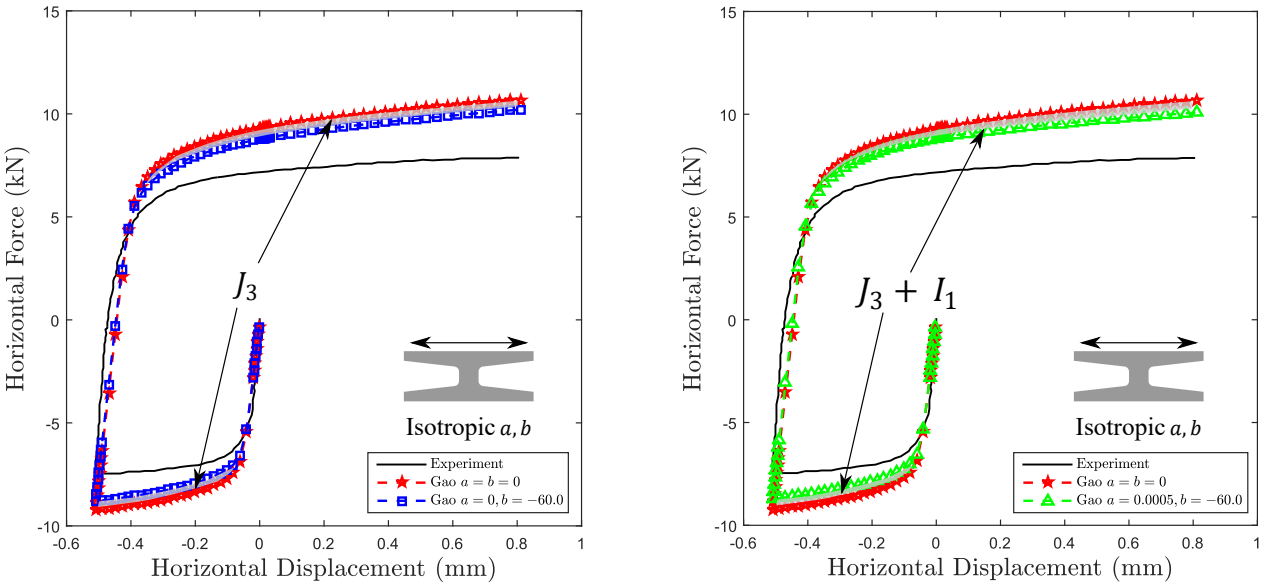

Figure 6.8 – Comparison between the numerical responses of Mises and Gao based formulations with the experimental reaction curve from the shear-shear ($-0°$ to $+0°$) test 1. On the left, only b is activated, while on the left both a and b are considered. Gao's parameters a and b calibrated on monotonic conditions.

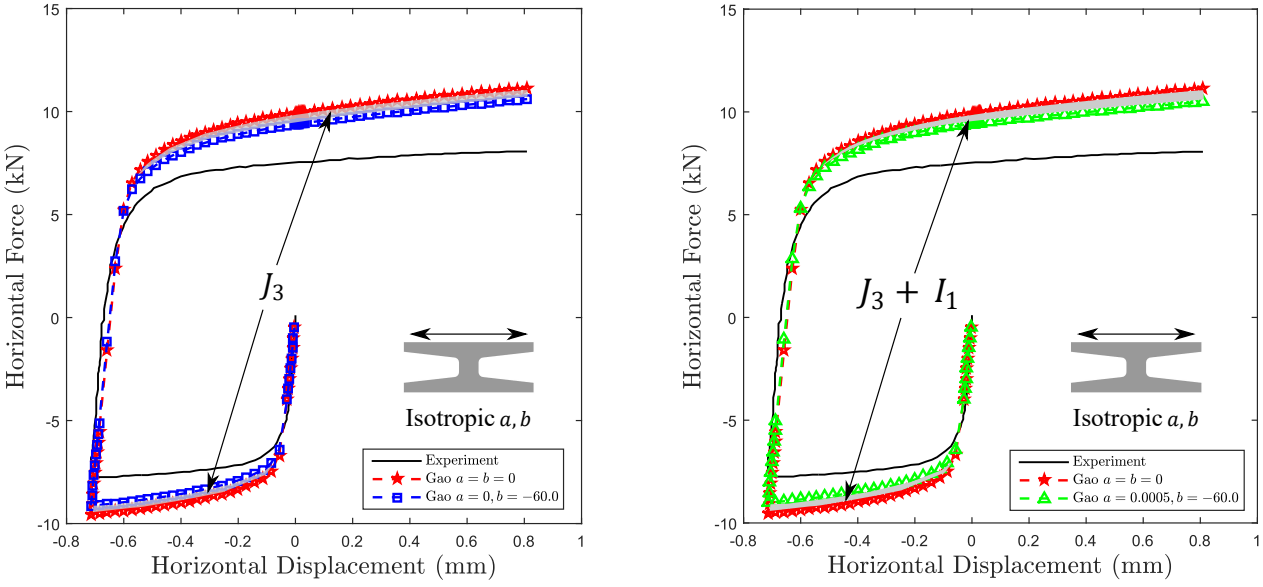

Figure 6.9 – Comparison between the numerical responses of Mises and Gao based formulations with the experimental reaction curve from the shear-shear ($-0°$ to $+0°$) test 2. On the left, only b is activated, while on the left both a and b are considered. Gao's parameters a and b calibrated on monotonic conditions.

Once more, one notices that the simulation response is more influenced by J_3 and indifferent to I_1 for the reversed shear case. However, as observed in Fig.6.6 and 6.7, a and b calibrated with the monotonic data is not adequate for ULCF conditions. This gives more support to the need to recalibrate these parameters. The shaded regions on the left plots of Fig.6.8 and 6.9 represent the effect of J_3, while on the left express the effect of both I_1 and J_3.

6.4 Ultra-Low Cycle Results After Recalibrating a and b in ULCF conditions

The outcomes of the simulations presented in Fig.6.6, 6.7, 6.8 and 6.9 indicate that a recalibration of Gao's constants is needed. This is likely due to the presence of kinematic hardening in the ULCF modeling, which is neglected on the monotonic case.

In this regard, one conducts an identification methodology following the same steps utilized in monotonic conditions. First, based on the reversed shear tests, several simulations are performed with different b values within the range $[-70.0, -10.0]$. The interval was narrowed compared to the one chosen previously because of the convexity loss observed with a high negative b. The best result was achieved with b=-70.0. The left plots in Fig.6.10 and 6.11 shows the numerical F versus d curves for $a = 0$ and $b = -70.0$ (blue square-dashed lines).

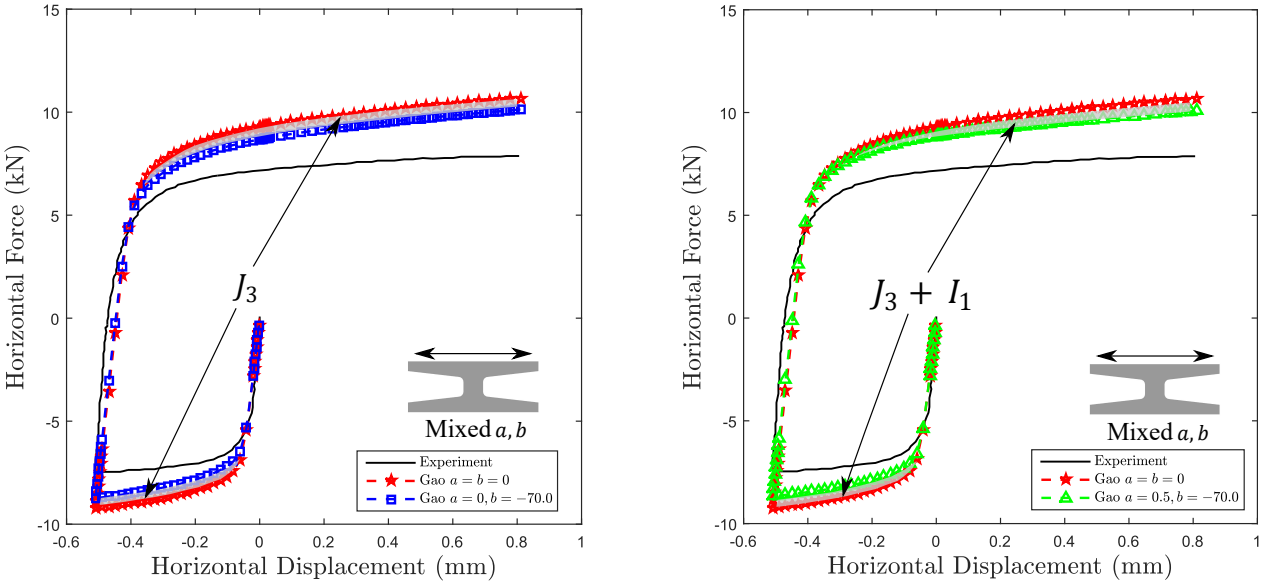

Figure 6.10 – Comparison between the numerical responses of Mises and Gao based formulations with the experimental reaction curve from the shear-shear ($-0°$ to $+0°$) test 1 after recalibration. On the left, only b is activated, while on the left both a and b are considered.

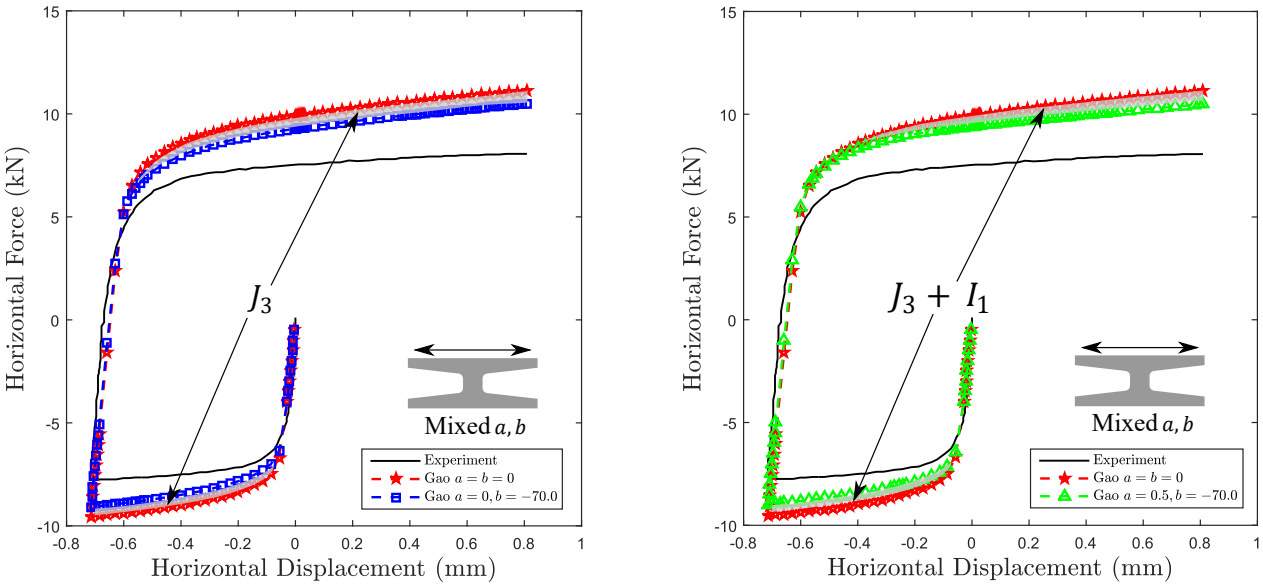

Figure 6.11 – Comparison between the numerical responses of Mises and Gao based formulations with the experimental reaction curve from the shear-shear ($-0°$ to $+0°$) test 2 after recalibration. On the left, only b is activated, while on the left both a and b are considered.

Comparing Fig.6.10 and 6.11 to 6.8 and 6.9, there was a slight improvement in the model's mechanical response prediction. Approximating the blue square-dashed line to the experimental curve would require to lower b values, but as one is limited by the model convexity, b=-70.0 was the lowest value possible.

The compression-tension experiments were simulated with $a = 0$ and $b = -70.0$, and as observed previously, J_3 has a minor influence in this conditions, which indicates that ,once more, I_1 is the factor controlling the mechanical response in vertical loading situations. The left portion Fig.6.12 and 6.13 show the numeric F versus d from the referred simulations.

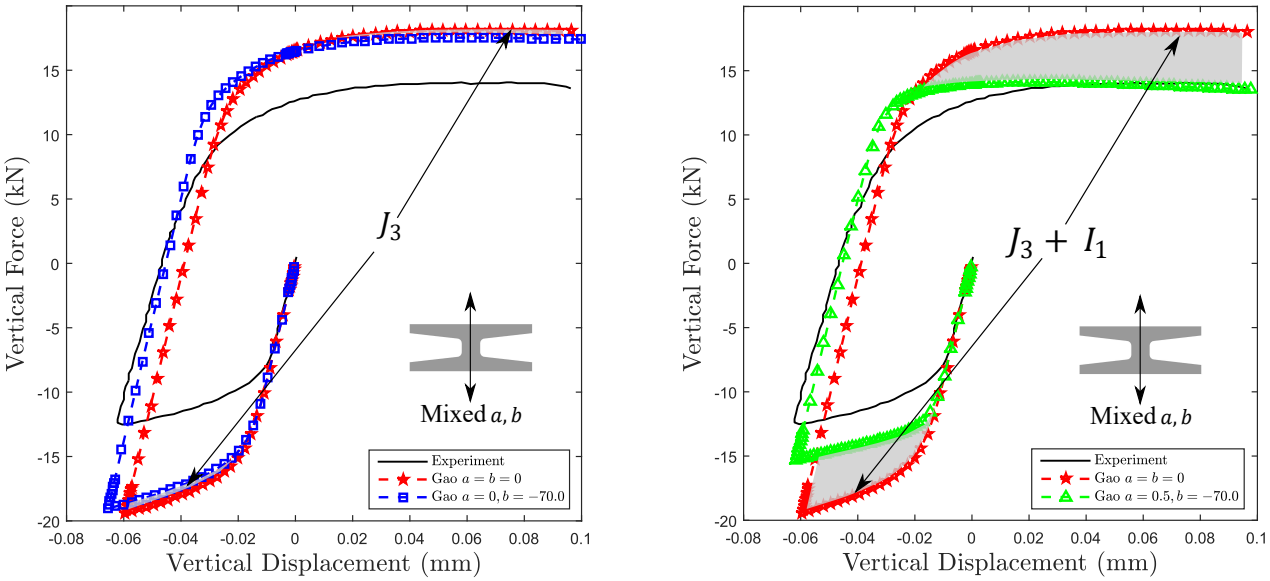

Figure 6.12 – Comparison between the numerical responses of Mises and Gao based formulations with the experimental reaction curve from the compression-tension ($-90°$ to $+90°$) test 1 after recalibration. On the left, only b is activated, while on the left both a and b are considered.

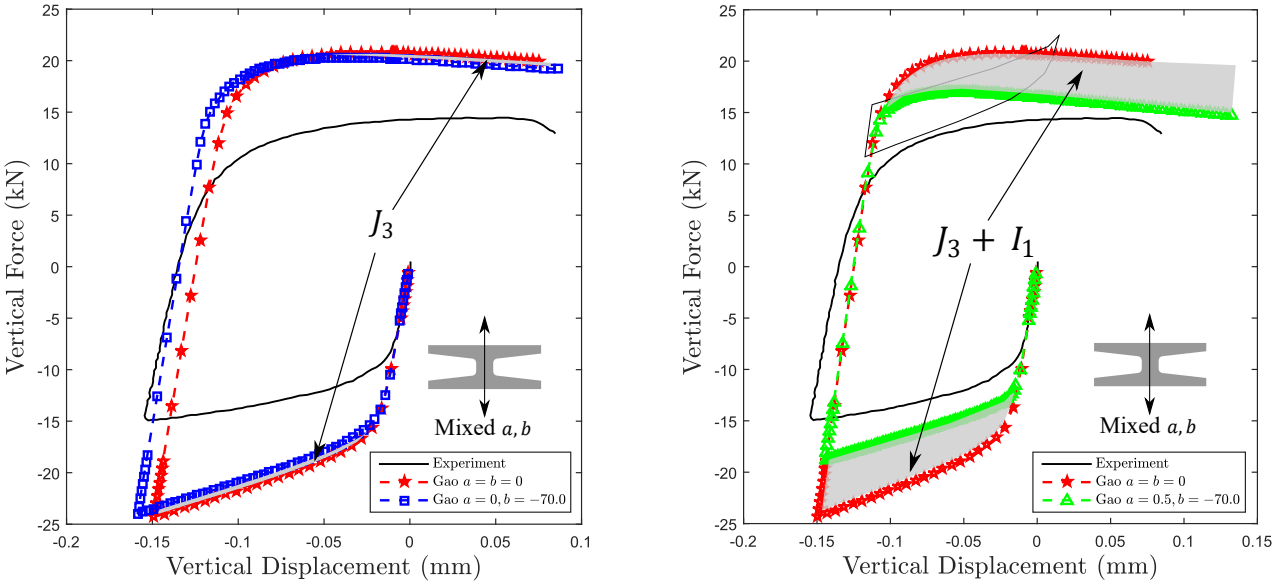

Figure 6.13 – Comparison between the numerical responses of Mises and Gao based formulations with the experimental reaction curve from the compression-tension ($-90°$ to $+90°$) test 2 after recalibration. On the left, only b is activated, while on the left both a and b are considered.

Therefore, the identification of a was carried out with the same steps used previously in monotonic conditions. The same search interval was used, and after many tests, the best agreement was reached with $a = 0.5$. The right plots on Fig.6.12 and 6.13 display graphically the results from the Finite Element simulations with $a = 0.5$ and $b = -70.0$. As highlighted by the shaded in regions in the latter graphs, I_1 provokes a notable correction in the green triangle-dashed reaction curves, further confirming the strong influence of this parameter in this loading scenario.

With the recalibrated a and b, the reversed shear tests are simulated once again. The outcome of such simulations are shown on the right plots in Fig.6.10 and 6.11. As noticed in Fig.6.1, 6.8 and 6.9, I_1 has negligible effect on reversed shear tests (shear-predominant cases).

Overall, Fig.6.6, 6.7, 6.10, 6.9, 6.10, 6.11, 6.12 and 6.13 demonstrate that in all cases, the von-Mises formulation fails to predict the SAE 1045 steel behavior in Ultra-Low Cycle conditions. This latter gives more proof that this alloy is I_1 and J_3 dependent.

6.5 Summary

The results discussed in this chapter lead to following remarks:

- SAE 1045 steel Ductile Fracture and Ultra-Low Cycle behaviors display pressure and third invariant dependence. Thus, one who wishes to predict the failure upon these phenomenons of structures made of this material need to consider I_1 and J_3;
- In shear predominant conditions, the first invariant can be neglected without loss of accuracy. Conversely, J_3 produces less pronounced corrections than I_1 on the numerical reaction curves in tensile situations;
- Gao's a and b parameters depend on the particular phenomenon considered, as demonstrated by the calibrated values in monotonic (isotropic hardening) and ULCF (mixed hardening) conditions.

7 Low Cycle Fatigue Results

7.1 Gao's a and b Parameters

One of conclusions of Chapter 6 asserted that, depending on the phenomenon studied, a and b may have different values. More precisely, a and b apparently are function of the hardening type considered. Thus, one expects that a and b will likely display different values in Low Cycle Fatigue conditions than the calibrated a and b in Chapter 6, since the LCF simulations were carried out considering kinematic hardening only.

7.1.1 b Estimation

The fully reversed torsion tests in Table 5.4 and the calibration of kinematic hardening parameters σ_{y0}, H^K and b^K displayed graphically in Fig.5.7 enable the estimation of b. The technique used for this purpose is different from the methodology in Chapter 6.

The calibration strategy here is based on plotting on the principal stress space the Mises's yield surface calibrated with fully reversed tension and shear experiments, and Gao's for a given b. Since fully reversed tension and torsion loads are plane stress situations, one may plot the yield surfaces on the $\frac{\sigma_1}{\sigma_{y0}}$ versus $\frac{\sigma_2}{\sigma_{y0}}$ plane, where σ_1 and σ_2 are the on-plane principal stresses. The b value that provides the Gao's surface closest to Mises's calibrated in torsion in the pure shear axis ($\sigma_2 = -\sigma_1$), is the calibrated b. It worth noting that a does not affect this calibration method, because the stress state in pure shear case is deviatoric.

In this regard, one uses the same search range set for the ULCF case, and interestingly, b=-70.0 furnished the best agreement with Mises's shear yield surface, which is the same value estimated for ULCF. Figure 7.1 shows Mises's, Tresca's and Gao's surface on the previously referred plane.

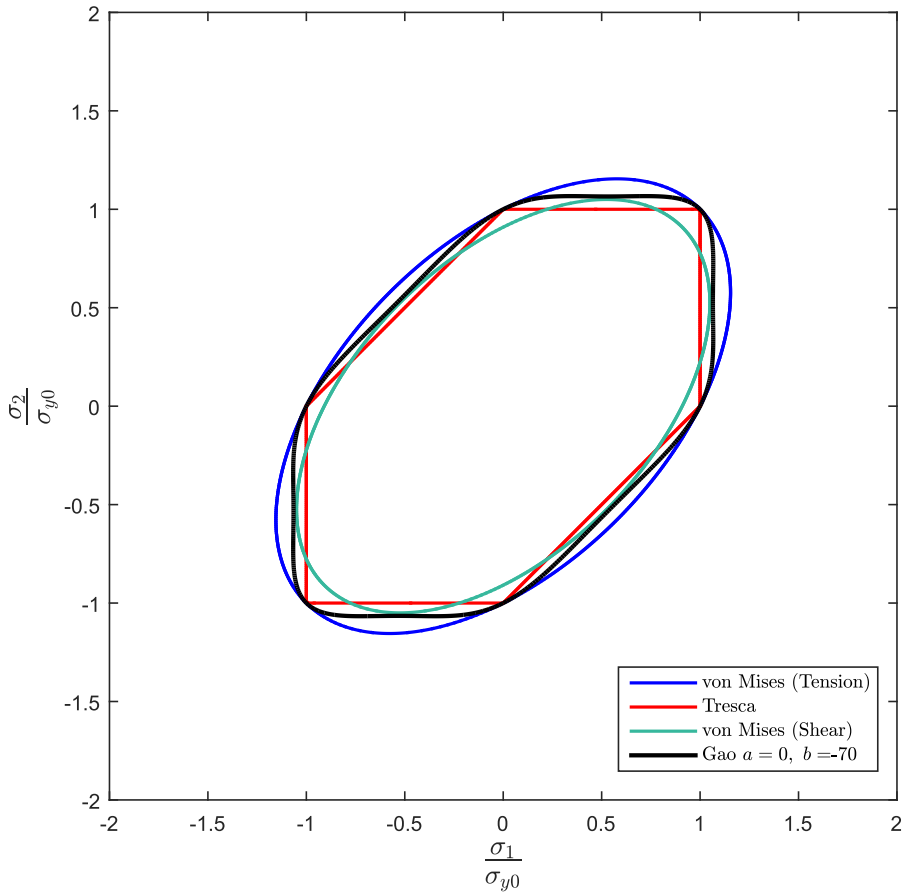

Figure 7.1 – Yield surfaces of each yield criterion on the normalized principal stress space for plane stress conditions. In blue, Mises's surface obtained in axial conditions; in Black Gao's for b =-70.0, in green; Mises's identified in shear; and in red, Tresca's surface.

One notices some important remarks present in Fig.7.1. Firstly, as discussed in Chapter 2, Mises's (blue-solid line), Tresca's, and Gao's yield surfaces coincide in uniaxial stress states. Secondly, Gao's surface (black-solid line) with $b = -70.0$ indeed touches the shear Mises's one in the pure shear line ($\sigma_2 = -\sigma_1$ axis). Thirdly, SAE 1045 steel displays an elastoplastic behavior within Tresca's Mises's yield surfaces, another observation for many metallic materials stated in Chapter 2. Finally, SAE 1045 steel Low Cycle Fatigue behavior has J_3 dependence.

7.1.2 a Estimation

The estimation of a requires a data set in which I_1 has a major influence, such as LCF in cylindrical notched specimens ($\eta > 1/3$ and $\xi = 1$). Nevertheless, the simulations carried out in LCF conditions, being performed at the Gauss point level, do not allow the incorporation of stress states with $\eta > 1/3$. Therefore, one assumes $a = 0$.

7.2 Fully Reversed Axial Loading

With the material parameters in Table 5.6 and the estimated a and b for LCF conditions, one conducts a series of Gauss point simulations (20 load cycles) with the axial strain amplitudes ε_a in Table 5.3. Therefore, the isotropic hardening constants are set to 0 in the numerical state update model depicted in Chapter 4. Figure 7.2 presents the hysteresis loops predicted by von Mises's (red circles) and Gao's (blue solid line) based formulations with Armstrong-Frederick kinematic hardening law.

The axial loops produced by the model presented in this work coincide with the J_2 responses, which confirms the first observation made in the previous section. This was foreseen result, as fully reversed axial loading is a uniaxial stress state ($\eta = 1/3$ and $\xi = 1$). The plots in Fig.7.2 are also evidence of the validation of the state update algorithm implemented.

The inputs of many fatigue life estimation methods (e.g critical plane) are the stress and strain histories, since they are needed to compute the stress and strain amplitudes in a given material plane. In this context, Fig.7.3 displays a comparison between the amplitudes predicted by each formulation and the average experimental normal stress $\bar{\sigma}_a$ in Table 5.3.

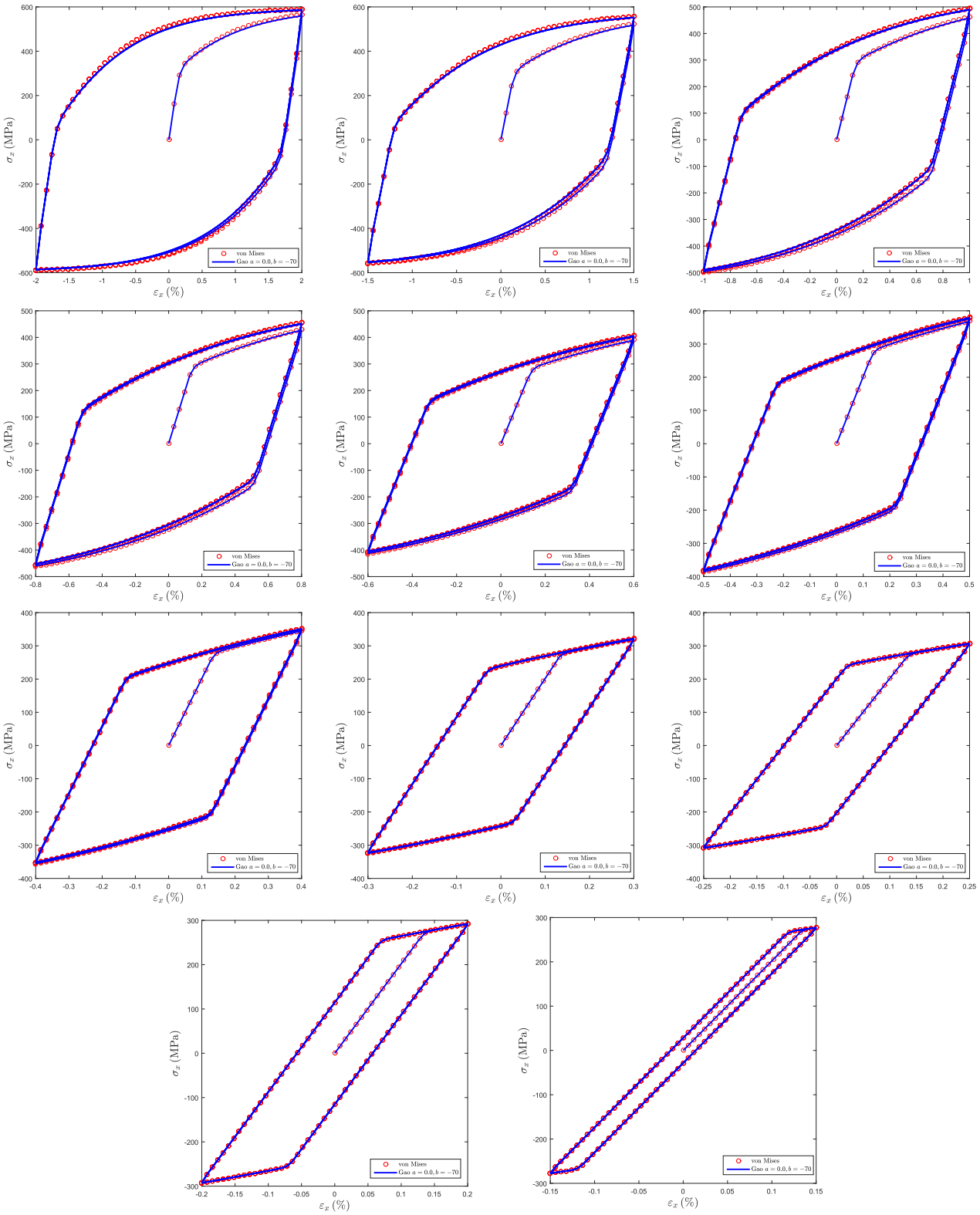

Figure 7.2 – Axial hysteresis loops predicted by von Mises's (red circles) and Gao's (blue solid line) formulations for a range of ε_a.

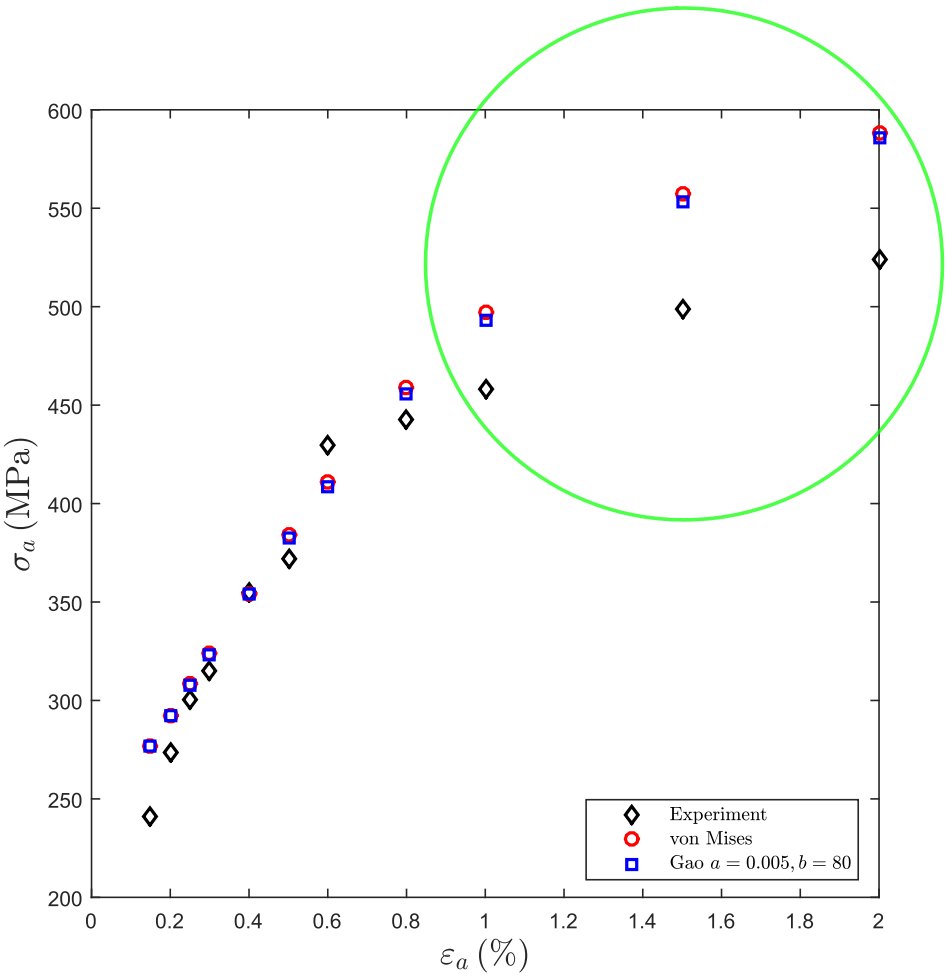

Figure 7.3 – Comparison between normal stress amplitudes σ_a predicted by Mises's(red circles) and Gao's (blues squares), and the mean experimental amplitudes (black diamonds) in Table5.3.

From Fig.7.3, one observes that the normal stress amplitudes predicted by Mises's and Gao's approaches are nearly identical, which confirms once again the first remark in the previous section. Furthermore, there is a fairly agreement with respect to data for low ε_a, and some considerable deviation for the three highest normal strain amplitudes, as highlighted by the big green circle in Fig.7.3. The extrapolation of the calibrated kinematical hardening law for these ε_a is a possible explanation for that.

7.3 Fully Reversed Torsion Loading

The same simulations conducted for the axial case were carried out for torsion loads, utilizing the shear strain amplitudes contained in Table 5.4. Figure 7.4 displays the shear hysteresis loops produced.

One notices from Fig.7.4 that, in all cases, von Mises's formulation exhibited higher shear stress levels, differently from the results of Fig.7.2. Similarly to what was pointed in Chapter 6 for the monotonic case, the activation of b tends to uniformly contracts the

hysteresis loops. Despite the disparities displayed by the numeric responses from the two constitutive models, they were less pronounced than in monotonic and Ultra-Low Cycle conditions.

Traditional fatigue life assessments depend on the calculation of the shear stress amplitude τ_a. In this dissertation, τ_a is simply defined as:

$$\tau_a = \frac{1}{2}\left[\max_t \tau\left(t\right) - \min_t \tau\left(t\right)\right]. \tag{7.1}$$

It is worth stating that other definitions of τ_a are possible (see Mamiya et al. (2009)). Based on Eq.(7.1), one computes τ_a for each simulation and compares to the mean experimental shear stress amplitudes $\bar{\tau}_a$ in Table 5.4. Figure 7.5 graphically displays this comparison.

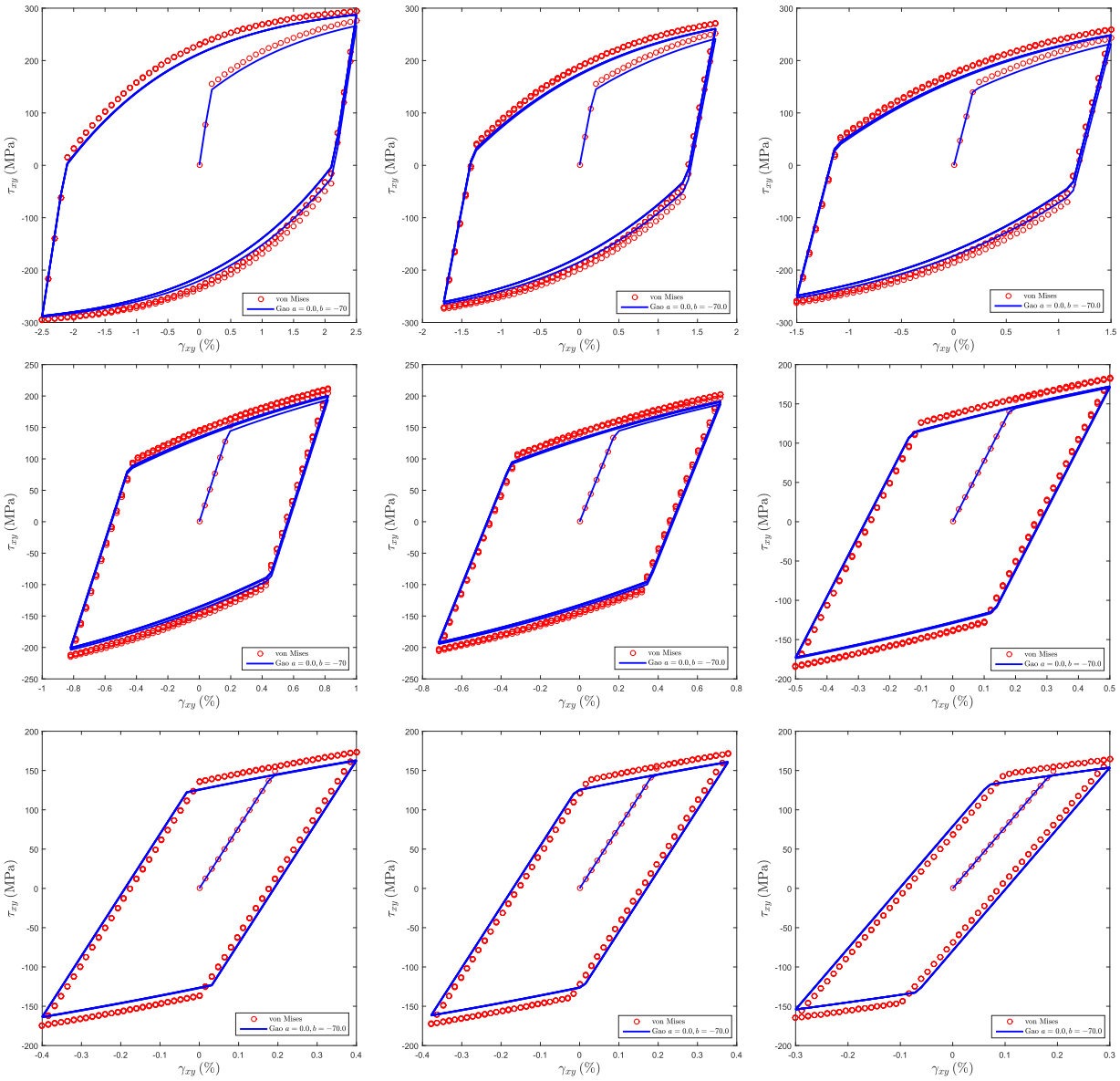

Figure 7.4 – Shear hysteresis loops predicted by von Mises's (red circles) and Gao's (blue solid line) formulations for a range of γ_a.

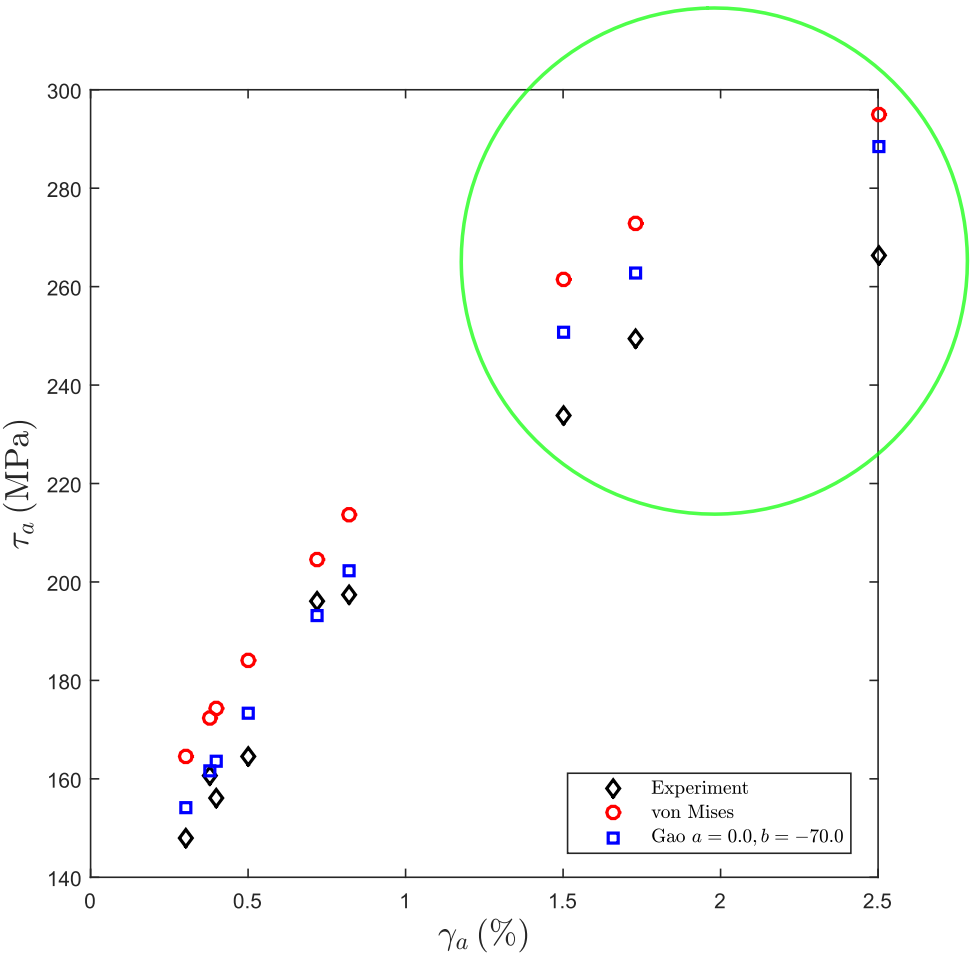

Figure 7.5 – Comparison between normal stress amplitudes τ_a predicted by Mises's(red circles) and Gao's (blues squares), and the mean experimental amplitudes (black diamonds) in Table5.4.

The shear stress amplitude computed ia Gao's modeling were always closer to $\bar{\tau_a}$. In particular, τ_a from the constitutive formulation of the present work satisfactorily agreed with experimental data for low γ_a. Nevertheless, the same problem in high ε_a noted in Fig.7.3 is also present in Fig.7.5. The same reasons given in the axial case are applicable for the inaccuracies depicted by the big green circle in Fig.7.5.

Therefore, the results in Fig.7.5 suggest that Gao's based approach can be utilized for more accurate fatigue predictions (at least in pure torsion) than traditional J_2 constitutive models.

7.4 Fatigue Life Assessment: A Qualitative Analysis

Supported by the cyclic plasticity outcomes of this Chapter, one may state some qualitative remarks on the crack initiation fatigue life assessment by the proposed constitutive model in this dissertation. Traditional life estimation techniques, such as critical plane and stress-invariants methods, rely on the accurate description of the σ_a and τ_a, along

with a proper calibration methodology. For example, the Smith-Watson-Topper (SWT) (Smith et al., 1970) criterion is expressed by:

$$F_{SWT} = \varepsilon_a \sigma_n^{max} = g\left(N_f\right), \tag{7.2}$$

where F_{SWT} and $g\left(N_f\right)$ respectively denotes the SWT parameter and a function of the the fatigue life N_f. Before computing F_{SWT}, one needs to perform a material plane search to identify which planes display the maximum normal strain amplitude ε_a. From these identified set, the material plane (or planes) with the highest maximum normal stress σ_n^{max} is selected to compute the product $\varepsilon_a \sigma_n^{max}$. The normal and shear stresses histories affect the calculation of σ_n^{max}, and hence accurate predictions of σ_a and τ_a lead to better life estimations. This feature is shared by all critical plane methodologies.

Since σ_a from Mises's and Gao's based models are basically the same, critical plane methods will predict the same life N_f for fully reversed uniaxial loads on SAE 1045 steel. Nevertheless, for torsion and more complicated loading conditions, distinct N_F will be estimated depending on the constitutive formulation utilized. Based on Fif.7.5, more accurate life estimations will likely be achieved by the usage of J_3-sensitive approaches (such as Gao's with mixed hardening presented in Chapter 3). However, the τ_a differences between the constitutive models are not dramatic to lead to substantial changes on critical plane N_f predictions. These life assessment techniques are not strongly influenced by the loop shape and size (Jiang et al., 2009), and hence the modeling choice will not greatly interfere if critical plane methods are used for durability estimations.

On the other hand, incremental approaches have gained substantial interest in recent years (see Chapter 2), because they capture effects that traditional methodologies are not capable of (Jiang et al., 2009), such as loop's size and shape. Besides, incremental techniques such as Damage Mechanics often consider a damage constitutive variable to account for material degradation, and thus, allowing to compute fatigue life while running the calculations.

The evolution of the accumulated plastic strain $\bar{\varepsilon}^p$ usually plays a key role in incremental formulations. For instance, the evolution of the damage variable in Lemaitre (1985) Continuum Damage Mechanics model is directly linked with $\dot{\bar{\varepsilon}}^p$. The elastoplatic constitutive model that will be used as the base for the incremental methodology affects $\dot{\bar{\varepsilon}}^p$, and consequently the fatigue life estimation. To illustrate this, one simulates 100 cycles with the highest and lowest strain amplitudes in Tables 5.3 and 5.4, and the evolution of $\bar{\varepsilon}^p$ is plotted for each case. Figure 7.6 shows the outcome of these simulations for fully reverse uniaxial load.

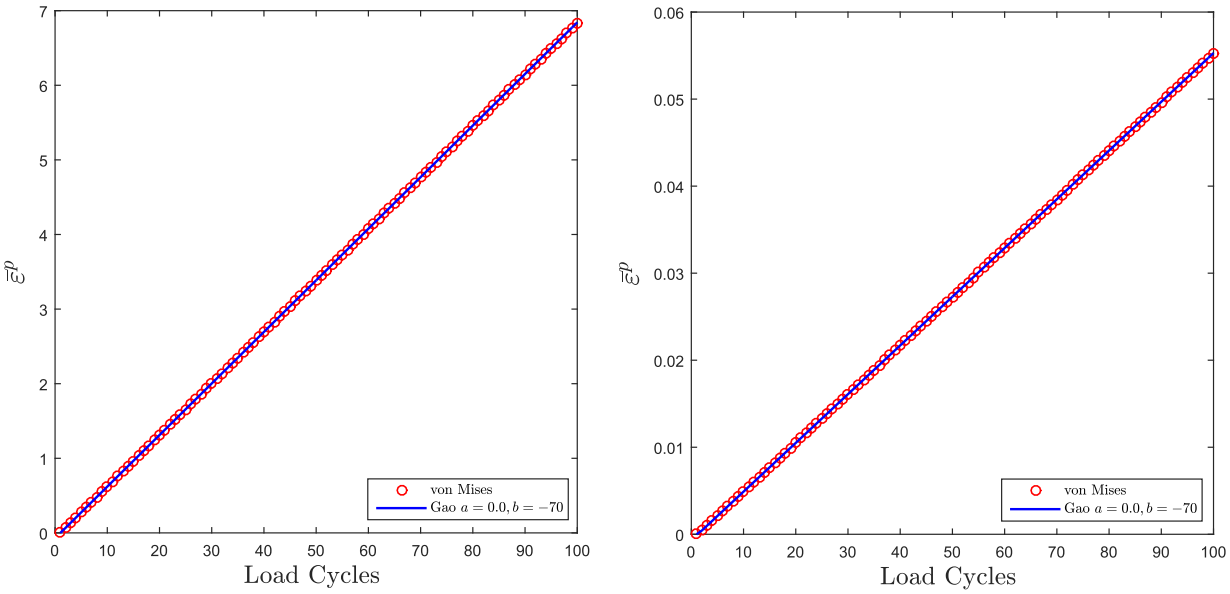

Figure 7.6 – Predicted $\bar{\varepsilon}^p$ evolution by von Mises's and Gao's modeling. The red circles are used to plot Mises's response so one may distinguish it from the blue-solid line. On the left the outcome for ε_a =2.0% and on the right for ε_a =0.15%.

The same behavior in Fig.7.2 is once again observed in Fig.7.6: $\bar{\varepsilon}^p$ evolution from either models are indistinguishable. Thus, as for the critical plane approach, the coupled incremental method will furnish the same fatigue life estimation regardless of the constitutive model choice. Considerable differences rise in the pure torsion case, as depicted in Fig.7.7.

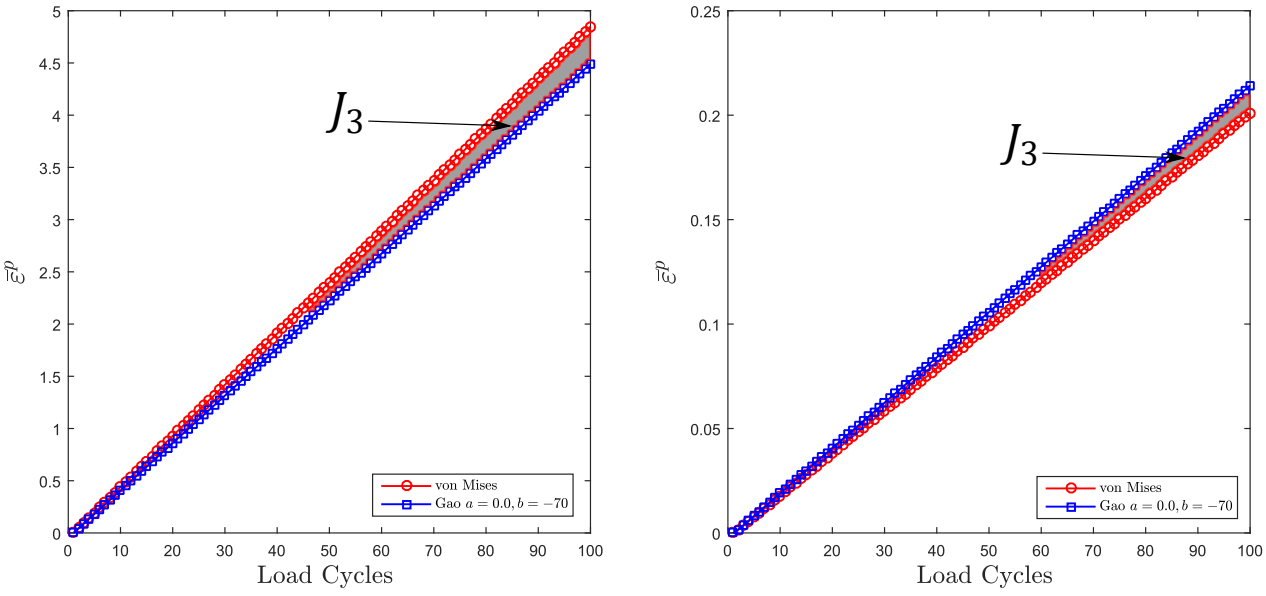

Figure 7.7 – Predicted $\bar{\varepsilon}^p$ evolution by von Mises's and Gao's modeling. On the left the outcome for γ =2.5% and on the right for γ =0.3%.

In pure shear conditions, the shaded regions in Fig.7.7 demonstrate the effect of J_3 on $\bar{\varepsilon}^p$. The red circle curve indicating the accumulated plastic strain evolution according to the Mises-based model has a different growth rate than Gao's blue-squared line. Therefore,

damage mechanics formulations coupled with Mises-yield criterion, for example, expect distinct material degradation, and consequently contrasting crack initiation life. Finally, two features can be observed in Fig7.7: i) elevated shear strain amplitudes display slightly bigger disparities regarding $\bar{\varepsilon}^p$ between the two constitutive approaches than lower γ_a; ii) apparently, overtime the discrepancies on the evolution of $\bar{\varepsilon}^p$ become more substantial. This suggests that for low lives, the constitutive modeling option will have a strong effect on the N_f estimation via incremental approaches. This latter observation is interesting because as γ_a grow, one comes closer to ULCF regime, a condition where J_3 controls the phenomenon behavior.

7.5 Overview

Supported by the results detailed in this Chapter, one points the following remarks:

- In uniaxial conditions, the models behavior coincide as expected. This further cofirms that J_3 becomes less relevant for tensile-compressive predominant situations;
- In pure torsion loads, the shear hysteresis loops predicted by the formulation utilized in this work and J_2 modeling display differences, although not as substantial as notices in monotonic and ULCF conditions;
- Regarding fatigue life assessments, the feasibility of the proposed modeling for practical applications depend on the life estimation methodology chosen. For critical plane methods, it may not justifiable the usage of J_3-sensitive models, while in incremental approaches it can lead to improved results.

8 Conclusion

8.1 Dissertation Conclusions

In this dissertation, the influence of the stress invariants (I_1 and J_3) on the Ductile Fracture, Ultra-Low and Low Cycle fatigue behavior of metallic materials was investigated. The alloy analyzed was the SAE 1045 steel due to the vast experimental data availability on this material, in addition to its industrial relevance. A Gao-based model with mixed hardening was proposed to capture the pressure and third invariant effects, whose parameters were calibrated based on data furnished by Bai (2008) and Leese and Socie (1989). The modeling considered a mixed hardening approach because it recovers isotropic and kinematic hardening as limiting cases. A numerical scheme is elaborated to simulate the SAE 1045 steel response under different loading conditions . Furthermore, an optimization technique is used to identify the isotropic hardening law based on the standard smooth cylindrical tension test.

In Chapter 6, one demonstrates that traditional Mises constitutive modeling fails to describe the monotonic behavior ($\eta \neq 1/3$ and $\xi \neq 1$) other than the calibration point ($\eta = 1/3$ and $\xi = 1$), which indicates that SAE 1045 steel is I_1 and J_3 sensitive. In this regard, one calibrates Gao's a and b constants, and the numerical reaction plots obtained satisfactorily agreed with the experimental F versus d curves, confirming that a proper mechanical description needs account for I_1 and J_3. Moreover, one notices the influence range of I_1 and J_3. For shear-predominant conditions, J_3 affects the SAE 1045 steel monotonic response the most, while I_1 displays the strongest effect on tensile situations.

The Ultra-Low Cycle simulations confirmed once more the SAE 1045 steel I_1 and J_3 dependence. However, monotonically calibrated a and b did not lead to adequate corrections on the numerical F versus d plots, and hence these parameters were recalibrated in ULCF conditions. The recalibration process led to new a and b values and to better numerical predictions. The former suggests that Gao's constants depend on the hardening type considered, since in the monotonic case only isotropic hardening is accounted for while mixed hardening is present in ULCF. The remarks stated on the monotonic simulations regarding I_1 and J_3 influence range are also applicable for ULCF conditions. In either monotonic and Ultra-Low cycle situations, the tested b values were limited by the model convexity.

In Chapter 7, the influence of the third invariant was shown in the Low Cycle Fatigue SAE 1045 steel behavior by Gauss point level simulations. For uniaxial conditions, the numerical responses from Mises and Gao-based models are indistinguishable, which is something expected since several yield surfaces coincide in this stress state. Nevertheless, the hysteresis loops from Mises's and Gao's formulation differed in pure torsion, although less dramatically as observed in Chapter 6 for shear predominant loads. Compared to the mean shear stress amplitudes, Gao's predicted τ_a were always closer than Mises's. One may infer from this observation that better fatigue life estimation can likely be achieved in shear-predominant fatigue loads by utilizing J_3-sensitive formulations for materials whose behavior is affected by this parameter.

The feasibility of the proposed constitutive model for LCF fatigue life assessment purposes depends on the prediction technique chosen. Modelings that account for I_1 and J_3 are an attractive option to be used in incremental approaches because such methods often rely on the evolution $\dot{\bar{\varepsilon}}^p$ of the accumulated plastic strain $\bar{\varepsilon}^p$. One proved that considerable different $\bar{\varepsilon}^p$ growth rates are predicted by Mises and Gao-based formulations, which will lead to distinct fatigue life estimations via incremental techniques.

8.2 Suggestion for Future Works

Some suggestions for future works are:

1. The coupling of the proposed Gao-based constitutive model with Damage Mechanics formulations to predict fracture moment and spot, as well as estimate fatigue life;
2. The utilization of more refined kinematic hardening laws, such as the proposal of Chaboche (1989) and Desmorat (2010);
3. The evaluation of the model performance in LCF conditions under the proportional and nonproportional loading paths in Leese and Socie (1989);
4. The analysis of other stress invariants dependent materials, as for instance the aluminum alloy AA6101-T4 (see Malcher et al. (2020)) ;
5. The proposal of a and b as functions of the hardening types taking place in the particular phenomenon analyzed.

Bibliography

Algarni, M., Y. Choi, and Y. Bai

2017. A unified material model for multiaxial ductile fracture and extremely low cycle fatigue of Inconel 718. *International Journal of fatigue*, 96:162–177. Quoted 3 times on pages 2, 6, and 9.

Araújo, L., G. Ferreira, R. Neves, and L. Malcher

2020. Fatigue analysis for the aluminum alloy 7050-T7451 performed by a two scale continuum damage mechanics model. *Theoretical and Applied Fracture Mechanics*, 105:102439. Quoted on page 9.

Armstrong, P. J. and C. Frederick

1966. *A mathematical representation of the multiaxial Bauschinger effect*, volume 731. Central Electricity Generating Board [and] Berkeley Nuclear Laboratories, Research & Development Department Berkeley. Quoted 2 times on pages 9 and 18.

Bai, Y.

2008. *Effect of Loading History on Necking and Fracture, Massachusetts Institute of Technology*. PhD thesis, PhD thesis. Quoted 26 times on pages vi, viii, x, xiii, 2, 3, 4, 5, 6, 7, 9, 12, 33, 34, 35, 36, 38, 39, 40, 42, 43, 44, 45, 53, 54, and 76.

Bai, Y., X. Teng, and T. Wierzbicki

2006. Study on the effect of the third stress invariant on ductile fracture. Technical report, report 151. Technical report, Impact and Crashworthiness Laboratory .... Quoted on page 7.

Bai, Y. and T. Wierzbicki

2008. A new model of metal plasticity and fracture with pressure and lode dependence. *International journal of plasticity*, 24(6):1071–1096. Quoted 3 times on pages 2, 4, and 7.

Bannantine, J. and D. Socie

1988. Observations of cracking behavior in tension and torsion low cycle fatigue. In *Low Cycle Fatigue*. ASTM International. Quoted 2 times on pages 8 and 9.

Bao, Y. and T. Wierzbicki

2004. On fracture locus in the equivalent strain and stress triaxiality space. *International Journal of Mechanical Sciences*, 46(1):81–98. Quoted 3 times on pages 5, 7, and 53.

Bardet, J.-P.

1990. Lode dependences for isotropic pressure-sensitive elastoplastic materials. Quoted 3 times on pages 5, 6, and 7.

Barsoum, I. and J. Faleskog

2007a. Rupture mechanisms in combined tension and shear—experiments. *International journal of solids and structures*, 44(6):1768–1786. Quoted on page 5.

Barsoum, I. and J. Faleskog

2007b. Rupture mechanisms in combined tension and shear—micromechanics. *International Journal of Solids and Structures*, 44(17):5481–5498. Quoted on page 5.

Basquin, O.

1910. The exponential law of endurance tests. In *Proc Am Soc Test Mater*, volume 10, Pp. 625–630. Quoted on page 8.

BEA

2020. Investigation report. Technical report, Bureau d'Enquêtes et d'Analyses. Quoted on page 1.

Bemfica, C., L. Carneiro, E. Mamiya, and F. Castro

2019. Fatigue and cyclic plasticity of 304L stainless steel under axial-torsional loading at room temperature. *International Journal of Fatigue*, 125:349–361. Quoted 2 times on pages 8 and 9.

Bridgman, P.

1931. The physics of high pressure, london: G. *Bell and Sons, Ltd.* Quoted on page 4.

Bridgman, P.

1953. The effect of pressure on the tensile properties of several metals and other materials. *Journal of Applied Physics*, 24(5):560–570. Quoted on page 5.

Bridgman, P. W.

1923. The compressibility of thirty metals as a function of pressure and temperature. In *Proceedings of the American Academy of Arts and Sciences*, volume 58, Pp. 165–242. JSTOR. Quoted on page 4.

Bridgman, P. W.

1949. Linear compressions to 30,000 kg/cm, including relatively incompressible substances. In *Proceedings of the American Academy of Arts and Sciences*, volume 77, Pp. 189–234. JSTOR. Quoted on page 4.

Brown, L. and J. Embury

1973. Initiation and growth of voids at second-phase particles. In *Proc. Conf. on Microstructure and Design of Alloys, Institute of Metals and Iron and Steel Insitute, London. 1973, 1,(33), 164-169*. Quoted on page 7.

Brown, M. W. and K. Miller

1973. A theory for fatigue failure under multiaxial stress-strain conditions. *Proceedings of the Institution of Mechanical Engineers*, 187(1):745–755. Quoted on page 8.

Brünig, M.

1999. Numerical simulation of the large elastic–plastic deformation behavior of hydrostatic stress-sensitive solids. *International Journal of Plasticity*, 15(11):1237–1264. Quoted 2 times on pages 6 and 7.

Brünig, M., S. Gerke, and V. Hagenbrock

2013. Micro-mechanical studies on the effect of the stress triaxiality and the lode parameter on ductile damage. *International Journal of Plasticity*, 50:49–65. Quoted 4 times on pages 2, 4, 5, and 7.

Brünig, M., S. Gerke, and M. Schmidt

2018. Damage and failure at negative stress triaxialities: Experiments, modeling and numerical simulations. *International Journal of Plasticity*, 102:70–82. Quoted on page 6.

Castro, F. and Y. Jiang

2016. Fatigue life and early cracking predictions of extruded AZ31B magnesium alloy using critical plane approaches. *International Journal of Fatigue*, 88:236–246. Quoted on page 8.

Cavalheiro, J. S. and L. Malcher

2017. Assessment of third invariant elasto-plastic models: Mathematical aspects, numerical strategies and comparative results. *Finite Elements in Analysis and Design*, 123:51–69. Quoted 6 times on pages x, 6, 7, 12, 51, and 54.

Chaboche, J.-L.

1989. Constitutive equations for cyclic plasticity and cyclic viscoplasticity. *International journal of plasticity*, 5(3):247–302. Quoted 4 times on pages 9, 18, 19, and 77.

Coulomb, C. A.

1776. *Essai sur une application des règles de maximis & minimis à quelques problèmes de statique à l'architecture*. De l'Imprimerie Royale. Quoted on page 6.

Courbon, C., T. Mabrouki, J. Rech, D. Mazuyer, F. Perrard, and E. D'Eramo

2013. Towards a physical fe modelling of a dry cutting operation: Influence of dynamic recrystallization when machining aisi 1045. *Procedia CIRP*, 8:516–521. Quoted on page 38.

Crossland, B.

1956. Effect of large hydrostatic pressures on the torsional fatigue strength of an alloy steel. In *Proc. Int. Conf. on Fatigue of Metals*, volume 138, Pp. 12–12. Institution of Mechanical Engineers London. Quoted on page 8.

Dang, V. K.

1971. *Sur la résistance à la fatigue des métaux*. PhD thesis, Université de Paris VI. Quoted on page 8.

de Souza Neto, E. A., D. Peric, and D. R. Owen

2011. *Computational methods for plasticity: theory and applications*. John Wiley & Sons. Quoted 11 times on pages x, 13, 14, 15, 16, 17, 18, 19, 25, 26, and 31.

Desmorat, R.

2010. Non-saturating nonlinear kinematic hardening laws. *Comptes Rendus Mécanique*, 338(3):146–151. Quoted 2 times on pages 9 and 77.

Dowling, N. E. and S. Thangjitham

2000. An overview and discussion of basic methodology for fatigue. *Fatigue and Fracture Mechanics: 31st Volume*. Quoted on page 8.

Driemeier, L., M. Brünig, G. Micheli, and M. Alves

2010. Experiments on stress-triaxiality dependence of material behavior of aluminum alloys. *Mechanics of Materials*, 42(2):207–217. Quoted 5 times on pages 2, 4, 6, 53, and 54.

Driemeier, L., R. T. Moura, I. F. Machado, and M. Alves

2015. A bifailure specimen for accessing failure criteria performance. *International Journal of Plasticity*, 71:62–86. Quoted 2 times on pages 2 and 4.

Drucker, D. C. and W. Prager

1952. Soil mechanics and plastic analysis or limit design. *Quarterly of applied mathematics*, 10(2):157–165. Quoted on page 6.

Ewing, J. A. and W. Rosenhain

1900. Bakerian lecture.—the crystalline structure of metals. *Proceedings of the Royal Society of London*, 65(413-422):172–177. Quoted on page 13.

Fatemi, A. and N. Shamsaei

2011. Multiaxial fatigue: An overview and some approximation models for life estimation. *International Journal of Fatigue*, 33(8):948–958. Quoted on page 8.

Fatemi, A. and D. F. Socie

1988. A critical plane approach to multiaxial fatigue damage including out-of-phase loading. *Fatigue & Fracture of Engineering Materials & Structures*, 11(3):149–165. Quoted on page 8.

Ganjiani, M. and M. Homayounfard

2021. Development of a ductile failure model sensitive to stress triaxiality and lode angle. *International Journal of Solids and Structures*, 225:111066. Quoted on page 6.

Gao, X. and J. Kim

2006. Modeling of ductile fracture: significance of void coalescence. *International Journal of Solids and Structures*, 43(20):6277–6293. Quoted on page 5.

Gao, X., T. Zhang, J. Zhou, S. M. Graham, M. Hayden, and C. Roe

2011. On stress-state dependent plasticity modeling: Significance of the hydrostatic stress, the third invariant of stress deviator and the non-associated flow rule. *International Journal of Plasticity*, 27(2):217–231. Quoted 10 times on pages vi, 2, 3, 4, 6, 7, 9, 19, 51, and 53.

Goodman, J.

1918. *Mechanics applied to engineering*. Longmans, Green. Quoted on page 8.

Gurtin, M. E., E. Fried, and L. Anand

2010. *The mechanics and thermodynamics of continua*. Cambridge University Press. Quoted 3 times on pages 10, 20, and 21.

Hancock, J. and A. Mackenzie

1976. On the mechanisms of ductile failure in high-strength steels subjected to multi-axial stress-states. *Journal of the Mechanics and Physics of Solids*, 24(2-3):147–160. Quoted 2 times on pages 5 and 7.

Hosford, W.

1972. A generalized isotropic yield criterion. Quoted 2 times on pages 6 and 7.

Hosford, W. F.

2013. *Fundamentals of engineering plasticity*. Cambridge University Press. Quoted on page 17.

Jiang, Y., W. Ott, C. Baum, M. Vormwald, and H. Nowack

2009. Fatigue life predictions by integrating evicd fatigue damage model and an advanced cyclic plasticity theory. *International Journal of Plasticity*, 25(5):780–801. Quoted 2 times on pages 9 and 73.

Kalnaus, S.

2009. *Investigation of fatigue behavior of two austenitic stainless steels*. University of Nevada, Reno. Quoted on page 9.

Khan, A. S. and S. Huang

1995. *Continuum theory of plasticity*. John Wiley & Sons. Quoted 2 times on pages 13 and 17.

Khan, A. S. and H. Liu

2012. A new approach for ductile fracture prediction on al 2024-T351 alloy. *International Journal of Plasticity*, 35:1–12. Quoted on page 7.

Kim, J., G. Zhang, and X. Gao

2007. Modeling of ductile fracture: application of the mechanism-based concepts. *International journal of solids and structures*, 44(6):1844–1862. Quoted on page 5.

Kleinermann, J.-P. and J.-P. Ponthot

2003. Parameter identification and shape/process optimization in metal forming simulation. *Journal of Materials Processing Technology*, 139(1-3):521–526. Quoted 4 times on pages 17, 23, 36, and 42.

Koutsolelos, E.

2012. *Numerical analysis of a shear ram and experimental determination of fracture parameters*. PhD thesis, Massachusetts Institute of Technology. Quoted 2 times on pages 2 and 7.

Leese, G. E. and D. Socie

1989. *Multiaxial Fatigue: Analysis and Experiments: AE 14*. Society of Automotive Engineers. Quoted 15 times on pages vi, viii, xiii, 2, 3, 36, 38, 40, 41, 42, 43, 46, 50, 76, and 77.

Lemaitre, J.

1985. A continuous damage mechanics model for ductile fracture. *Journal of engineering materials and technology*, 107(1):83–89. Quoted on page 73.

Lemaitre, J.

2012. *A course on damage mechanics*. Springer Science & Business Media. Quoted 2 times on pages 5 and 7.

Lemaitre, J. and J.-L. Chaboche

1994. *Mechanics of solid materials*. Cambridge university press. Quoted 5 times on pages 13, 14, 17, 20, and 43.

Lemaitre, J., J. Sermage, and R. Desmorat

1999. A two scale damage concept applied to fatigue. *International Journal of fracture*, 97(1-4):67. Quoted on page 9.

Li, S., X. Xie, Q. Tian, C. Cheng, and Z. Zhang

2021a. Improved ultra-low cycle fatigue fracture models for structural steels considering the dependence of cyclic damage degradation parameters on stress triaxiality. *International Journal of Steel Structures*, 21(1):329–348. Quoted 3 times on pages 2, 6, and 9.

Li, X., W. Yang, D. Xu, K. Ju, and J. Chen
2021b. A new ductile fracture criterion considering both shear and tension mechanisms on void coalescence. *International Journal of Damage Mechanics*, 30(3):374–398. Quoted on page 6.

Lopes, J. and L. Malcher
2017. Fatigue life estimates under non-proportional loading through continuum damage evolution law. *Theoretical and Applied Fracture Mechanics*, 88:64–73. Quoted on page 9.

Ludwik, P.
1909. *Elemente der technologischen Mechanik*. Springer. Quoted on page 16.

Machado, L. and L. Malcher
2019. Isotropic hardening curve characterization by the resultant profile of ball indentation tests. *Journal of the Brazilian Society of Mechanical Sciences and Engineering*, 41(11):1–14. Quoted 3 times on pages 17, 36, and 37.

Malcher, L. and E. Mamiya
2014. An improved damage evolution law based on continuum damage mechanics and its dependence on both stress triaxiality and the third invariant. *International Journal of Plasticity*, 56:232–261. Quoted on page 7.

Malcher, L., L. Morales, V. Rodrigues, V. Silva, L. Araújo, G. Ferreira, and R. Neves
2020. Experimental program and numerical assessment for determination of stress triaxiality and j3 effects on aa6101-t4. *Theoretical and Applied Fracture Mechanics*, P. 102476. Quoted 9 times on pages 2, 4, 5, 34, 36, 51, 53, 54, and 77.

Malcher, L., F. A. Pires, and J. C. De Sá
2012. An assessment of isotropic constitutive models for ductile fracture under high and low stress triaxiality. *International Journal of Plasticity*, 30:81–115. Quoted 5 times on pages 2, 4, 6, 7, and 36.

Mamiya, E., J. Araújo, and F. Castro
2009. Prismatic hull: a new measure of shear stress amplitude in multiaxial high cycle fatigue. *International Journal of Fatigue*, 31(7):1144–1153. Quoted 2 times on pages 8 and 70.

Mamiya, E. N. and J. A. Araújo
2002. Fatigue limit under multiaxial loadings: on the definition of the equivalent shear stress. *Mechanics Research Communications*, 29(2-3):141–151. Quoted on page 8.

Matake, T.
1977. An explanation on fatigue limit under combined stress. *Bulletin of JSME*, 20(141):257–263. Quoted on page 8.

McClintock, F. A.
1968. A criterion for ductile fracture by the growth of holes. Quoted on page 7.

Mirone, G. and D. Corallo
2010. A local viewpoint for evaluating the influence of stress triaxiality and lode angle on ductile failure and hardening. *International Journal of Plasticity*, 26(3):348–371. Quoted on page 6.

Mises, R. v.
1913. Mechanik der festen körper im plastisch-deformablen zustand. *Nachrichten von der Gesellschaft der Wissenschaften zu Göttingen, Mathematisch-Physikalische Klasse*, 1913:582–592. Quoted 2 times on pages 1 and 4.

Mohr, O.
1900. Welche umstände bedingen die elastizitätsgrenze und den bruch eines materials? z ver deut ing. Quoted on page 6.

Morales, L.
2020. *Estudo Experimental e Numúerico do Comportamento Mecânico na Fratura da Liga AISI 4340*. PhD thesis, University of Braília. Quoted 3 times on pages 5, 34, and 54.

Nahshon, K. and J. Hutchinson
2008. Modification of the gurson model for shear failure. *European Journal of Mechanics-A/Solids*, 27(1):1–17. Quoted on page 7.

Nayak, G. and O. Zienkiewicz
1972. Elasto-plastic stress analysis. a generalization for various constitutive relations including strain softening. Quoted on page 6.

Neves, R., G. Ferreira, and L. Malcher
2020. Gurson-based incremental damage in fatigue life estimate under proportional and non-proportional loading: Constant amplitude and low cycle regime applications. *Theoretical and Applied Fracture Mechanics*, 108:102678. Quoted on page 9.

Pereira, J., A. De Jesus, and A. Fernandes
2016. A new ultra-low cycle fatigue model applied to the x60 piping steel. *International Journal of Fatigue*, 93:201–213. Quoted 4 times on pages 2, 3, 6, and 9.

Prager, W.
1955. The theory of plasticity: a survey of recent achievements. *Proceedings of the Institution of Mechanical Engineers*, 169(1):41–57. Quoted 2 times on pages 9 and 18.

Rad, S. G. and A. Zajkani
2020. On the stress state-based coupled plasticity–ductile damage model for aluminum

alloys considering the influence of high-rate impulsive preload. *International Journal of Impact Engineering*, 146:103715. Quoted on page 6.

Rice, J. R. and D. M. Tracey
1969. On the ductile enlargement of voids in triaxial stress fields. *Journal of the Mechanics and Physics of Solids*, 17(3):201–217. Quoted 2 times on pages 5 and 7.

Simo, J. and T. Hughes
1998. R. computational inelasticity. Quoted 2 times on pages 25 and 26.

Singh, S., S. Samir, K. Kumar, and S. Thapa
2021. Effect of heat treatment processes on the mechanical properties of aisi 1045 steel. *Materials Today: Proceedings*, 45:5097–5101. Quoted on page 38.

Smith, K., T. Topper, and P. Watson
1970. A stress strain function for the fatigue of metals (stress-strain function for metal fatigue including mean stress effect). *J. Materials*, 5:767–778. Quoted 2 times on pages 8 and 73.

Soderberg, C. R.
1939. Factor of safety and working stress. *Trans Am Soc Mech Eng*, 52:13–28. Quoted on page 8.

Tekin, A., C. Choi, T. Altan, H. Adin, A. Tekin, C. Choi, T. Altan, and H. Adin
2015. Estimation of shear force for blind shear ram blowout preventers. *Res Eng Struct Mater*, 1:39–51. Quoted 2 times on pages 2 and 7.

Thompson, S. W., V. Parthasarathi, and K. O. Findley
2021. A comparison of bending-fatigue properties of surface-induction-hardened sae 1045 bar steels with and without vanadium and the influence of comparable low-temperature induction-tempering and furnace-tempering treatments. *Materials Science and Engineering: A*, 807:140812. Quoted on page 38.

Tresca, H. E.
1869. *Mémoire sur l'écoulement des corps solides*, volume 18. Imprimerie impériale. Quoted on page 6.

Tuo, Z., Z. Yue, X. Zhuang, X. Min, H. Badreddine, L. Qiu, and J. Gao
2021. Comparison of two uncoupled ductile damage initiation models applied to dp900 steel sheet under various loading paths. *International Journal of Damage Mechanics*, P. 1056789520945002. Quoted 2 times on pages 6 and 7.

Veritas, D. N.
2011. Forensic examination of deepwater horizon blowout preventer, vols. i and ii (appendices). *Final Report for US Department of the Interior, Bureau of Ocean Energy*

Management, Regulation, and Enforcement, Washington, DC Report No. EP030842. Quoted on page 1.

Wang, P. and S. Qu

2018. Analysis of ductile fracture by extended unified strength theory. *International Journal of Plasticity*, 104:196–213. Quoted on page 6.

Wilson, C. D.

2002. A critical reexamination of classical metal plasticity. *J. Appl. Mech.*, 69(1):63–68. Quoted on page 6.

Wilson, D., W. Wan, and F. P. Dunne

2019. Microstructurally-sensitive fatigue crack growth in hcp, bcc and fcc polycrystals. *Journal of the Mechanics and Physics of Solids*, 126:204–225. Quoted on page 9.

Wöhler, A.

1860. Versucheüber die festiykeit eisenbahnwagenuchsen. *Z Bauwesen*, 10. Quoted on page 8.

Xu, F., T.-M. Chan, T. Sheehan, and L. Gardner

2020. Prediction of ductile fracture for circular hollow section bracing members under extremely low cycle fatigue. *Engineering Structures*, 214:110579. Quoted 2 times on pages 2 and 9.

Xue, L.

2008. Constitutive modeling of void shearing effect in ductile fracture of porous materials. *Engineering Fracture Mechanics*, 75(11):3343–3366. Quoted on page 7.

Yu, F., P.-Y. B. Jar, and M. T. Hendry

2018. Constitutive analysis of pressure-insensitive metals under axisymmetric tensile loading: A stress triaxiality-dependent plasticity damage model. *International Journal of Mechanical Sciences*, 142:21–32. Quoted on page 6.

Zhang, X.-W., J.-F. Wen, X.-C. Zhang, X.-G. Wang, and S.-T. Tu

2019. Effects of the stress state on plastic deformation and ductile failure: Experiment and numerical simulation using a newly designed tension-shear specimen. *Fatigue & Fracture of Engineering Materials & Structures*, 42(9):2079–2092. Quoted on page 6.

Zhu, L., S. F. Estefen, and M. I. Lourenço

2020. Fracture criteria applied to numerical simulation of blowout preventer ram shearing. *Engineering Failure Analysis*, P. 104596. Quoted 2 times on pages 2 and 7.

Appendixes

A Derivatives Required for Newton-Raphson Method and Consitant Tangent Operator

The following derivatives are present in the coefficient matrices in Eq.(4.24) and (4.33).

A.1 Derivatives Associated with $R_{\mathbf{S}}$

$$\frac{\partial R_{\boldsymbol{S}}}{\partial \boldsymbol{S}} = \mathbb{I} + 2G\Delta\gamma \frac{\partial \boldsymbol{N}^D}{\partial \boldsymbol{S}}, \tag{A.1}$$

$$\frac{\partial R_{\mathbf{S}}}{\partial \bar{\varepsilon}^p} = \mathbf{0}, \tag{A.2}$$

$$\frac{\partial R_{\mathbf{S}}}{\partial \Delta\gamma} = 2G\boldsymbol{N}^D, \tag{A.3}$$

$$\frac{\partial R_{\mathbf{S}}}{\partial p} = 2G\Delta\gamma \frac{\partial \boldsymbol{N}^D}{\partial p}, \tag{A.4}$$

$$\frac{\partial R_{\mathbf{S}}}{\partial \boldsymbol{\beta}^D} = 2G\Delta\gamma \frac{\partial \boldsymbol{N}^D}{\partial \boldsymbol{\beta}^D}, \tag{A.5}$$

$$\frac{\partial R_{\mathbf{S}}}{\partial \beta^V} = 2G\Delta\gamma \frac{\partial \boldsymbol{N}^D}{\partial \beta^V}, \tag{A.6}$$

with:

$$\begin{aligned}\frac{\partial \mathbf{N}^D}{\partial \boldsymbol{S}} = \frac{c}{6}\left[\left(\frac{-5}{6}\Lambda^{\frac{-11}{6}}\right)\frac{\partial \Lambda}{\partial \boldsymbol{S}} \otimes \left(81J_2^2\left(\boldsymbol{\eta}^D\right) + 2bJ_3\left(\boldsymbol{\eta}^D\right)\det\left(\boldsymbol{\eta}^D\right)\left(\boldsymbol{\eta}^D\right)^{-T} : \mathbb{I}^D\right)\right] \\ + \frac{c}{6}\Lambda^{\frac{-5}{6}}\left[\frac{\partial}{\partial \boldsymbol{S}}\left(81J_2^2\left(\boldsymbol{\eta}^D\right)\right) + \frac{\partial}{\partial \boldsymbol{S}}\left(2bJ_3\left(\boldsymbol{\eta}^D\right)\det\left(\boldsymbol{\eta}^D\right)\left(\boldsymbol{\eta}^D\right)^{-T} : \mathbb{I}^D\right)\right].\end{aligned} \tag{A.7}$$

Equations 3.5 and 3.43 imply:

$$\frac{\partial \Lambda}{\partial \boldsymbol{S}} = 81 J_2^2 \left(\boldsymbol{\eta}^D\right) + 2bJ_3 \left(\boldsymbol{\eta}^D\right) \det\left(\boldsymbol{\eta}^D\right) \left(\boldsymbol{\eta}^D\right)^{-T}. \tag{A.8}$$

Define:

$$\begin{cases} \mathbb{L}_1 \coloneqq \dfrac{\partial}{\partial \boldsymbol{S}} \left(81 J_2^2 \left(\boldsymbol{\eta}^D\right)\right), \\ \\ \mathbb{L}_2 \coloneqq \dfrac{\partial}{\partial \boldsymbol{S}} \left(2bJ_3 \left(\boldsymbol{\eta}^D\right) \det\left(\boldsymbol{\eta}^D\right) \left(\boldsymbol{\eta}^D\right)^{-T} : \mathbb{I}^D\right). \end{cases} \tag{A.9}$$

Thus (omitting arguments):

$$\mathbb{L}_1 = 81 \left(2J_2 \boldsymbol{\eta}^D \otimes \boldsymbol{\eta}^D + J_2^2 \mathbb{I}\right). \tag{A.10}$$

If $\boldsymbol{\chi}$ is tensor as:

$$\boldsymbol{\chi} \coloneqq \frac{\partial J_3}{\partial \boldsymbol{\eta}^D} = \det\left(\boldsymbol{\eta}^D\right) \left(\boldsymbol{\eta}^D\right)^{-T}, \tag{A.11}$$

it follows them:

$$\mathbb{L}_2 = 2b \left[\boldsymbol{\chi} \otimes \boldsymbol{\chi} + J_3 \frac{\partial \boldsymbol{\chi}}{\partial \boldsymbol{S}}\right] : \mathbb{I}^D, \tag{A.12}$$

with:

$$\frac{\partial \boldsymbol{\chi}}{\partial \boldsymbol{S}} = \left[\boldsymbol{\chi} \otimes \left(\boldsymbol{\eta}^D\right)^{-T} + \det\left(\boldsymbol{\eta}^D\right) \frac{\partial \left(\boldsymbol{\eta}^D\right)^{-T}}{\partial \boldsymbol{S}}\right]. \tag{A.13}$$

From this point forward, the arguments of J_2 and J_3 will be always omitted as they are always compute with respect to $\boldsymbol{\eta}^D$. Based on Eq.(3.45), one arrives at:

$$\frac{\partial \boldsymbol{N}^D}{\partial p} = \frac{c}{6} \left(\frac{-5}{6} \Lambda^{\frac{-11}{6}}\right) \left[81 J_2^2 \boldsymbol{\eta}^D + 2bJ_3 \boldsymbol{\chi}^D : \mathbb{I}^D\right] \frac{\partial \Lambda}{\partial p}, \tag{A.14}$$

in which:

$$\frac{\partial \Lambda}{\partial p} = 6a I_1^5 \left(\boldsymbol{\eta}\right), \tag{A.15}$$

the argument of I_1 will also be omitted for the same reasons given previously. It can be shown by Eq.(3.38) that:

$$\begin{cases} \dfrac{\partial \boldsymbol{N}^D}{\partial \boldsymbol{\beta}^D} = -\dfrac{\partial \boldsymbol{N}^D}{\partial \boldsymbol{S}}, \\ \dfrac{\partial \boldsymbol{N}^D}{\partial \beta^V} = -\dfrac{\partial \boldsymbol{N}^D}{\partial p} \end{cases} \tag{A.16}$$

A.2 Derivatives Associated with $R_{\bar{\varepsilon}^p}$

$$\frac{\partial R_{\bar{\varepsilon}^p}}{\partial \boldsymbol{S}} = -\frac{\Delta\gamma}{\sigma_y}\left(\boldsymbol{N}^D + \frac{\partial \boldsymbol{N}^D}{\partial \boldsymbol{S}} : \boldsymbol{\eta}^D + 3\eta^V \frac{\partial N^V}{\partial \boldsymbol{S}}\right), \tag{A.17}$$

$$\frac{\partial R_{\bar{\varepsilon}^p}}{\partial \bar{\varepsilon}^p} = 1 + \frac{\Delta\gamma\left(\boldsymbol{\eta}^D : \boldsymbol{N}^D + 3\eta^V N^V\right)}{\sigma^y} H^I, \tag{A.18}$$

$$\frac{\partial R_{\bar{\varepsilon}^p}}{\partial \Delta\gamma} = -\frac{\left(\boldsymbol{\eta}^D : \boldsymbol{N}^D + 3\eta^V N^V\right)}{\sigma_y}, \tag{A.19}$$

$$\frac{\partial R_{\bar{\varepsilon}^p}}{\partial p} = -\frac{\Delta\gamma}{\sigma_y}\left[\frac{\partial \boldsymbol{N}^D}{\partial p} : \boldsymbol{\eta}^D + 3\left(\frac{\partial \eta^V}{\partial p} N^V + \eta^V \frac{\partial N^V}{\partial p}\right)\right], \tag{A.20}$$

$$\frac{\partial R_{\bar{\varepsilon}^p}}{\partial \boldsymbol{\beta}^D} = -\frac{\Delta\gamma}{\sigma_y}\left(-\boldsymbol{N}^D + \frac{\partial \boldsymbol{N}^D}{\partial \boldsymbol{\beta}^D} : \boldsymbol{\eta}^D + 3\eta^V \frac{\partial N^V}{\partial \boldsymbol{\beta}^D}\right), \tag{A.21}$$

$$\frac{\partial R_{\bar{\varepsilon}^p}}{\partial \beta^V} = -\frac{\Delta\gamma}{\sigma_y}\left[\frac{\partial \boldsymbol{N}^D}{\partial \beta^V} : \boldsymbol{\eta}^D + 3\left(\frac{\partial \eta^V}{\partial p} N^V + \eta^V \frac{\partial N^V}{\partial \beta^V}\right)\right], \tag{A.22}$$

where:

$$\frac{\partial N^V}{\partial \boldsymbol{S}} = ac\left(-\frac{5}{6}\Lambda^{\frac{-11}{6}}\right)\frac{\partial \Lambda}{\partial \boldsymbol{S}} I_1^5, \tag{A.23}$$

with $\frac{\partial \Lambda}{\partial \mathbf{S}}$ given in Eq.(A.8). Next,

$$\frac{\partial N^V}{\partial p} = ac\left(\frac{-5}{6}\Lambda^{\frac{-11}{6}} I_1^5 \frac{\partial \Lambda}{\partial p} + \Lambda^{\frac{-5}{6}} 5 I_1^4 \frac{\partial I_1}{\partial p}\right), \tag{A.24}$$

in which:

$$\frac{\partial I_1}{\partial p} = 3, \tag{A.25}$$

and $\frac{\partial \Lambda}{\partial p}$ calculated in Eq.(A.15). It can be shown with Eq.(3.38):

$$\begin{cases} \dfrac{\partial N^V}{\partial \boldsymbol{\beta}^D} = -\dfrac{\partial N^V}{\partial \boldsymbol{S}}, \\ \dfrac{\partial N^V}{\partial \beta^V} = -\dfrac{\partial N^V}{\partial p} \end{cases} \tag{A.26}$$

A.3 Derivatives Associated with $R_{\Delta\gamma}$

$$\frac{\partial R_{\Delta\gamma}}{\partial \boldsymbol{S}} = \frac{\partial \sigma_{eq}}{\partial \boldsymbol{S}}, \tag{A.27}$$

$$\frac{\partial R_{\Delta\gamma}}{\partial \bar{\varepsilon}^p} = -H^I, \tag{A.28}$$

$$\frac{\partial R_{\Delta\gamma}}{\partial \Delta\gamma} = 0, \tag{A.29}$$

$$\frac{\partial R_{\Delta\gamma}}{\partial p} = \frac{\partial \sigma_{eq}}{\partial p}, \tag{A.30}$$

$$\frac{\partial R_{\Delta\gamma}}{\partial \boldsymbol{\beta}^D} = \frac{\partial \sigma_{eq}}{\partial \boldsymbol{\beta}^D}, \tag{A.31}$$

$$\frac{\partial R_{\Delta\gamma}}{\partial \beta^V} = \frac{\partial \sigma_{eq}}{\partial \beta^V}. \tag{A.32}$$

Since σ_{eq} can be written as $\sigma_{eq} = c\Lambda^{1/6}$, it follows:

$$\frac{\partial \sigma_{eq}}{\partial \boldsymbol{S}} = \frac{c}{6}\Lambda^{\frac{-5}{6}}\frac{\partial \Lambda}{\partial \boldsymbol{S}}, \tag{A.33}$$

and

$$\frac{\partial \sigma_{eq}}{\partial p} = \frac{c}{6}\Lambda^{\frac{-5}{6}}\frac{\partial \Lambda}{\partial p} \tag{A.34}$$

Once again, one can prove the relations:

$$\begin{cases} \dfrac{\partial \sigma_{eq}}{\partial \boldsymbol{\beta}^D} = -\dfrac{\partial \sigma_{eq}}{\partial \boldsymbol{S}}, \\ \dfrac{\partial \sigma_{eq}}{\partial \beta^V} = -\dfrac{\partial \sigma_{eq}}{\partial p} \end{cases} \tag{A.35}$$

A.4 Derivatives Associated with R_p

$$\frac{\partial R_p}{\partial \boldsymbol{S}} = 3K\Delta\gamma\frac{\partial \boldsymbol{N}^D}{\partial \boldsymbol{S}}, \tag{A.36}$$

$$\frac{\partial R_p}{\partial \bar{\varepsilon}^p} = 0, \tag{A.37}$$

$$\frac{\partial R_p}{\partial \Delta\gamma} = 3KN^V, \tag{A.38}$$

$$\frac{\partial R_p}{\partial p} = 1 + 3K\Delta\gamma\frac{\partial N^V}{\partial p}, \tag{A.39}$$

$$\frac{\partial R_p}{\partial \boldsymbol{\beta}^D} = 3K\Delta\gamma\frac{\partial N^V}{\partial \boldsymbol{\beta}^D}, \tag{A.40}$$

$$\frac{\partial R_p}{\partial \beta^V} = 3K\Delta\gamma\frac{\partial N^V}{\partial \beta^V}. \tag{A.41}$$

A.5 Derivatives Associated with R_{β^D}

$$\begin{aligned}\frac{\partial R_{\boldsymbol{\beta}^D}}{\partial \boldsymbol{S}} &= -\frac{2}{3}H^K\Delta\gamma\frac{\partial \boldsymbol{N}^D}{\partial \boldsymbol{S}} \\ &\quad + \frac{b^K\Delta\gamma}{\sigma_y}\left(\boldsymbol{N}^D + \frac{\partial \boldsymbol{N}^D}{\partial \boldsymbol{S}} : \boldsymbol{\eta}^D + 3\eta^V\frac{\partial N^V}{\partial \boldsymbol{S}}\right)\otimes\boldsymbol{\beta}^D,\end{aligned} \tag{A.42}$$

$$\frac{\partial R_{\boldsymbol{\beta}^D}}{\partial \bar{\varepsilon}^p} = -\frac{b^K\Delta\gamma}{\sigma_y^2}\left(\boldsymbol{\eta}^D : \boldsymbol{N}^D + 3\eta^V N^V\right)H^I\boldsymbol{\beta}^D, \tag{A.43}$$

$$\frac{\partial R_{\boldsymbol{\beta}^D}}{\partial \Delta\gamma} = -\frac{2}{3}H^K\boldsymbol{N}^D + \frac{b^K}{\sigma_y}\left(\boldsymbol{\eta}^D : \boldsymbol{N}^D + 3\eta^V N^V\right)\boldsymbol{\beta}^D, \tag{A.44}$$

$$\frac{\partial R_{\boldsymbol{\beta}^D}}{\partial p} = -\frac{2}{3}H^K\frac{\partial \boldsymbol{N}^D}{\partial p} + \frac{b^K\Delta\gamma}{\sigma_y}\left[\frac{\partial \boldsymbol{N}^D}{\partial p} : \boldsymbol{\eta}^D + 3\left(\frac{\partial \eta^V}{\partial p}N^V + \eta^V\frac{\partial N^V}{\partial p}\right)\right]\boldsymbol{\beta}^D, \tag{A.45}$$

$$\begin{aligned}\frac{\partial R_{\boldsymbol{\beta}^D}}{\partial \boldsymbol{\beta}^D} &= \mathbb{I} - \frac{2}{3}H^K\Delta\gamma\frac{\partial \mathbf{N}^D}{\partial \boldsymbol{\beta}^D} \\ &\quad + \frac{b^K\Delta\gamma}{\sigma_y}\left(-\boldsymbol{N}^D + \frac{\partial \boldsymbol{N}^D}{\partial \boldsymbol{\beta}^D} : \boldsymbol{\eta}^D + 3\eta^V\frac{\partial N^V}{\partial \boldsymbol{\beta}^D}\right)\otimes\boldsymbol{\beta}^D \\ &\quad + \frac{b^K\Delta\gamma}{\sigma_y}\left(\boldsymbol{\eta}^D : \boldsymbol{N}^D + 3\eta^V N^V\right)\mathbb{I},\end{aligned} \tag{A.46}$$

$$\frac{\partial R_{\boldsymbol{\beta}^D}}{\partial \beta^V} = -\frac{2}{3} H^K \frac{\partial \boldsymbol{N}^D}{\partial \beta^V} + \frac{b^K \Delta\gamma}{\sigma_y} \left[\frac{\partial \boldsymbol{N}^D}{\partial \beta^V} : \boldsymbol{\eta}^D + 3 \left(\frac{\partial \eta^V}{\partial \beta^V} N^V + \eta^V \frac{\partial N^V}{\partial \beta^V} \right) \right] \boldsymbol{\beta}^D. \tag{A.47}$$

A.6 Derivatives Associated with $R_{\beta V}$

$$\begin{aligned} \frac{\partial R_{\beta^V}}{\partial \boldsymbol{S}} &= -\frac{2}{3} H^K \Delta\gamma \frac{\partial N^V}{\partial \boldsymbol{S}} \\ &\quad + \frac{b^K \Delta\gamma}{\sigma_y} \left(\boldsymbol{N}^D + \frac{\partial \boldsymbol{N}^D}{\partial \boldsymbol{S}} : \boldsymbol{\eta}^D + 3\eta^V \frac{\partial N^V}{\partial \boldsymbol{S}} \right) \beta^V, \end{aligned} \tag{A.48}$$

$$\frac{\partial R_{\beta^V}}{\partial \bar{\varepsilon}^p} = -\frac{b^K \Delta\gamma}{\sigma_y^2} \left(\boldsymbol{\eta}^D : \boldsymbol{N}^D + 3\eta^V N^V \right) H^I \beta^V, \tag{A.49}$$

$$\frac{\partial R_{\beta^V}}{\partial \Delta\gamma} = -\frac{2}{3} H^K N^V + \frac{b^K}{\sigma_y} \left(\boldsymbol{\eta}^D : \boldsymbol{N}^D + 3\eta^V N^V \right) \beta^V, \tag{A.50}$$

$$\frac{\partial R_{\beta^V}}{\partial p} = -\frac{2}{3} H^K \frac{\partial N^V}{\partial p} + \frac{b^K \Delta\gamma}{\sigma_y} \left[\frac{\partial \boldsymbol{N}^D}{\partial p} : \boldsymbol{\eta}^D + 3 \left(\frac{\partial \eta^V}{\partial p} N^V + \eta^V \frac{\partial N^V}{\partial p} \right) \right] \beta^V, \tag{A.51}$$

$$\frac{\partial R_{\beta^V}}{\partial \boldsymbol{\beta}^D} = -\frac{2}{3} H^K \Delta\gamma \frac{\partial N^V}{\partial \boldsymbol{\beta}^D} + \frac{b^K \Delta\gamma}{\sigma_y} \left(-\boldsymbol{N}^D + \frac{\partial \boldsymbol{N}^D}{\partial \boldsymbol{\beta}^D} : \boldsymbol{\eta}^D + 3\eta^V \frac{\partial N^V}{\partial \boldsymbol{\beta}^D} \right) \beta^V, \tag{A.52}$$

$$\begin{aligned} \frac{\partial R_{\beta^V}}{\partial \beta^V} &= 1 - \frac{2}{3} H^K \frac{\partial N^V}{\partial \beta^V} + \frac{b^K \Delta\gamma}{\sigma_y} \left[\frac{\partial \boldsymbol{N}^D}{\partial \beta^V} : \boldsymbol{\eta}^D + 3 \left(\frac{\partial \eta^V}{\partial \beta^V} N^V + \eta^V \frac{\partial N^V}{\partial \beta^V} \right) \right] \beta^V \\ &\quad + \frac{b^K \Delta\gamma}{\sigma_y} \left(\boldsymbol{\eta}^D : \boldsymbol{N}^D + 3\eta^V N^V \right) \end{aligned} \tag{A.53}$$